November 2016

C-Ku-Band Dual-Polarized Array Element for Shared-Aperture Frequency-Scanning Array

Amin Nikravan
University of Massachusetts Amherst

C-KU-BAND DUAL-POLARIZED ARRAY ELEMENT FOR SHARED-APERTURE FREQUENCY-SCANNING ARRAY

A Dissertation Presented

by

AMIN NIKRAVAN

Submitted to the Graduate School of the
University of Massachusetts Amherst in partial fulfillment
of the requirements for the degree of

DOCTOR OF PHILOSOPHY

September 2016

Electrical and Computer Engineering

C-KU-BAND DUAL-POLARIZED ARRAY ELEMENT FOR SHARED-APERTURE FREQUENCY-SCANNING ARRAY

A Dissertation Presented

by

AMIN NIKRAVAN

Approved as to style and content by:

Do-Hoon Kwon, Chair

Paul Siqueira, Member

Stephen Frasier, Member

James Manwell, Member

Christopher V. Hollot, Department Head
Electrical and Computer Engineering

To my father, my mother and my brothers.

ACKNOWLEDGMENTS

I would like to express deepest gratitude to my advisor Professor Do-Hoon Kwon for his full support, guidance and encouragement throughout this research. This work would not have been possible without his passion and wisdom.

I would also like to thank Professors Paul Siqueira, Stephen Frasier and James Manwell for having served on my committee. Their thoughtful feedback and counsel were valued greatly. I am very grateful to James Carswell and James Canniff from Remote Sensing Solutions, Inc. who had significant technical and administrative contribution to this research.

Thanks also go to my fellow graduate students at the Antennas and Propagation Laboratory of UMass Amherst, particularly Hsieh-Chi Chang, Caglar Emiroglu, Yutong Yang, Adebayo Adeyemi and John Logan.

This work was supported by the National Oceanic and Atmospheric Administration under Contract No. NRMC0009-12-02700.

Amin Nikravan

Amherst, MA

ABSTRACT

C-KU-BAND DUAL-POLARIZED ARRAY ELEMENT FOR SHARED-APERTURE FREQUENCY-SCANNING ARRAY

SEPTEMBER 2016

AMIN NIKRAVAN

B.S., SHIRAZ UNIVERSITY

M.S., TARBIAT MODARES UNIVERSITY

Ph.D., UNIVERSITY OF MASSACHUSETTS AMHERST

Directed by: Professor Do-Hoon Kwon

Accurate now-casting and forecasting could prevent losses and reduce risks caused by severe weather. Key observation to improve our knowledge of the weather is the ocean vector wind. National Oceanic and Atmospheric Administration (NOAA) is embarking on an ambiguous but needed effort to launch a new satellite-based instrument called the Dual Frequency Scatterometer (DFS) that will provide accurate global mapping of the ocean vector wind in a timely manner. The Advanced Wind and Rain Airborne Profiler (AWRAP) can play a pivotal role for this mission by providing critical measurements to improve the geophysical model function that DFS will relay on to estimate the winds.

AWRAP requires a novel antenna to collect dual-polarized, dual-wavelength measurements. This work develops a subarray for the AWRAP antenna that will enable

it acquire the necessary measurements from the NOAA WP-3D aircraft. By sharing the aperture for both C (5.3 GHz) and Ku (13.8 GHz) bands, this antenna array utilizes the given circular area as efficiently as possible. In both bands, the array is capable of forming and scanning a narrow beam in the $x-z$ plane in the range 40°—60° off normal within 10% of frequency bandwidth, for both vertical and horizontal polarizations.

Each subarray consists of nine dual-polarized Ku-band microstrip patch antennas and two perpendicular C-band slot antennas, sharing the aperture. Microstrip patches and their stripline feed networks are integrated into an 8-layer printed circuit board (PCB) and the slots are formed on an aluminum plate under the PCB. The PCB covers the slots, but they can radiate through the openings in the ground planes of the PCB. The C-band slots are positioned between Ku-band patches every third patch spacing.

In total, four separate feed networks are required to drive the antenna elements in two bands for two polarizations. In order to achieve lower loss and higher antenna efficiencies in a small space, several transmission line technologies (namely, rectangular waveguides, suspended striplines and striplines) are used to deliver the power to the antenna elements. In order to pass the signal between different media, a broadband perpendicular E-plane waveguide-to-suspended stripline transition is designed and fabricated in Ku band. A frequency bandwidth of 12% and an insertion loss as low as 0.09 dB are achieved in measurement.

Measured input return loss of the Ku-subarray is more than 9 dB in the entire frequency bandwidth and realized gains are better than 10 dBi. Cross-polarization levels are less than -20 dB in the lower frequencies. However, in the higher frequencies, cross-polarization levels increase to -15 dB. It is proposed to use mirrored feed technique to improve cross-polarization levels of the array.

For the C-subarray, measured input return loss is better than 12 dB in the entire frequency bandwidth. Measured realized gain at the center frequency is -12 dBi, and cross-polarization level is better than -20 dB.

TABLE OF CONTENTS

LIST OF TABLES

Table **Page**

LIST OF FIGURES

Figure **Page**

CHAPTER 1

INTRODUCTION

1.1 Motivation

Hurricanes can place significant burden on the economy and society. Today, more than half of the United States population resides in coastal areas, and the population and wealth in these areas are steadily increasing. Representing only 17 percent of nation's contiguous land area, the coastal population density is very high. Also, the world's oceans provide the main route for international trade. Further, the United States has significant investment and responsibility in offshore oil operations. This presents significant challenges for hurricane preparation. Without improvements in hurricane and severe ocean storm track and intensity forecasting that can outpace the population and wealth growth along the coast, losses due to hurricanes are expected to increase.

Severe weather impacts our daily lives, society and nation's economy: from an average of $10B (normalized to 2005 dollars) annual loss due to tropical cyclones between 1900—2005, to $200B commercial shipping industry that is threatened by severe ocean storms, to the hundreds of lives and assets being lost in the $20B recreational boating industry [1]. For all of these events and many others, a recurring theme is the need for accurate and timely knowledge of the weather (now-casting and forecasting).

The coastal regions are also great locations for offshore wind farms. Wind turbines in these areas must be built to withstand the harsh wind, waves, and rain from hurricanes and tropical storms. A study in 2012 quantified the likelihood that a

hurricane could topple towers in American waters where projects were under consideration or development [2]. It showed that in the most vulnerable areas then being actively considered by developers, nearly half the turbines in a farm were likely to be destroyed in a 20-year period. The Energy Department is working with NOAA's hurricane research missions to collect data that could lead to improved offshore wind turbine designs. The data shared by NOAA will provide critical insights that could lead to stronger offshore wind turbines and components, such as blades, foundations, and gearboxes capable of withstanding hurricane conditions. Additionally, by being able to better gauge the momentum of winds throughout a storm, turbine operators will be able to more effectively rotate and position the turbine's blades to prevent component and structural damage [3].

The application of phased array technology in weather radars has been growing recently. The pulse to pulse electronic beam steering capability of a phased array radar allows accurate meteorological measurements with a shorter data update time [4, 5]. To explore and develop weather-related applications of the phased array antenna, a National Weather Radar Testbed (NWRT) has been established recently [5].

However, phased array antennas use relatively expensive phase shifters and/or TR modules which makes them less attractive for weather radar applications where a huge number of antenna elements are needed to form a narrow beam for high angular resolution measurements [6]. A more cost-effective alternative is the frequency-scanning array antenna. In this antenna, there is no need for phase shifters and the radiated beam direction is controlled by changing the operating frequency.

1.2 Literature Review

1.2.1 Scatterometers

The sea clutter was observed by early radar operators on their radar displays when looking for sea vessels or airplanes over the ocean. This phenomenon is caused by

backscatter of microwave radar pulses from short capillary waves on the ocean surface. The sea clutter enables microwave scatterometers to measure the ocean surface wind vector [7].

The ocean wind vectors are a key parameter in determining the interaction between the atmosphere and ocean by affecting the heat, moisture, gas and momentum fluxes at this boundary. To this end, the National Centers for Environment Prediction has identified the need for more accurate, higher resolution measurements of the ocean wind vectors as a key priority. Over the last two decades, advances have been made in measuring the ocean wind vectors on a global scale. The United States deployed the SeaWinds instrument on the Japan Aerospace Exploration Agency (JAXA) ADEOS II satellite and the United States QuikSCAT satellite [8, 9]. SeaWinds was a Ku-band, dual beam conically scanning scatterometer that measured normalized radar cross section (NRCS) of the ocean surface over a large swath of approximately 1800 km. The measurement geometry of the SeaWinds is shown in Figure 1.1. The ocean wind vectors can be derived from ocean NRCS measurements using ocean wind vector scatterometry techniques even at hurricane force winds [10].

The SeaWinds (QuikSCAT) data has had a significant positive impact on detecting hurricane force winds for extratropical cyclones, early detection of surface circulations in developing tropical cyclones, defining the gale- and storm-force wind radii and much more [12]. However, SeaWinds also had limitations: operating solely at Ku-band, it could not penetrate intense precipitation; its ocean NRCS measurements were adversely affected by attenuation and volume backscatter from moderate precipitation; its resolution was too coarse to resolve the high wind regions within the inner core of tropical cyclones; and its application to coastal regions was limited by its spatial resolution [12]. On November 23, 2009, its mission ended after a decade of operation.

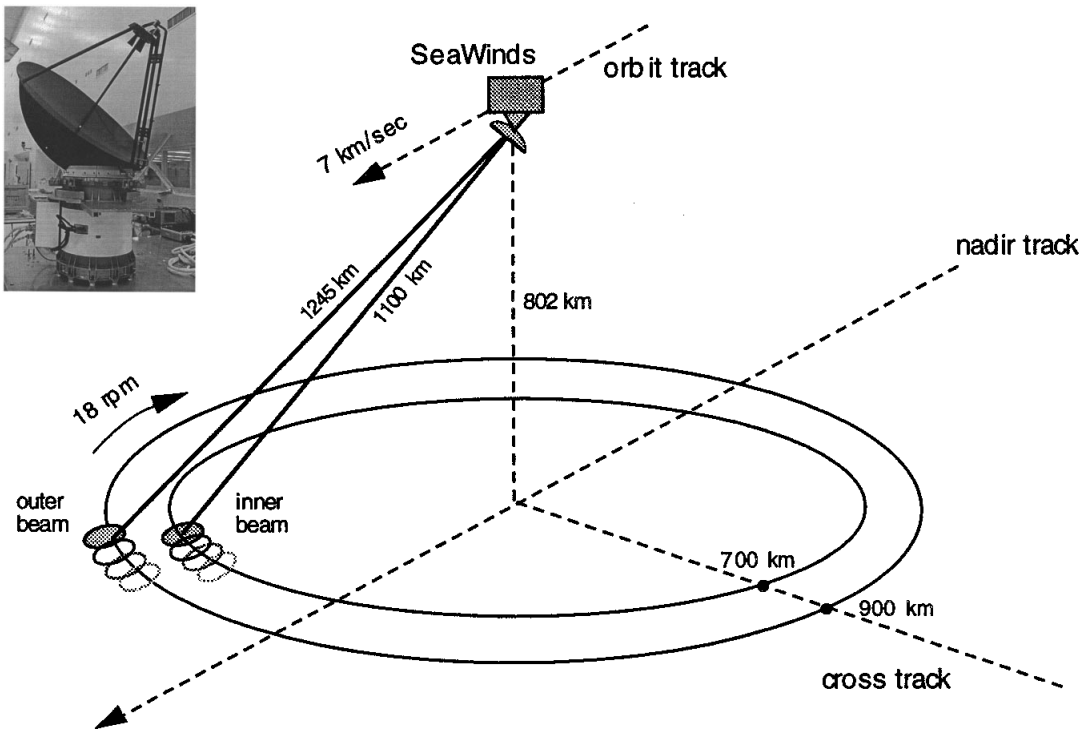

Figure 1.1: Schematic representation of the SeaWinds measurement geometry. Inset photo shows the antenna and rotary mechanism. Reproduced from [11].

Based on the successes of QuikSCAT, NOAA, working with other U.S. agencies and JAXA, has launched an effort to develop a follow-on mission that will address the limitations of QuikSCAT and provide the much-needed global observations of the ocean wind vectors. This new system concept is called the Dual Frequency Scatterometer (DFS) and will operate at C- and Ku-bands collecting measurements at two incidence angles (approximately 49° and 58°) while conically scanning [12]. The addition of C-band will provide the capability to retrieve the ocean wind vectors in the presence of precipitation [13].

Although much work has been done, further ocean NRCS measurements are needed at these frequencies, incidence angles and vertical and horizontal polarization to validate the geophysical model function (GMF) under high wind conditions and precipitation, especially at C band and horizontal polarization. This has been identified as a key risk issue for DFS.

Figure 1.2: Department of Commerce WP-3D "Hurricane Hunter" [16].

To realize these improvements and address key risk areas for the DFS mission, airborne ocean vector scatterometers have been used to collect targeted measurements in high wind conditions and in the presence of precipitation. Such systems can also provide high resolution targeted ocean wind vector observations for now-casting and forecasting applications.

Over the last decade, University of Massachusetts Amherst's Microwave Remote Sensing Laboratory (MIRSL) designed, built and deployed the Imaging Wind and Rain Airborne Profiler (IWRAP) [7, 14]. IWRAP was designed to collect targeted observations and also provide real-time surface and atmospheric observations. Deployed on the NOAA WP-3D aircraft (Figure 1.2), MIRSL have collected high resolution ocean NRCS measurements at C- and Ku-band in winds up to 70 m/s. With its two conically scanning antennas, one Ku-band and the other C-band, IWRAP scans the surface below the aircraft. Both antennas are microstrip patch arrays that transmit a pencil-beam that can be frequency-steered between 25° and 50° incidence [15]. From these measurements, they have derived improved GMFs [10].

1.2.2 Frequency-Scanning Arrays

The design and analysis of frequency-scanning arrays have been studied extensively in the literature [17–26]. The principles of using microstrip resonators as radiating elements in a frequency-scanning antenna array are described in [17].

In the X-band frequency-scanning array in [22], a low-loss rectangular waveguide is used as the slow-wave structure. Figure 1.3 shows the geometry and radiation patterns of the array. The microstrip patch array is coupled to the waveguide via slots on the narrow wall of the waveguide. The simulated range of the scanning angles is $-48°$—$+45°$ for 10% frequency variation.

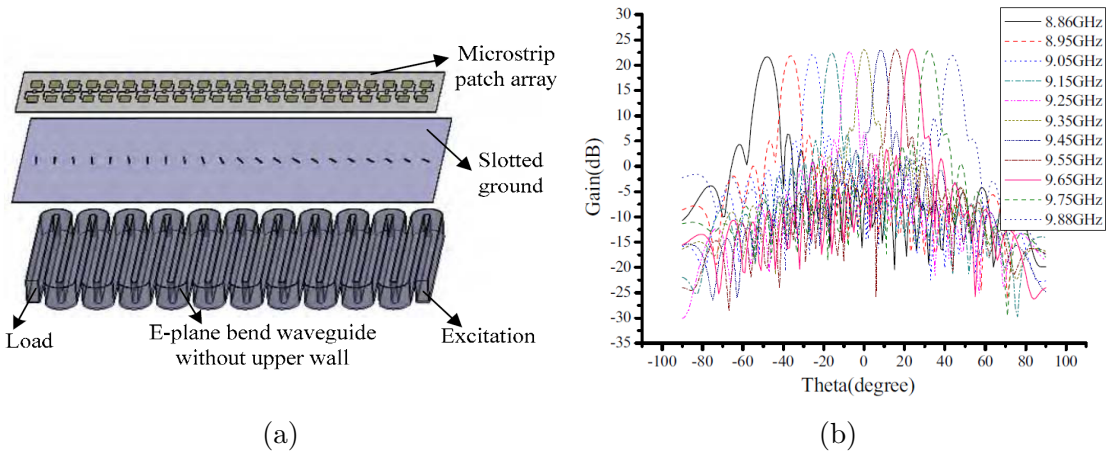

(a) (b)

Figure 1.3: An X-band frequency-scanning microstrip array [22]. (a) The geometry. (b) The simulated radiation patterns.

To increase the frequency sensitivity of the scan angle, the X-band resonators are cascade-coupled in [17], as shown in Figure 1.4. This results in a phase-shift in the resonator in addition to that created by the transmission line. Consequently, the array was able to scan the main lobe between $-30°$ and $+30°$ with less than 6.5% frequency variation. However, a low radiation efficiency of -6.6 dB was observed in measurement.

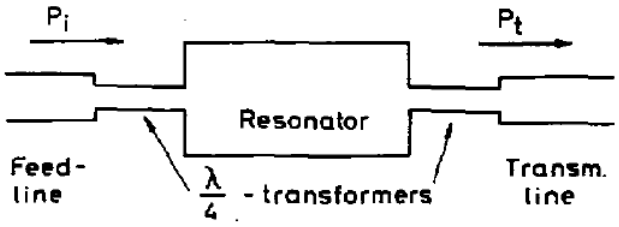

Figure 1.4: Cascade-coupled microstrip resonators [17].

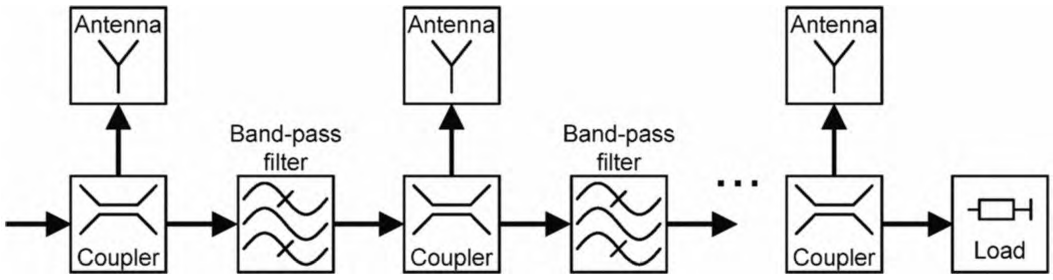

Figure 1.5: A narrowband frequency-scanning array with bandpass feed structure for extra phase shift [19].

Another approach is taken in [19], by using band-pass filters between the array elements, as shown in Figure 1.5. Adding a bandpass filter—with an almost linear phase response around its center frequency—between the individual antenna elements causes an additional phase shift. An angular range of -50° to $+50^\circ$ is obtained in a frequency bandwidth of 2.5%.

A circularly-polarized frequency-scanning array is introduced in [24]. It uses dual-feed square microstrip patch element with a chamfered corner to achieve circular polarization. The scan angle squints between -6° to $+5^\circ$ with a frequency variation of 3.5%.

The application of metamaterials in the design of frequency-scanning arrays have also been of great interest recently. Phased-array feed network based on composite right/left handed (CRLH) dispersive transmission lines are discussed in [25, 26]. A CRLH transmission line enables systematic engineering of the phase response pro-

viding both phase advance and phase delay. This allows the design of an all-passive frequency-scanning array with a large scanning angle range toward both positive and negative angles. The proposed method completely decouples the radiating antenna element from the array factor, providing extra design freedom and enhanced radiation performance.

1.2.3 Dual-Polarized Arrays

Weather radars have been updated to a dual polarization capability to obtain more meteorological information [27–31]. For this reason, the dual-polarized frequency-scanning arrays have also attracted increasing attention recently.

The antenna arrays presented in [32, 33] are mid-size cylindrical polarimetric phased array radars for weather sensing applications. The beam scans the elevation by changing the frequency, and the azimuth by commutation. The maximum elevation scan angle is about 20° for a frequency change from 2.7 GHz to 3.0 GHz. The cylindrical array consists of 96 frequency-scanning vertical columns mounted on the surface of a cylinder (Figure 1.6(a)). Each antenna column consists of 19 stacked microstrip patch elements. As shown in Figure 1.6(b), each patch element is excited through two perpendicular slots on the ground plane and two series feed striplines underneath, one for each polarization. They are all realized in a 5-layer printed circuit board. The maximum cross-polarization levels reported for the broadside radiation are -20 dB in [32] and -25 dB in [33].

The cross-polarization level is substantially suppressed to -50 dB in [6, 34] using two feeding methods: the differential [35–38] and the mirrored-feed configurations [38–40]. In the first method, for the vertical polarization purity, each patch element is excited with two inset feeds of equal input powers and 180° phase difference in the vertical direction. The higher order modes contributing to the cross polarization radiation pattern are suppressed with this configuration. In the second

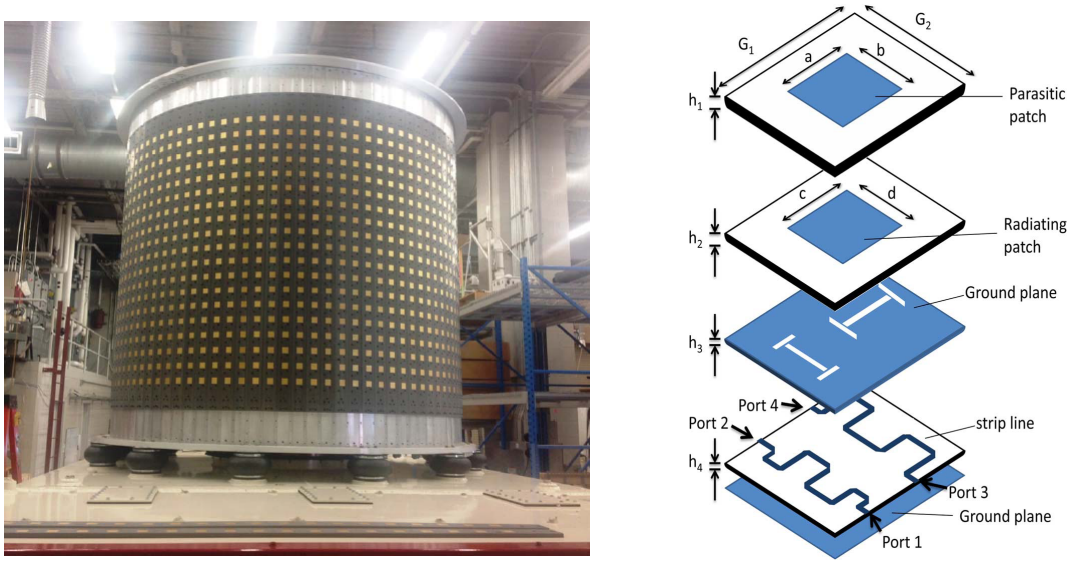

(a) (b)

Figure 1.6: The University of Oklahoma's dual-polarized series-fed microstrip antenna array. (a) Photograph of the cylendrical array [32]. (b) Configuration of the single element antenna [33].

arrangement, for the horizontal polarization purity, each column is a mirrored version of its neighboring columns. The co-polar components of two columns add up in phase and the cross-polar components cancel each other out.

Diffusion bonding of laminated metal plates [41–44] has been used by a group or researchers for the fabrication of slot array antennas. This new fabrication technique is very promising in millimeter-wave to THz bands because of low cost and high precision. It is realized by stacking a number of laminated metal layers as thin as 0.2 mm. Each layer could have its individual etching pattern. Perfect electric connection can be realized between the metal layers by diffusion bonding at high temperature of about 1000°C. The design and fabrication of a dual-polarization waveguide slot array for 60 GHz band is presented in [45,46]. To realize the dual-polarization, cross-shaped radiating slots and a multilayer feeding structure are employed (See Figure 1.7). The

measured gain of the 16×16-element array is higher than 32 dBi with an antenna efficiency of 80%.

Another dual-polarized slot antenna array using only one layer of substrate board is presented in [47]. Two identical coplanar waveguide (CPW) series-fed slot arrays are positioned orthogonally and provide dual polarization. Each polarization is placed on one side of a single substrate. The antenna radiates in both sides of the substrate which is acceptable for the 2.4 GHz wireless local area network (WLAN) application. Due to high mismatch at the input, the antenna efficiency is only 30%. The cross-polarization level is −16 dB.

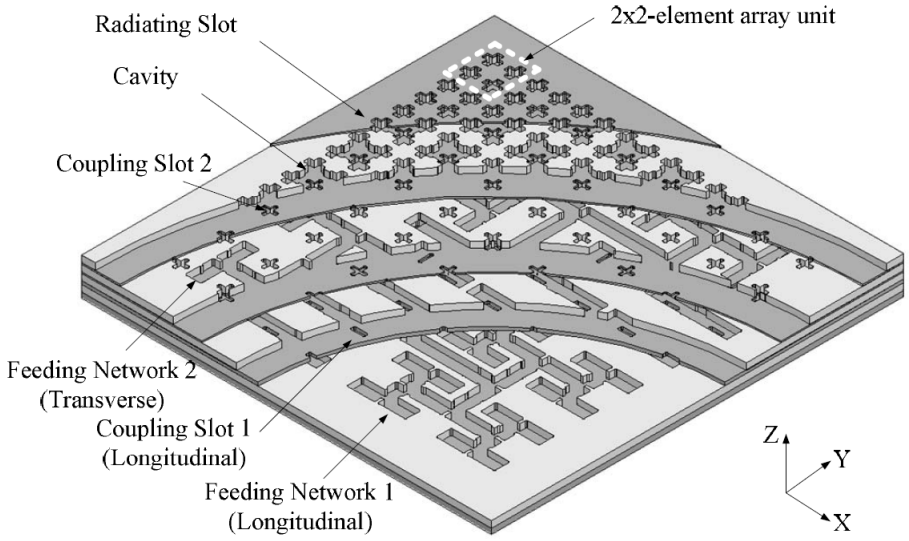

Figure 1.7: A dual-polarization waveguide slot array using diffusion bonding of laminated thin plates [45].

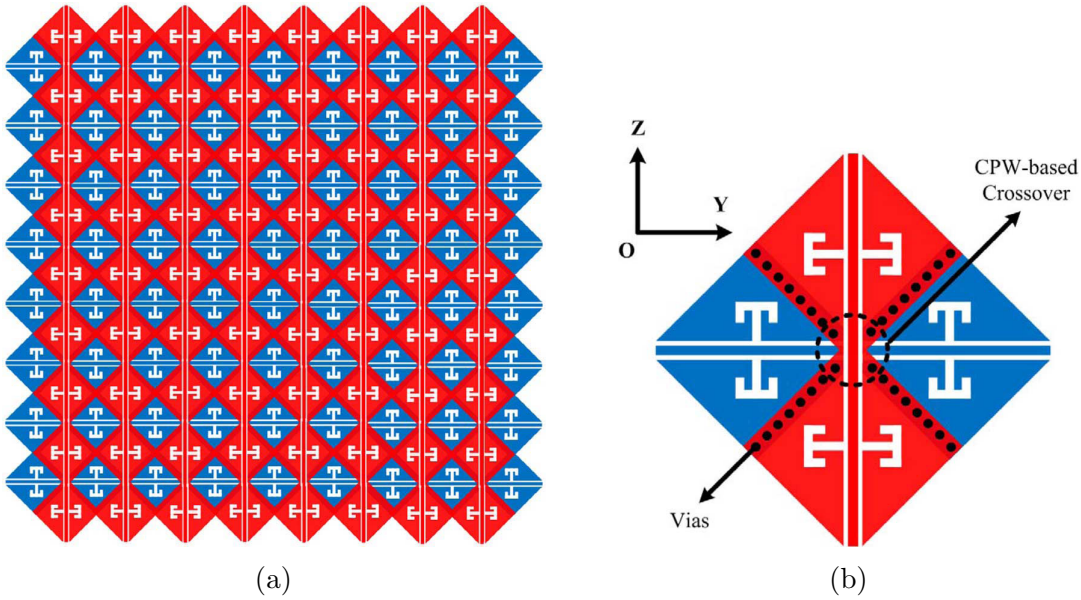

Figure 1.8: A dual-polarized series-fed slot antenna array [47]. (a) Geometry of the array. (b) Detailed view of element connection and CPW-based crossover.

1.2.4 Dual-Band Arrays

Another trend in microwave remote sensing radars is to perform simultaneous measurements at different frequency bands [12]. A dual-band array can be designed in one of two fundamental ways: using dual-band elements or using interleaved single-band elements [48, 49].

In the first method, each element is capable of covering both bands simultaneously but usually needs the frequency bands to be near-harmonic. In addition, large frequency ratios result in unnecessary increase in the number of elements in the lower band, and a large and complicated associated feed network. Moreover, dual-band antenna elements usually suffer from poor polarization purity and low isolation between bands.

In the second method, two independent arrays of single-band radiating elements are interleaved. Each set must have a uniform periodic lattice such that each element has the optimum spacing between them for grating-lobe-free operation. Thus, the

difficulty in interleaving lies in the physical arrangement of the element footprints so that they do not overlap. As the elements of each set are in close proximity, the electromagnetic coupling between them will have a large affect on the array performance in each band [49].

For the first example of using dual band elements, consider the loop loaded dipoles in [50]. A pair of loops is placed on or underneath the dipole aperture, providing dual-band operation at 3 GHz and 5.5 GHz. It is numerically demonstrated that the 3×3 array offers 15% impedance bandwidths at designated frequencies. The broadside simulated gains are 13 dBi and 17 dBi at 3 GHz and 5.5 GHz, respectively.

The method presented in Figure 1.9 offers phase advance in addition to phase delay in a single feed network, which allows dual-band operation capable of directing the radiated beam to arbitrary directions [26]. It uses dual-band CRLH dispersive lines which are capable of controlling the relative phase differences at two operating frequency bands simultaneously. A four-element linear phased array using Quasi-Yagi inspired dual-band antennas is demonstrated in Figure 1.9(b). Antenna efficiencies of 62% and 49% are achieved at 1.8 GHz and 2.5 GHz, respectively. The main lobes are towards $\theta = 10^\circ$ and $\theta = -10^\circ$ at those frequencies, respectively.

A dual-band array with two different antenna elements, one for each band, is presented in Figure 1.10 [51]. It comprises interleaved folded dipoles designed to be resonant at octave-separated frequency bands (1 GHz and 2 GHz). Smaller dipoles are nested inside the larger folded dipoles. Each dipole is gap-fed by a microstrip line on the other side of the substrate. A large array containing 39 printed dipoles (nine 1-GHz elements and thirty nested 2-GHz elements) has been fabricated, with each dipole individually fed to facilitate independent beam control. A frequency bandwidth of 5% and a cross-polarization level of −22 dB are measured.

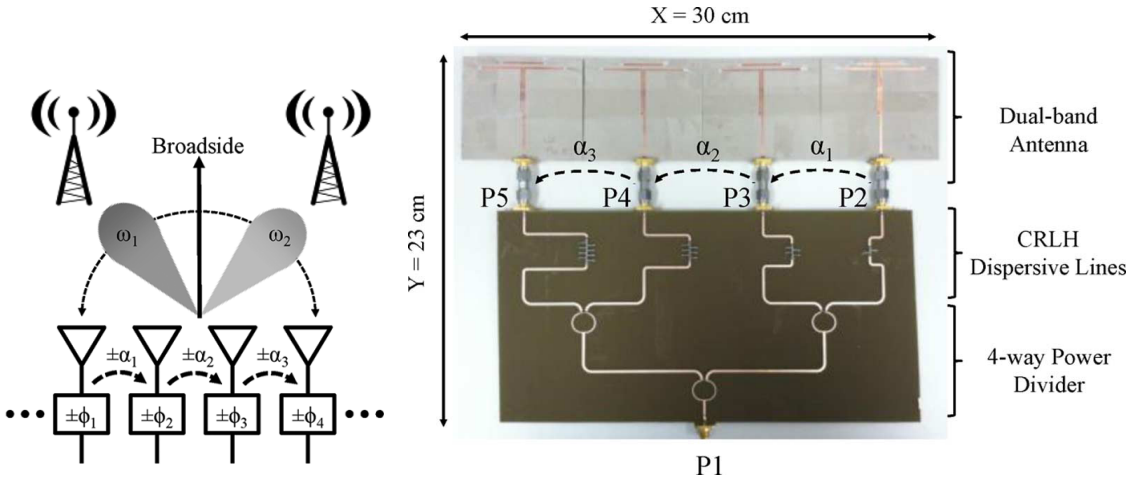

(a) (b)

Figure 1.9: A dual-band CRLH based phased-array antenna [26]. (a) Principle of operation. (b) Photograph of the fabricated antenna.

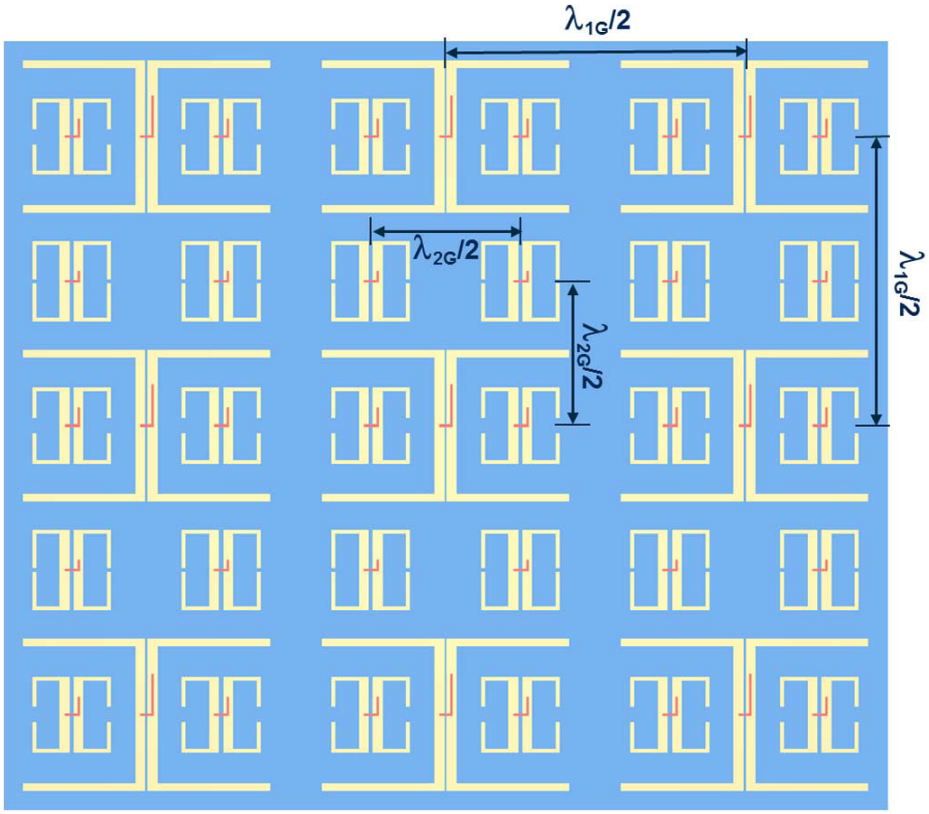

Figure 1.10: A nested-element dipole array for dual-band operation. The wavelengths at 1 GHz and 2 GHz are denoted as λ_{1G} and λ_{2G}, respectively [51].

1.2.5 Shared-Aperture Dual-Band Dual-Polarized Arrays

The Spaceborne Imaging Radar (SIR-C) operated at L- and C-bands with dual linear polarization at each frequency, but these two antennas did not share a common aperture [52]. Consequently, the large mass of the SIR-C antenna would not be compatible with currently operated space platforms. In practice, only a shared-aperture antenna with minimum size and weight has the capability of integration with an aircraft. For this reason, various approaches have been taken in [48, 53–57], to design dual-polarized and dual-band array antennas sharing the same physical aperture, for synthetic aperture radar (SAR) applications.

A shared-aperture dual-band dual-polarized (SADBDP) antenna array with interlaced C-band patches and X-band slots is shown in Figure 1.11 [48]. Narrow frequency bandwidths of 5% and 4% and cross-polarization levels of -21 dB and -18 dB are measured in C and X bands, respectively.

Another SADBDP antenna array is presented in [53] (Figure 1.12). It consists of 2×2 L-band proximity-fed perforated patches interleaved with an array of 12×16 X-band aperture coupled patches. They are realized in a 4-layer printed circuit board

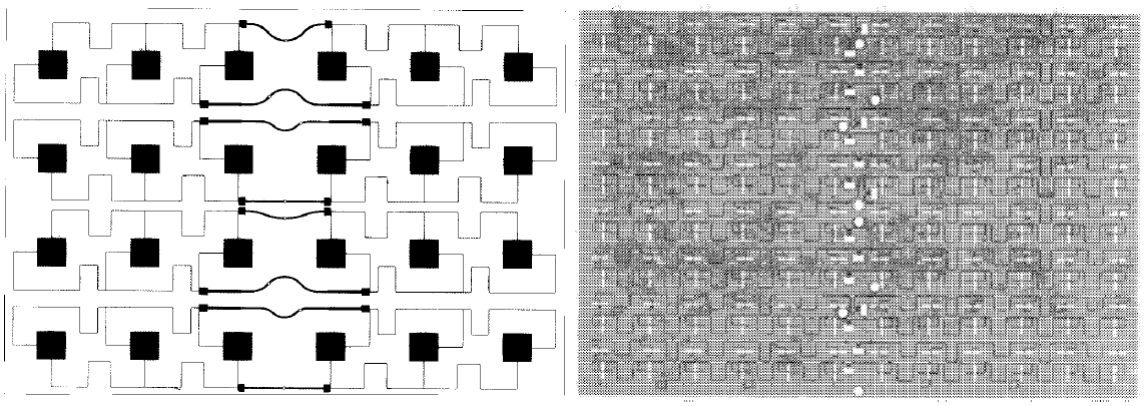

(a) (b)

Figure 1.11: A dual-frequency dual-polarized antenna using C-band patches (a) and X-band slots (b). The C-band patch array layer overlays the X-band slot layer [48].

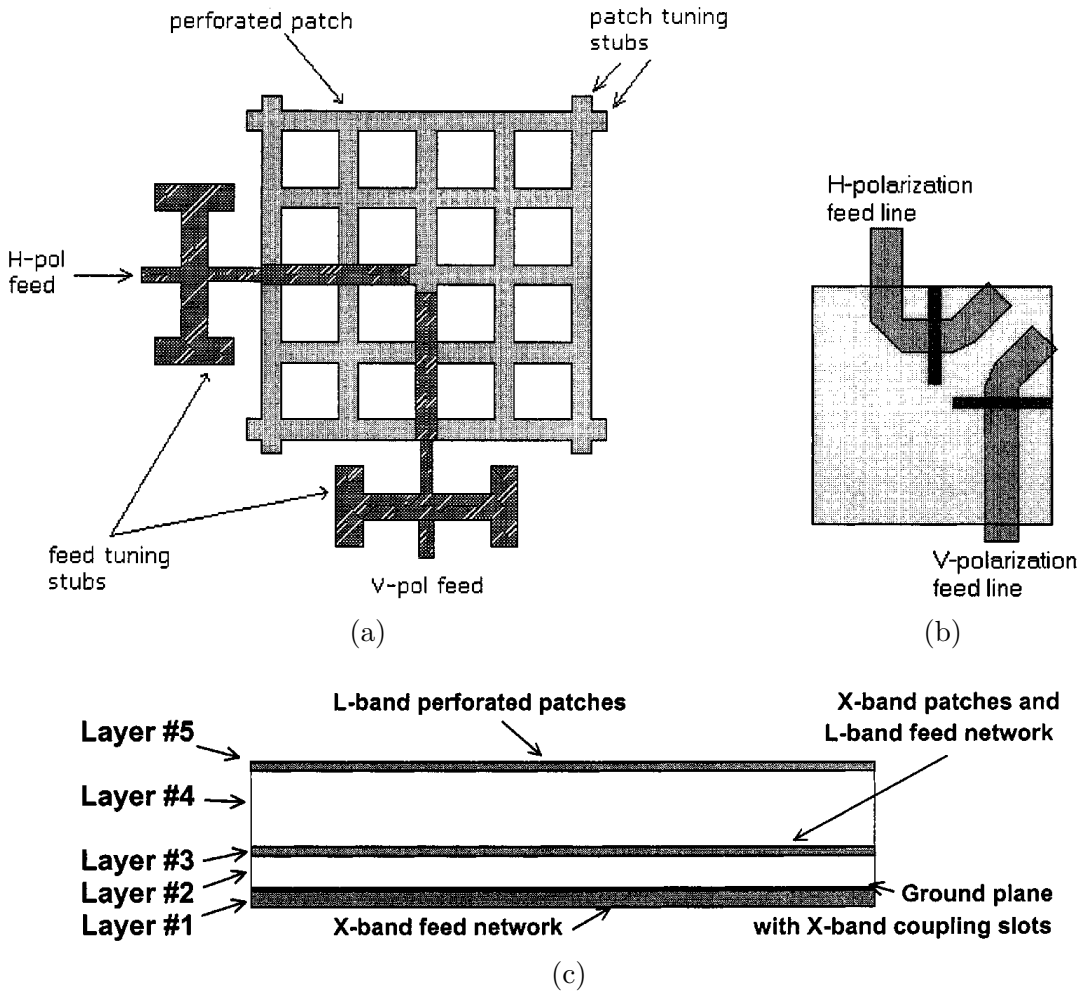

Figure 1.12: Geometry of the L-X-band SADBDP antanna array in [53]. (a) Basic subarray element, consisting of an L-band proximity-fed perforated patch and a 4×4 subarray of aperture coupled microstrip patches. (b) Geometry of the X-band dual-polarized aperture-coupled microstrip patch element. (c) Cross-sectional view of the multi-layered substrate configuration.

(PCB). Narrow frequency bandwidths of 6.5% and 3% are measured in L and X bands, respectively. Cross-polarization levels are −21 dB for both frequency bands. The reported aperture efficiency for X band is 40%.

Perforated patches are also used in [54] to design a SADBDP antanna for SAR applications. The operating frequencies are at the L and C bands with a frequency ratio of 1:4 and 100 MHz bandwidths in both bands. As shown in Figure 1.13, the

L-band elements are selected as perforated patches to enable the placement of the C-band elements within them. Stacked-patch configurations are used to meet the bandwidth requirements. Cross-polarization levels are better than -25 dB, due to the use of differential feeding scheme in the L-band and dummy slots in the C-band.

The SADBDP antenna reported in [55, 56] uses 2×1 microstrip dipoles and 7×4 square patches as the radiating elements at S and X bands, respectively (Figure 1.14). Parasitic elements are placed on top of the driven elements to reach the measured bandwidths of 9% and 17% for VSWR ≤ 2, in S and X bands, respectively. The measured cross-polarization levels are better than -26 dB for the S-band and -31 dB for the X-band. There are sixty SSMA coaxial connectors at the back of the 6-layer PCB which are connected to an external feed network through coaxial cables. This makes the overall design bulky and inefficient.

None of the antennas discussed above have the capability of frequency scanning. Introducing the frequency scanning functionality to the antenna array brings extra design challenges that will be discussed in Section 1.4.

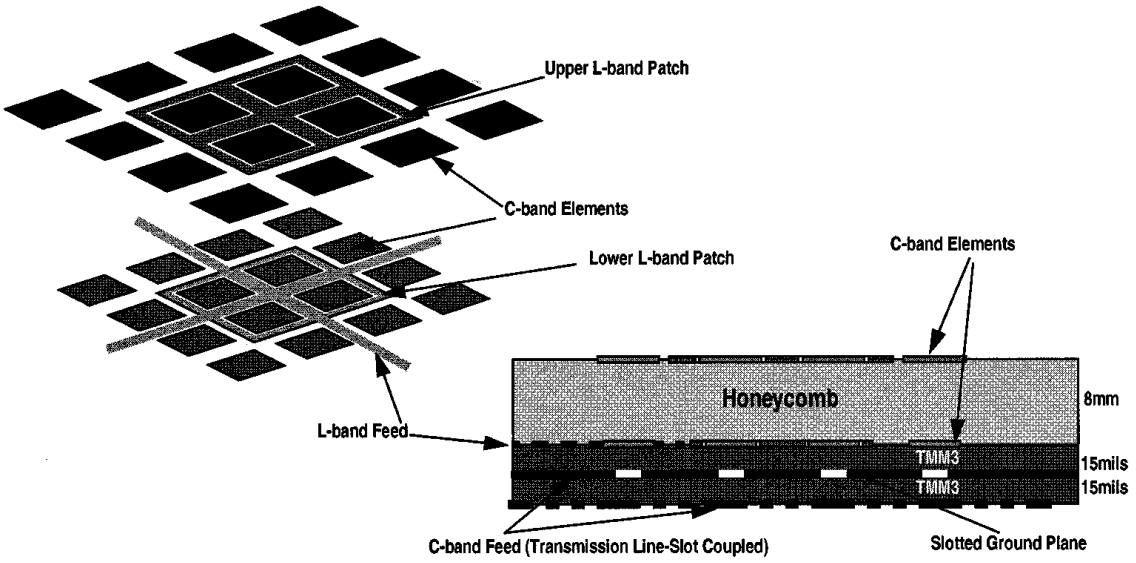

Figure 1.13: Geometry of the L-C-band SADBDP antanna array in [54]. Geometry of the stacked perforated L-band patches with 16 stacked C-band patches forming a unit cell. The full array consisits of 8×8 unit cells.

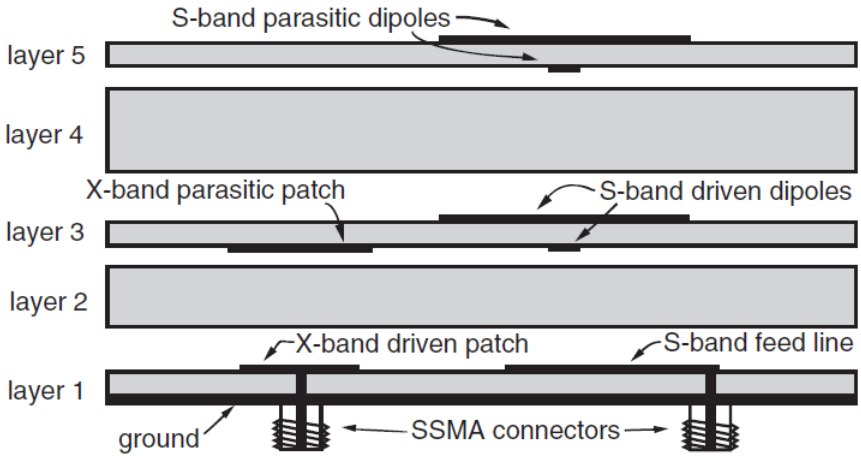

(a)

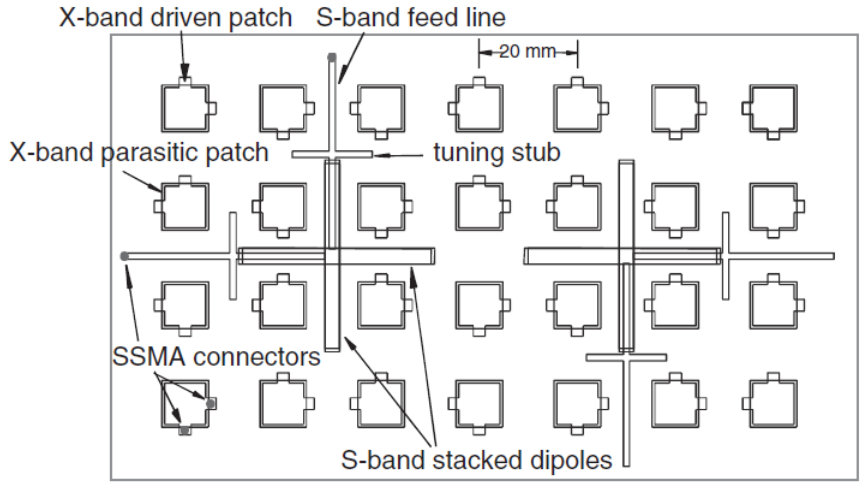

(b)

Figure 1.14: Geometry of the S-X-band SADBDP antanna array in [55]. (a) Side view. (b) Top view.

1.3 Objectives

The IWRAP system currently uses separate C-band and Ku-band microstrip phased arrays, each with two apertures—one vertically polarized and one horizontally polarized. The beam of these antennas can be frequency steered from 25° to approximately 55° incidence and mechanically rotated in azimuth at 60 rpm. Measurements have been nominally collected at four separate incidence angles (approximately 30°,

35°, 40°, and 50°), as shown in Figure 1.15 [14, 58]. This is accomplished by transmitting a waveform with frequency shifted pulses at frequencies corresponding to these angles and then simultaneously receiving the return signals from all beams and separating them using bandpass filters in the receivers. This enables IWRAP to collect measurements at four incidence angles without requiring it to time sequence the beams. A microwave pin diode switch on the antenna directs the transmit/receive signal to either the vertical or horizontal polarization port of the antenna.

Although these antennas provide ocean NRCS measurements at vertical and horizontal polarization, they have limitations, especially when acquiring measurements in the presence of precipitation. The major drawbacks of the antennas are: wide elevation beamwidth, small incidence angles and low efficiency. These issues limit IWRAP's capabilities to support DFS mission risk reduction efforts. Further, the dual aperture solution limits IWRAP to deployment on the NOAA WP-3D aircraft, and even for this aircraft, prevents other instruments—such as millimeter-wave radar

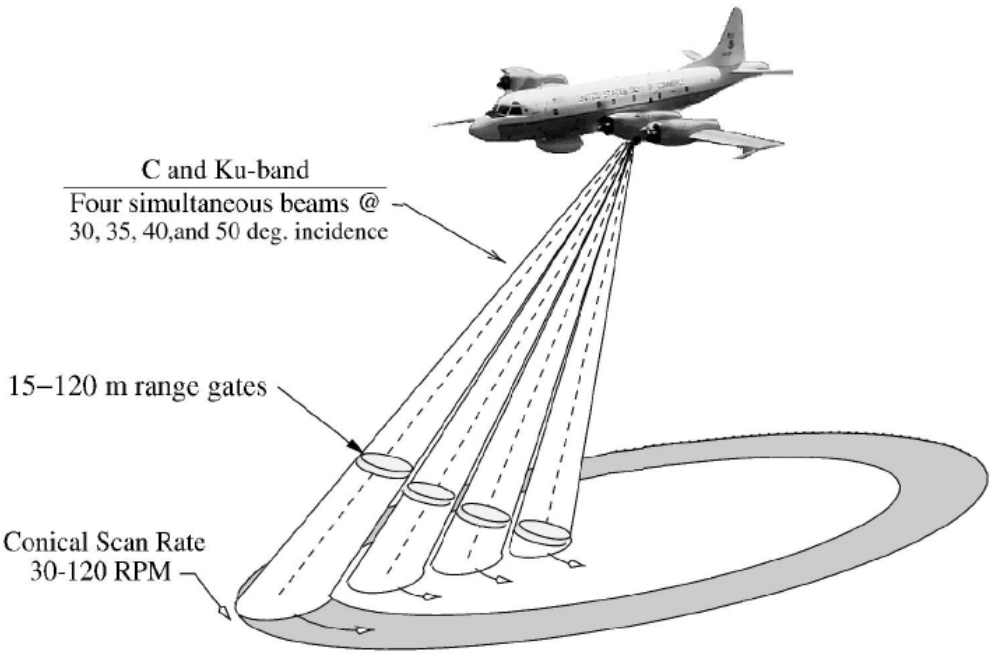

Figure 1.15: The measurement geometry of the IWRAP instrument [58].

that could provide additional information on clouds and precipitation—from being installed, since IWRAP antennas occupy the two largest available pressure dome regions.

In this research, we seek a shared-aperture antenna design solution capable of supporting IWRAP's C- and Ku-band frequencies and providing both polarizations at incidence angles in the range of 40° to 60°. It will be a part of the Advanced Wind and Rain Airborne Profiler (AWRAP), the next generation of IWRAP. This antenna will enable AWRAP to acquire the necessary measurements to support NOAA's DFS effort, provide high resolution ocean wind vector maps and enable more accurate retrieval and mapping of the precipitation bands and 3-D atmospheric winds within these bands. Further, with a single aperture solution, AWRAP could be significantly reduced in size and its performance substantially increased. This would enable AWRAP to be deployed on alternate aircraft such as the Avwatch aircraft to support SAR and other disaster reconnaissance missions. Besides, co-located apertures for C and Ku bands eliminate the onerous task of synchronizing incoming data stream from different antennas.

The specifications of the new frequency-scanning array technology with dual-band and dual-polarization capability in a shared aperture are summarized in Table 1.1.

Table 1.1: Target specifications of the shared-aperture frequency-scanning array

Frequencies	C-band: 5.0—5.6 GHz (11%)
	Ku-band: 13.1—14.5 GHz (10%)
Polarization	Dual linear
Cross-polarization level	-25 dB
Side-lobe level	-25 dB
Scan plane	$x - z$ plane
Scan range	40°—60° off broadside
Aperture efficiency	50% minimum
Aperture diameter	1.2 m

1.4 Challenges

Operating frequencies are widely separated and there is a 2.6:1 ratio between the center frequencies (i.e. 13.8 GHz and 5.3 GHz). To avoid grating lobes, different array element spacings are required. This implies that the optimal design demands an interleaved arrangement of elements at each band [53]. Therefore, four independent feed networks are required to distribute the power to the antenna elements for two frequency bands and two polarizations.

The avoidance of grating lobes (particularly at higher scan angles, i.e. 60° off broadside) places an upper limit on element spacings, while maximum element spacings are preferred to minimize cost. This precludes the use of dual-band or wide-band elements, such as spirals or notches [53]. Furthermore, significant mutual coupling effects are anticipated which can result in de-tuning antenna elements and decreasing return loss and radiation gain levels.

The major diameter of the array is given by 1.2 m which is very large for Ku band and can cause a significant loss in the series-feed line and a low aperture efficiency. Dividing the aperture to smaller units and careful transmission line selection is needed to minimize loss.

Furthermore, it is extremely difficult to achieve such low cross-polarization levels, especially in the upper end of the scan angle range, i.e. 60° off normal.

1.5 Contributions of This Work

The main contributions of this work can be listed as follows:

- *Design of the first shared-aperture dual-polarized array antenna with the capability of scanning the space with frequency in two bands:* Previous SADBDP arrays do not have the frequency-scanning capability.

- *Design of the array architecture:* The aperture is divided into subapertures and subarrays for modularity and low loss. Feeding structure and transmission lines are carefully chosen to minimize loss and volume.

- *Design, fabrication, and measurement of 3×3 Ku-band subarray:* The Ku-subarray consists of 3×3 dual-pol microstrip patch antennas and their feeding network. The radiation patterns and input impedances are measured. Waveguide simulation technique is used to measure the active impedance of the subarray.

- *Design, fabrication, and measurement of C-band slot antenna:* The antenna element in the C-band is a slot antenna on a metal plate excited by suspended stripline. The slot is covered with the Ku-subarray PCB for higher efficiencies. Its impedance and radiation characteristics are measured.

- *Design of dual-pol slot array for low cross-polarization level:* There are two orthogonal sets of slot arrays—one for each polarization. The proposed configuration guarantees that these two sets are interlaced symmetrically with minimal perturbation of each other's current paths. This keeps the cross-polarization levels low.

- *Design, fabrication, and measurement of a broadband waveguide-to-suspended stripline transition:* A perpendicular E-plane transition between rectangular waveguide and suspended stripline in the Ku-band is proposed. It uses a patch resonator on a double-sided single-layer dielectric substrate, combined with a cavity of a very shallow depth behind the resonator.

CHAPTER 2

ARRAY ARCHITECTURE

In this chapter, the architecture of the frequency-scanning array will be discussed.

2.1 Feeding Scheme

An extremely important part of any phased array system is the architecture by which the power from the transmitter is efficiently divided and distributed to the radiating elements, and vice versa for in the receive direction. The structure that performs this function is called the *array feed* [59].

Antenna arrays are usually either linear arrays or assemblies of linear arrays to make a planar array. Thus the linear array is a basic building block. When the elements are in parallel with a feed line or network, the array is termed *parallel*. Similarly, when the array elements are in series along a transmission line, the array is termed *series* [60]. Therefore, there are two basic feed networks that can be used to build arrays. These networks are shown in Figure 2.1.

2.1.1 Parallel Feed

The parallel-feed network is often called corporate-feed and is named after the structure of organization charts, where the feed divides into two or more paths, then each path divides, and so on. Such feeds are commonly binary, but sometimes the divider tree includes 3-way, or even 5-way dividers, depending upon the number of array elements [60]. Figure 2.1(a) shows a simple binary parallel feed. All paths—from the input port to each output port—are of equal length, which results in equal

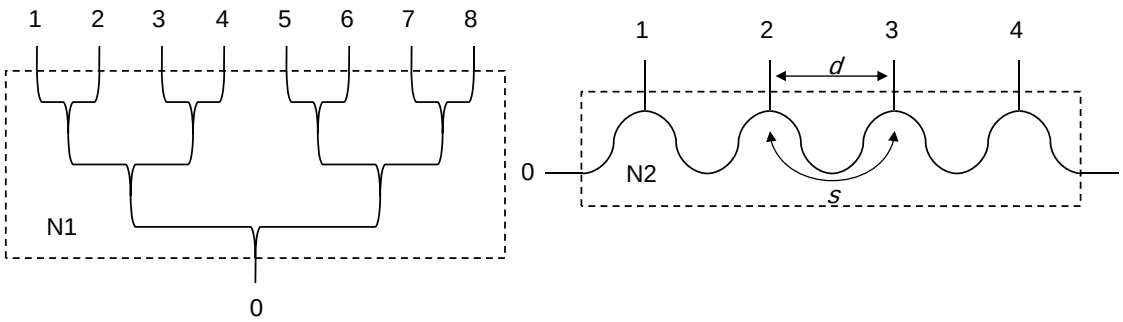

Figure 2.1: Basic feed arrangements of linear arrays. (a) Parallel feed. (b) Series feed.

phases at the outputs and maximum directivity in the broadside direction. For other scan angles, one should apply appropriate phase shifts at the output terminals using phaser elements. The power division ratio of each power divider can be deliberately determined to exhibit the desired taper in the amplitude of the aperture illumination [61].

The critical component in the corporate feed is the power divider (combiner); bifurcated T waveguide or coaxial-line T junctions, or hybrid junctions, can be used. Power dividers and hybrids can also be implemented in stripline or microstrip. The popular Wilkinson divider incorporates resistive loads to improve the match; it is commonly a stripline divider with the load across the separated lines. However, many microstrip patch arrays use the simple split line reactive power divider [60].

2.1.2 Series Feed

The series-feed network has radiating elements dispersed along a transmission line. The transmission line is fed at left end, with a load at the other end. It is matched at the right end to eliminate reflections and ensure an essentially pure traveling wave on the line. As the excitation wave travels along, the array part of it is radiated, leaving only a small part at the end to go to the load [60, 62].

Series-feed networks support traveling wave operation which is required for frequency scanning. The output phases are a function of frequency. The pahse difference between two adjacent elements is [59]

$$\phi = 2\pi f s/v \tag{2.1}$$

where f is the frequency, s is the length of line connecting adjacent elements, and v is the velocity of wave propagation in the line. Generally, s is greater than the distance d between elements and the feed line should be meandered. Meandered feed lines are sometimes called *snake* or *serpentine* feed.

At one particular frequency, all output terminals are in phase, i.e. $\phi = 2m\pi$, with m being an integer. At this frequency, denoted as f_0, the beam points to broadside. As the frequency is changed, the phase across the aperture tilts linearly, and the beam is scanned [63]. The direction of beam pointing can be written as [59]

$$\sin\theta = \frac{s}{d}\left(1 - \frac{f_0}{f}\right) \tag{2.2}$$

where θ is measured from broadside.

2.1.3 The Planar Array

The parallel- and series-feed networks can be combined to build 2-D aperture arrays with frequency scanning in one of the planes. Two possible array architectures are sketched in Figure 2.2. The scan plane is perpendicular to the array plane along the series-feed network.

Figure 2.2(a) is a combination of a single parallel feed and number of series feeds. Parallel feed is shown in the vertical dimension, and in the horizontal dimension series feeds are shown. This is called a *parallel-series* feed.

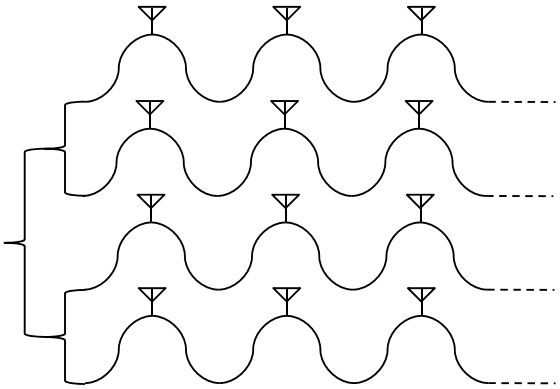

(a)

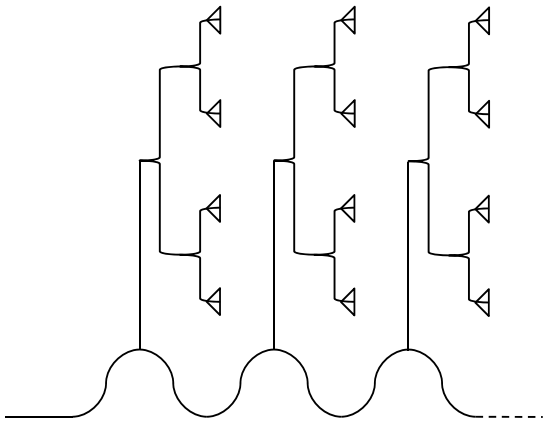

(b)

Figure 2.2: Two potential array architectures of 3×4 array that support frequency scanning in one plane. (a) Parallel-series feed. (b) Series-parallel feed.

The architecture shown in Figure 2.2(b), on the other hand, uses a single series feed in the horizontal dimension, and the power in each column is distributed with a parallel feed. This is called a *series-parallel* feed.

Series-parallel feed needs more power dividers, whereas parallel-series feed requires more snake feed. In this work, we prefer the parallel-series feed, because they require less less number of power dividers, which are very bulky and expensive, especially in the waveguide form.

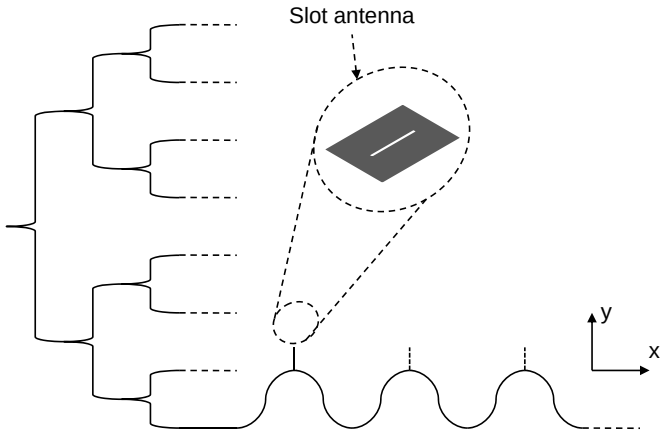

(a)

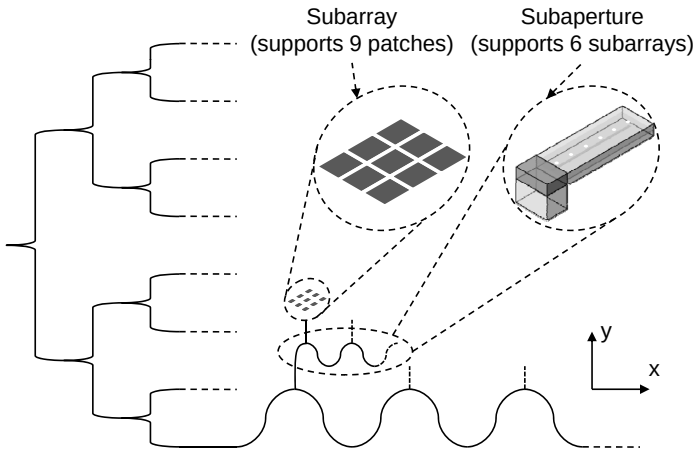

(b)

Figure 2.3: The proposed array architectures for each polarization. (a) C-band. (b) Ku-band.

Figures 2.3(a) and 2.3(b) show the architecture of the array in this work for each polarization for C and Ku bands, respectively. For C-band, we use a parallel-series feed network. The power dividers are in the waveguide (WG) form, the series-feed networks are suspended striplines (SSL), and the antenna elements are slots.

The architecture for Ku-band is slightly different. It is also a parallel-series feed network, but it utilizes *subarrays* and *subapertures*. In general, such hierarchical partitioning makes possible cost-effective prototyping and simplifies manufacturing

of the whole array, especially when the aperture size is very large compared to the dimensions of the antenna element. It also allows us to control the loss by using the appropriate transmission line for each hierarchical level. In Ku band, the power dividers are in the WG form and antenna elements are microstrip (MS) patches. The series feed networks are WG in the array level, SSL in the subaperture level and stripline (SL) in the subarray level. Note that although waveguides are very low-loss, they are extremely bulky and are not appropriate for lower levels of the hierarchy such as subapertures and subarrays; particularly in this work, where four feed networks need to be arranged under the radiating elements.

2.2 Radiating Elements

There are many kinds of radiating elements commonly used in phased arrays: dipoles, slots, open-ended waveguides, TEM horns, spirals, helices, and microstrip patch elements. The selection of an element for a particular application must be based on the following considerations [64]:

1. *Size:* The required area of the element should be small enough to fit within the allowable element spacing and lattice without generating grating lobes.

2. *Physical construction:* Elements must be able to withstand environmental requirements such as thermal, shock, and vibration requirements. In addition, they must be lightweight enough for the array's mission.

3. *Polarization purity:* Cross-polarization levels of arrays are closely related to the polarization purity of their radiating elements. Therefore, it is important that antenna elements have low cross-polarization levels.

4. *Compatibility with feeding network:* The array architecture specifies the feeding network. Radiating elements should be able to be driven by the feeding network conveniently.

5. *Frequency bandwidth:* Bandwidth of the radiating elements should meet the requirements of the array bandwidth.

6. *Cost, reliability, and repeatability:* Many hundreds or thousands of elements are required to build the entire array. Thus, fabrication of elements must be inexpensive, and their performance must be reliable and repeatable from unit to unit.

For the application of this work, which is deployment on an aircraft or even on satellites, the size and weight of the array is of great importance. Besides, it will be shown in Section 2.6 that element spacings are very tight: 0.39 λ at Ku-band, and 0.45 λ at C-band. Therefore, bulky or massive radiating elements such as open-ended waveguides, spirals, helices etc. are not suitable.

The frequency bandwidth of this array is about 10% which can be achieved with many resonant antenna elements such as dipoles, slots, and microstrip patch elements. There is no need to use very wideband but bulky elements like TEM horns, helices, log-periodic antennas etc.

More importantly, antenna elements must utilize a shared aperture for both frequencies and both polarizations. As previously stated, the antenna elements are interleaved. Some works have modified two-dimensional elements to fit them in the same aperture. For example [53, 54] have used perforated microstrip patches for one band and conventional patches for the second band. Another solution would be using one-dimensional antenna elements, such as slots or dipoles, at least for one band.

Dipoles and slots are resonant antennas and are $\lambda/2$ long, which is larger than the element spacings of this work. However, physically shorter slot antennas can be made resonant or near-resonant using some techniques, one of which is discussed in Section 5.5. Feeding mechanism of slots are very straightforward. For example, a simple cut on the ground plane of an SSL is a slot antenna, as long as it effectively

disturbs the current path. Polarization purity of slot antenna is excellent, and its frequency bandwidth is adequate for this work.

Microstrip patch antennas are very compact and cost effective. They are highly preferred in aircraft, spacecraft, satellite, and missile applications, where size, weight, cost, performance, ease of installation, and aerodynamic profile are constraints [61]. They are widely used in phased array systems because of their simplicity and compatibility with printed-circuit technology, making them easy to fabricate in large scale. There are many configurations that can be used to feed patch antennas: via microstrip line, coaxial probe, aperture coupling and proximity coupling [61]. The frequency bandwidth of patch antenna is adequate for this work, especially if thick substrates are used. The major operational disadvantage of patch antenna is its poor polarization purity [61], which can be alleviated using some techniques, one of which is discussed in Section 3.7.

For the above reasons, we choose patch and slot antennas as the radiating elements for this work. Slots can be cut in the extended ground plane of patch antennas. There must not be any metal between the slot and free space. Hence, slots must be placed between patch elements, which means that the spacing between slot elements should be larger than the patch dimensions. Consequently, we need to use slots in the lower band (i.e. C-band) and patches in the upper band (i.e. Ku-band). Following section illustrates and describes the configuration.

2.3 Aperture Sharing

Figure 2.4 illustrates a portion of the candidate design for a SADBDP frequency-scanning array antenna. The primary objective of the proposed array design is to utilize the given circular aperture area as efficiently as possible for both C (5.3 GHz) and Ku (13.8 GHz) bands by sharing the aperture. In both bands, the array is capable of forming and scanning a narrow beam in the $x - z$ plane in the range 40°—60° off

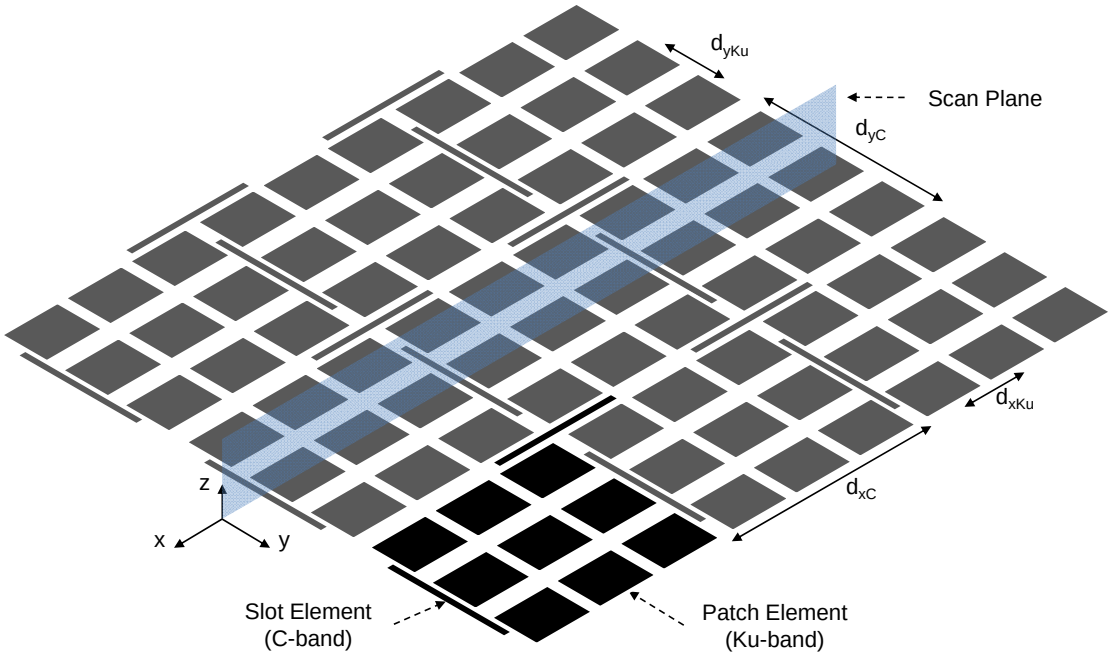

Figure 2.4: Arrangement of the radiating elements in the proposed shared-aperture C-Ku dual-band frequency-scanning array antenna. A subarray is indicated in a darker tone.

normal for both vertical and horizontal polarizations. A more detailed illustration of the array is shown in Figure 2.5. In addition to the radiating elements, it also shows the transmission lines which feed them. A cross sectional view will be presented and discussed in the next section.

Dual-polarized Ku-band microstrip patch antennas and perpendicular C-band slot antennas share the aperture. Microstrip patches sit on a low-permittivity substrate and the slots are formed in the aluminum housing. The C-band slots are positioned between Ku-band patches every third patch spacing. The element spacings in the Ku band are d_{xKu} and d_{yKu} in the $\hat{x}$ and $\hat{y}$ directions, respectively. Those spacing for the C-band slots are d_{xC} and d_{yC}.

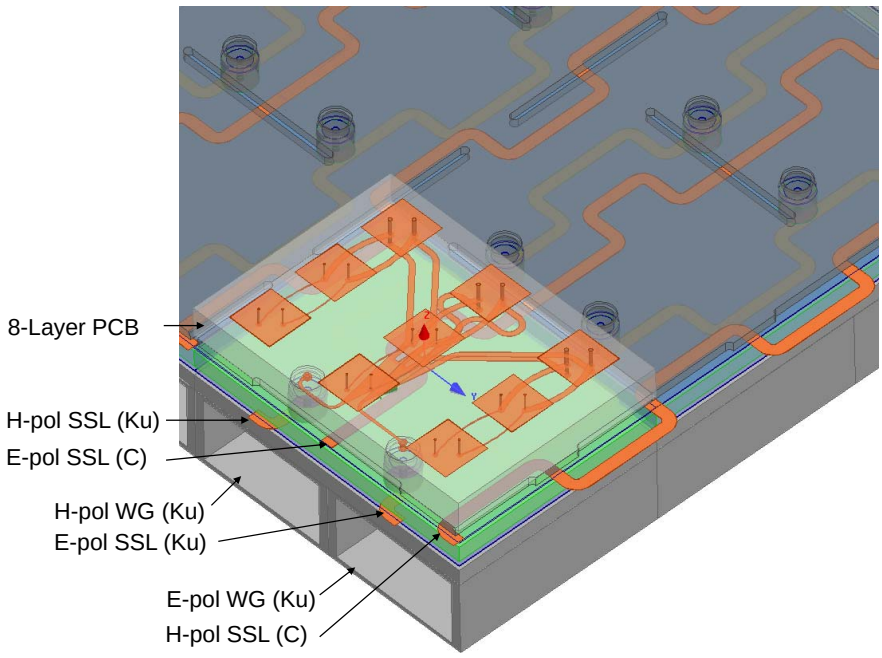

Figure 2.5: Simplified 3-D model of the array antenna showing the radiating elements and feed networks. The Ku-band 8-layer PCB is only shown for one subarray.

2.4 Subarray

A subarray consists of nine Ku-band microstrip patch antennas and two C-band slot antennas, as indicated in Figure 2.4 by a darker tone. One of the slot antennas is in the $\hat{x}$ direction for H-polarized radiation and the other one is in the $\hat{y}$ direction for E-polarized radiation. All of the nine square microstrip patch antennas are dual-polarized. The subarray shares all four boundaries with identical neighboring subarrays.

The C-band slots are fed by the underlying SSL. The Ku-band patches are divided into three groups of three series-fed square patches. Each patch element has two probe feeds for E- and H-polarized radiations. The side view of a single subarray is illustrated in Figure 2.6. There are a total of 12 circuit layers. The configuration and function of each layer is described as follows:

1. *Layer 1:* Nine dual-polarized Ku-band square patches are exposed to air.

2. *Layer 2:* Ground plane

3. *Layer 3:* This is a stripline layer that contains series (combline) feed-lines for the Ku-band patches. There are a total of six comblines, three for each polarization.

4. *Layer 4:* Ground plane

5. *Layer 5:* This layer contains an SL 1:3 in-phase power division circuit for the E polarization of the Ku-band. The three output ports are connected to the series feed network in layer 3.

6. *Layer 6:* Ground plane

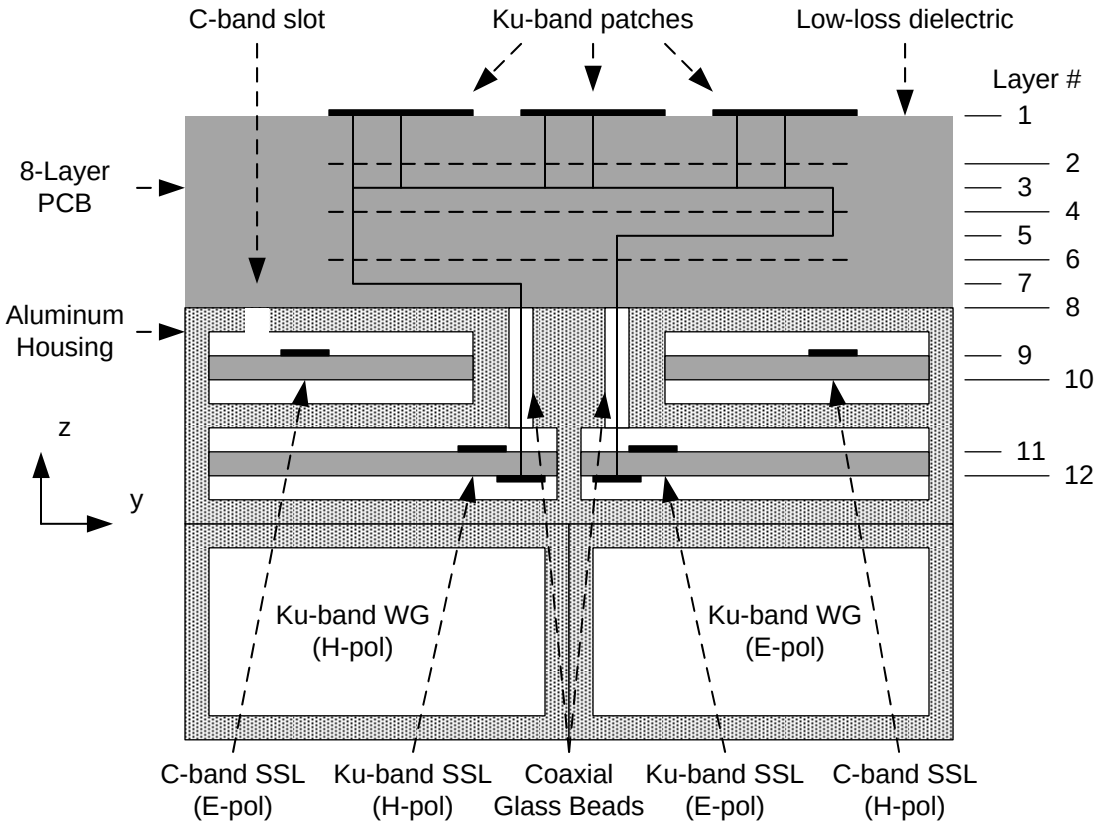

Figure 2.6: A cross sectional view of the subarray, from the running direction of the underlying transmission lines, $\hat{x}$. The drawing is not to scale.

7. *Layer 7:* This layer contains an SL 1:3 in-phase power division circuit for the H polarization of the Ku-band. The three output ports are connected to the series feed network in layer 3.

8. *Layer 8:* Ground plane. This layer will be attached to the aluminum housing with silver epoxy to provide electrical connection between the aluminum housing and the ground planes of the Ku-band 8-layer PCB.

9. *Layer 9:* This layer has the two underlying SSLs for feeding two C-band slot antennas, one for each polarization. A conducting wall is seperating the two transmission lines to enhance isolation between them.

10. *Layer 10:* Empty layer

11. *Layer 11:* This contains two underlying Ku-band SSLs, one for each polarization. To enhance isolation between the two transmission lines, a conducting wall is placed between them. For each SSL, a small amount of power is coupled off to feed the nine Ku-patch subarray. There is a double-layer coupled-line coupler on layers 11 and 12 for this purpose.

12. *Layer 12:* Once a small power is coupled off the main SSL on layer 11, it goes through two coaxial glass beads to feed the 1:3 power dividers on layers 5 and 7. The coaxial glass beads are embedded inside cylindrical aluminum posts.

For C-band slots, the underlying SSL directly feeds them. However, for Ku-band, there are three distinct stages for power coupled off the main transmission line to arrive at the patch elements: an SSL coupler in layers 11 and 12, a 1:3 power splitter in layers 5 or 7, and an SL series feed beamformer circuit in layer 3.

2.5 Subaperture

Metallic waveguides feature extremely low losses and are best suited for feeding large apertures. Their major drawback is large dimensions. The SSL, on the other hand, has a compact form factor and is suitable for feeding small apertures or subapertures. However, their transmission loss is higher than the loss of WGs and makes them impractical for large apertures. Thus, a practical design may result from a compromise between these two transmission media. In this research, we use WGs in the aperture level and SSLs in the subaperture level. That will be discussed in more detail in Section 2.7.

A subaperture contains six subarrays along the $\hat{x}$ direction (see Figure 2.3(b)). The architecture of the subaperture is shown in Figure 2.7. The input of a subaperture is a WR-62 waveguide. A waveguide-to-suspended stripline (WG-SSL) transition converts the transmission medium to SSL.

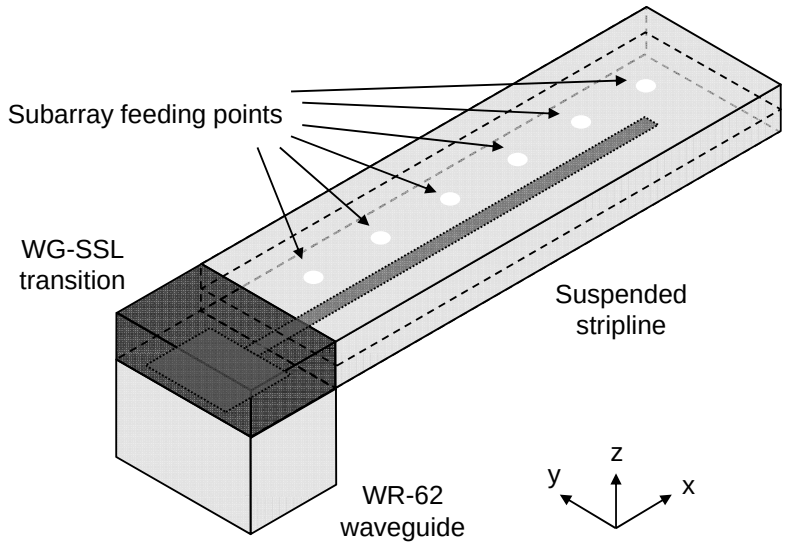

Figure 2.7: Architecture of the subaperture.

2.6 Element Spacing

For both C-band and Ku-band arrays, the frequency scanning function can be achieved using traveling-wave series-feed network sections like that in Figure 2.1(b). For this, we define a slow-wave factor

$$\gamma = \frac{k_g}{k_0}\frac{s}{d} = \frac{s/\lambda_g}{d/\lambda} \tag{2.3}$$

that accounts for all involved parameters such as

- s: path length inside transmission line
- λ: free-space wavelength
- λ_g: guided wavelength inside transmission line
- d: radiator interelement spacing
- k_0: free-space phase constant
- k_g: guided phase constant

The vector wavenumber corresponding to the (m,n)th-order Floquet mode is

$$\begin{aligned}\mathbf{k}_{mn} = \hat{x}\left(k_{sx} + \frac{2m\pi}{d_x}\right) + \hat{y}\left(k_{sy} + \frac{2n\pi}{d_y}\right) \\ + \hat{z}\sqrt{k_0^2 - \left(k_{sx} + \frac{2m\pi}{d_x}\right)^2 - \left(k_{sy} + \frac{2n\pi}{d_y}\right)^2}\end{aligned} \tag{2.4}$$

where m and n are integers and

$$k_{sx} = k_0 \sin\theta_s \cos\phi_s \tag{2.5}$$

$$k_{sy} = k_0 \sin\theta_s \sin\phi_s \tag{2.6}$$

are associated with the scan direction given by (θ_s,ϕ_s). For the $x-z$ plane scanning conditions of this research where $\phi_s = 0$, and for $n = 0$, above formulas reduce to

$$\mathbf{k}_m = \hat{x}\left(k_{sx} + \frac{2m\pi}{d_x}\right) + \hat{z}\sqrt{k_0^2 - \left(k_{sx} + \frac{2m\pi}{d_x}\right)^2} \tag{2.7}$$

and

$$k_{sx} = k_0 \sin\theta_s. \tag{2.8}$$

The relationship between the slow-wave factor and the $\hat{x}$-directed component of $\mathbf{k}_m$ is

$$\mathbf{k}_m \cdot \hat{x} = \gamma \times k_0. \tag{2.9}$$

The guided wavenumber (or phase constant) of the underlying transmission line of either fast or slow wave nature, the spacing between neighboring elements, and possible phase reversal between consecutive elements determine the scan angle and its frequency sensitivity. The objective of dual C- and Ku-band dual linear-polarized frequency-scanning array is to scan 40°—60° off broadside in both bands for both polarizations.

Some numerical calculation has been performed to find the optimal frequency scanning configuration. As mentioned before, the series feed network inside the Ku-band subarray consists of cascaded SL delay-lines. The dielectric constant of the Ku-subarray PCB is given by $\epsilon_r = 2.94$ (the material choice will be discussed in chapter 3). Therefore, the slow-wave factor for the Ku-band, γ_{Ku}, should be greater than $\sqrt{\epsilon_r} = 1.71$. Since for the same sweep sensitivity (the slope of scan angle versus frequency curve), larger γ needs a shorter element spacing and that results in higher mutual coupling, we will remain close to this bound. In order to leave some room for fine tuning the phase, we choose $\gamma_{Ku} = 1.8$.

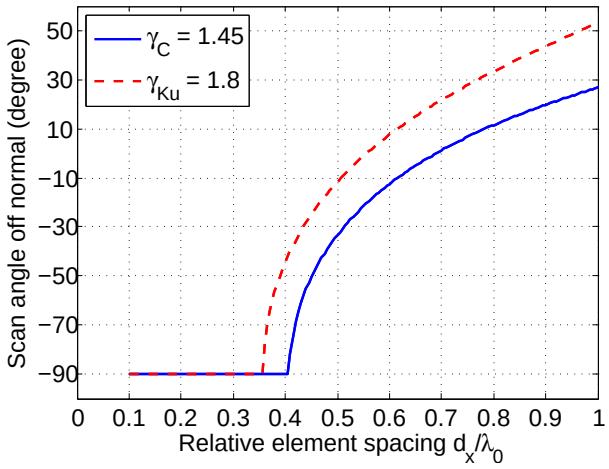

Figure 2.8: Scan angle with respect to relative element spacing for $m = -1$ Floquet-mode. Negative scan angle means the main beam in the backward direction from the underlying transmission line.

For the chosen γ_{Ku} and for the $m = -1$ Floquet-mode propagating wave (backward firing), Figure 2.8 shows the scan angle θ with respect to the element spacing. Consider an element spacing of

$$d_{xKu} = 0.39\lambda_{ku} = 8.50 \text{ mm} \tag{2.10}$$

at center frequency 13.8 GHz. A frequency variation of 10% makes the fixed spacing vary from $0.37\lambda_{Ku}$ to $0.41\lambda_{Ku}$ and scan the main beam from $-60°$ to $-40°$. This element spacing is less than a half wavelength and grating lobes will be avoided. Since there is no scanning in the $y - z$ plane, we can afford to have a slightly larger subarray dimension in the $\hat{y}$ direction, without worrying about grating lobes. As long as it is not greater than λ_{Ku}, a larger dimension in the $\hat{y}$ direction is desirable in order to accommodate all feeding mechanisms. We choose

$$d_{yKu} = 0.55\lambda_{ku} = 12.0 \text{ mm} \tag{2.11}$$

at $f = f_{Ku} = 13.8$ GHz.

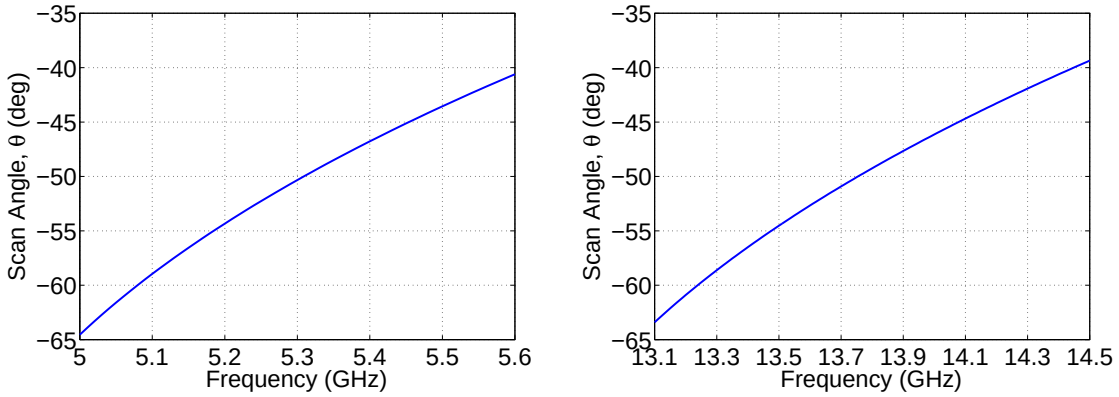

(a) (b)

Figure 2.9: Scan angle as a function of frequency. (a) C band: $d_{xC} = 25.5$ mm and $\gamma_C = 1.45$. (b) Ku band: $d_{xKu} = 8.5$ mm and $\gamma_{Ku} = 1.8$.

The C-band element spacings d_{xC}, d_{yC} are exactly three times the Ku-band element spacing, i.e.

$$d_{xC} = 3 \times d_{xKu} = 25.5 \text{ mm} = 0.45\lambda_C \tag{2.12}$$

$$d_{yC} = 3 \times d_{yKu} = 36.0 \text{ mm} = 0.64\lambda_C \tag{2.13}$$

at $f = f_C = 5.3$ GHz. The element spacing in the $\hat{x}$ direction is less than a half wavelength and grating lobes will be avoided. For the $d_{xC} = 0.45\lambda_C$ spacing, a phase factor of $\gamma_C = 1.45$ results in a high sweep sensitivity. Figure 2.8 shows that a beam can be scanned in the desired angular range for the spacing d_x between $0.43\lambda_0$ and $0.47\lambda_0$ in terms of the free-space wavelength λ_0. That corresponds to a 9% frequency variation. Figure 2.9 shows the scan angle of the array as a function of frequency for both C and Ku bands.

2.7 Slow-wave Structure

The two slow-wave phase factors of 1.45 and 1.8 can be realized using various configurations of transmission lines. Note that the phase factor of a straight transmission line can be adjusted accurately (in the increasing direction) by meandering it. For

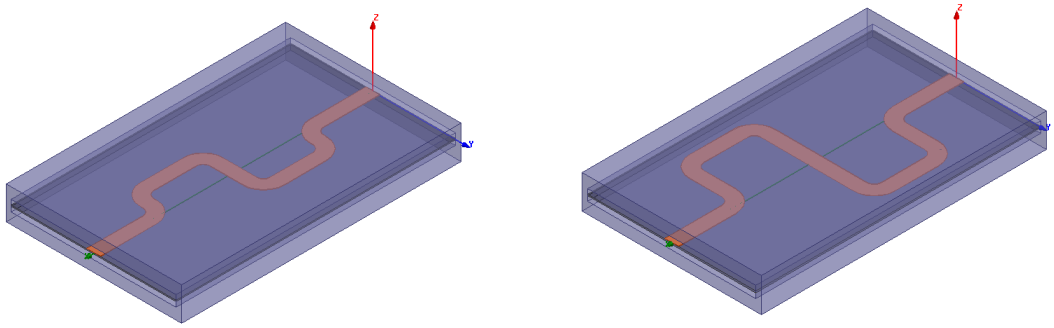

(a) (b)

Figure 2.10: Ansys HFSS models of the slow-wave SSLs. Meandered copper traces are etched on thin RT/duroid 5880 substrates and placed inside aluminum housings. (a) C-band. (b) Ku-band.

the phase factor of 1.45 in the C-band, we will only use a meandered SSL. For the phase factor of 1.8 in the Ku-band, we will use slow-wave WG in the aperture level, meandered SSL in the subaperture level and meandered SL in the subarray level.

A low-loss high-frequency laminate RT/duroid 5880 ($\epsilon_r = 2.2$, $\tan\delta = 0.0009$) from Rogers Corporation [65] has been selected for the proposed realizations of the underlying C- and Ku-band transmission lines. To assess the propagation loss of C- and Ku-band SSLs, numerical analysis has been performed at the band center frequencies 5.3 GHz and 13.8 GHz using Ansys HFSS. Figure 2.10 shows the 3-D models for the C- and Ku-band SSLs.

In Figure 2.10, the substrate thickness is equal to $t_{sub} = 0.127$ mm and the thickness of the copper trace is $t_{cond} = 0.035$ mm (1 oz. cladding). The total height of the stripline (separation between the top and bottom grounds) is $h = 1$ mm. The distances between the input and output ports in the x-direction are equal to $d_{xC} = 3 \times d_{xKu} = 25.5$ mm. Both transmission lines are meandered to achieve the desired phase factors, $\gamma_C = 1.45$ and $\gamma_{Ku} = 1.8$.

At $f = 5.3$ GHz, a transmission-line loss of 0.044 dB is observed between the two ports in simulation. This corresponds to a loss of 1.72 dB/m. The C-band loss is low

enough that a single SSL over the entire diameter 1.2 m of the array aperture will cause a loss of 2.07 dB. Ideally, a single SSL can run the entire aperture diameter and feed all the C-band elements. However, in practice, the longest lengths of available dielectric substrates and machined aluminum housings will determine the maximum length of the individual C-band transmission line segments. Several segments will be cascaded to cover the entire aperture.

The simulated transmission-line loss at $f = 13.8$ GHz is given by 0.13 dB which corresponds to a loss of 5.1 dB/m. The Ku-band loss is high, and dividing the array into subapertures and utilizing waveguide feeds are necessary. Several Ku-band subapertures will have to be cascaded to run the 1.2 m diameter of the entire circular aperture.

The main reason that we prefer SSL over MS line for the the series-feed line, despite its fabrication hardship, is the transmission loss. To show the difference, we simulated the transmission loss of MS line too. The MS line was meandered by the amount to make the electrical length correspond to the required phase factor of 1.8 at Ku band. Simulation results showed that the insertion loss of MS line at $f = 13.8$ GHz is 10.6 dB/m, 5.5 dB more that that of SSL. Clearly, MS lines are very lossy for the purpose of this array where 50% of antenna efficiency is required.

Figure 2.11 illustrates the geometry and feeding methods for the two underlying transmission lines and their aluminum housings. It is based on a stacked geometry with the guide for the C-band SSL above the guide for the Ku-band SSL. As shown in Figure 2.11, a C-band guide (aluminum housing) is fed straight from one end at the array aperture boundary. A direct straight connection for both the aluminum guide and the suspended stripline is made to the next section. On the underside of a C-band guide, several isolated Ku-band guides are arranged. Each Ku-band stick is fed at right angle at one end via a WG-SSL transition.

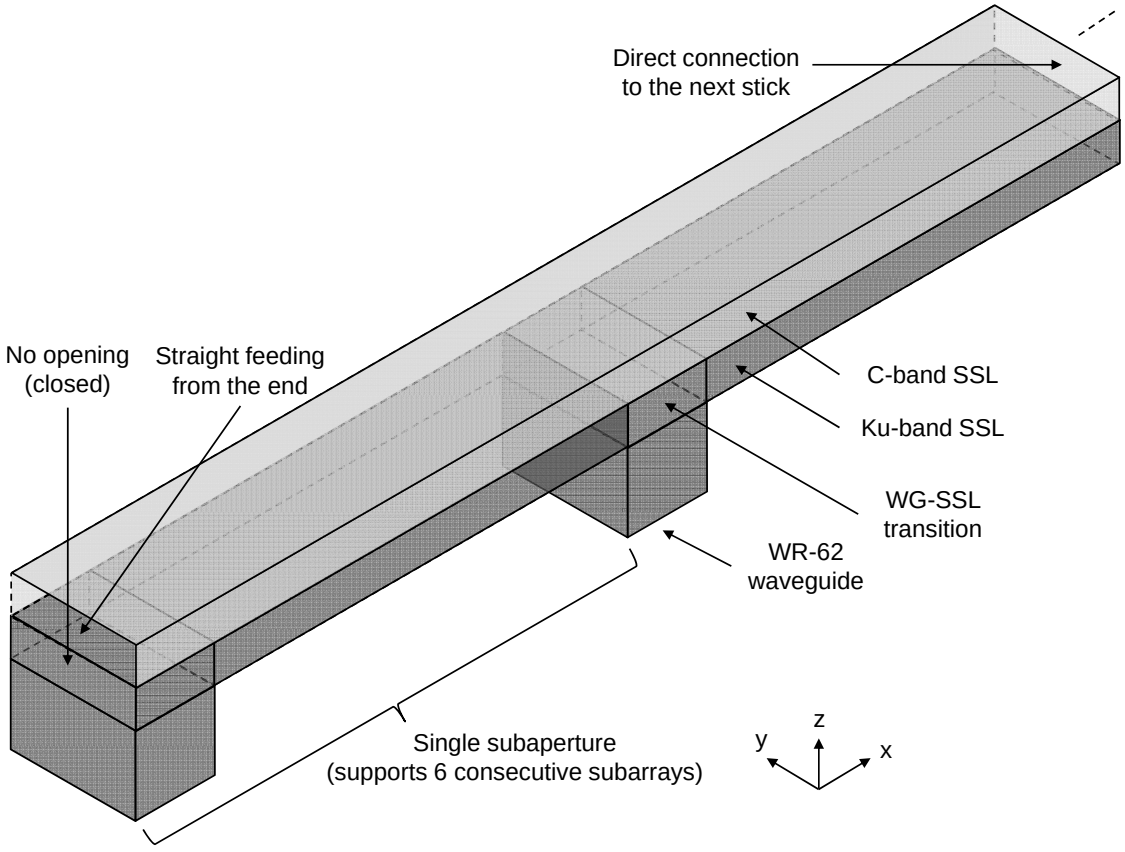

Figure 2.11: A stacked aluminum housing and feeding configuration for the C- and Ku-band transmission line.

CHAPTER 3

KU-BAND SUBARRAY

In this chapter, the design and simulation of the frequency-scanning subarray for Ku band, namely the *Ku-subarray*, will be discussed. The signal layer metalizations and the stack-up of the Ku-subarray are shown in Figure 3.1. The Ku-subarray consists of eight layers of copper cladding with Rogers RT/duroid 6202 and 2929 Bondply materials in-between as the core and the prepreg, respectively [66, 67].

The coefficient of thermal expansion (CTE) of RT/duroid 6202 is 30 ppm/°C in the $\hat{z}$ direction, which makes it more suitable for multilayer PCB fabrication, compared to other low-loss materials like RT/duroid 5880 with a CTE of 237 ppm/°C. CTE describes how much a PCB expands as it is heated or cooled. Large CTE results in excessive expansion of the dielectric in multiple registration steps in fabrication, which in turn puts more stress on the vias—usually made of copper with CTE of 18. Excessive stress can break the via connections.

Fabrication of the 8-layer PCB was a challenging task. In order to mitigate parallel-plate propagation modes between ground planes, they must be connected to each other using numerous vias. On the other hand, the ground vias must not penetrate signal circuitry which is not always achievable with through-hole vias. Hence, the use of blind and buried vias was inevitable which increases the complexity of manufacturing process. This process is described in Appendix B.

The functions of each layer were described in Section 2.4. The design and simulation of each circuit layer will be discussed in more detail in the following sections.

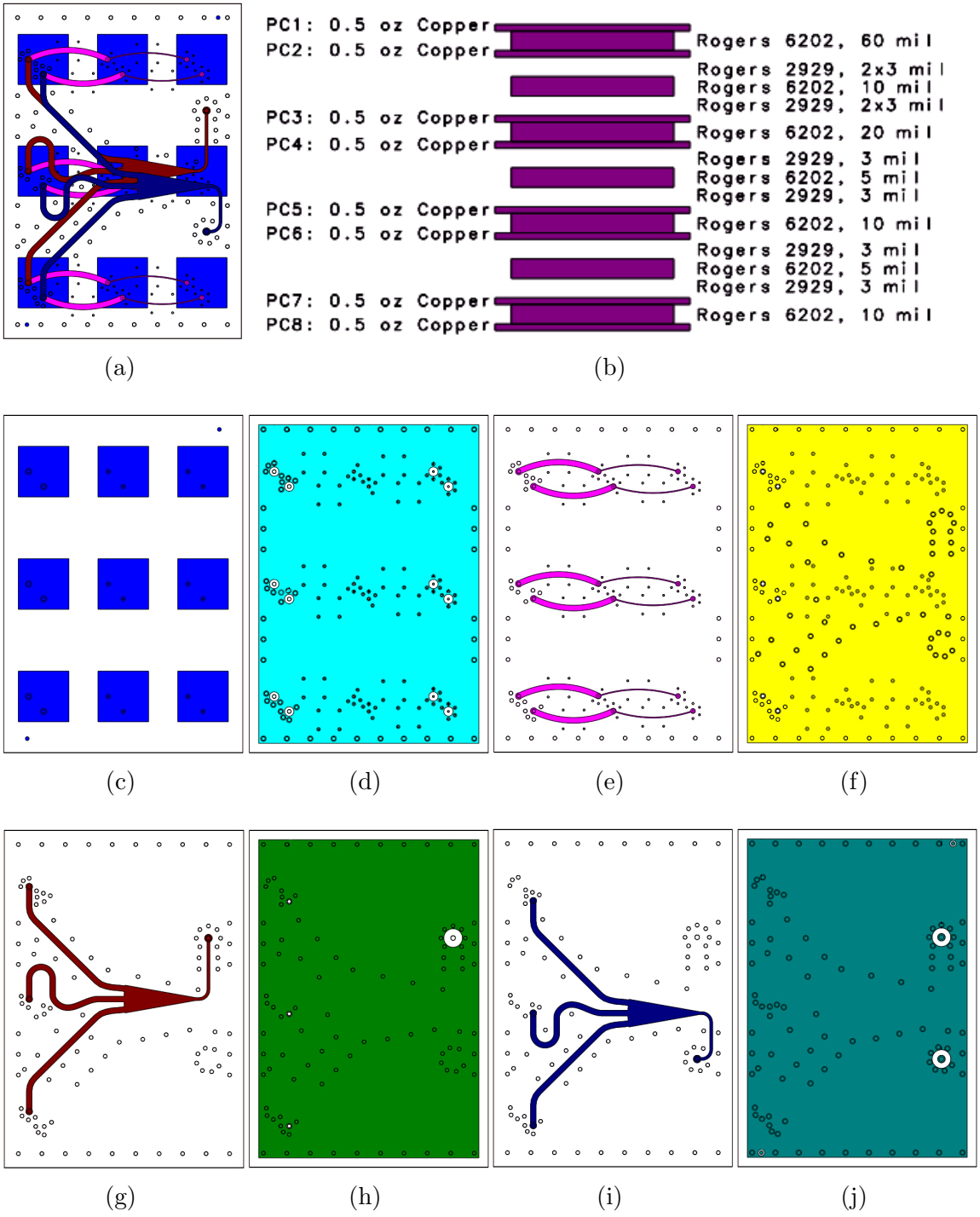

Figure 3.1: Ku-subarray. (a) Metal layers. Each layer is indicated with a different color. Ground planes are invisible. (b) Stack-up (c) Layer 1: 3×3 array of patch elements. (d) Layer 2: Ground plane. (e) Layer 3: 1:3 series feed networks. (f) Layer 4: Ground plane. (g) Layer 5: 1:3 parallel power divider for E-polarization. (h) Layer 6: Ground plane. (i) Layer 7: 1:3 parallel power divider for H-polarization. (j) Layer 8: Ground plane and input ports.

3.1 Patch Antenna

Microstrip patch antennas are widely used in the antenna arrays because of the simplicity of fabricating printed-circuit boards (PCBs) in large scales. In Section 2.2, it was discussed how a microstrip patch element is a great candidate for the application of this work. Some microstrip patch arrays were reviewed in Section 1.2.2. The simplest microstrip antenna consists of a patch of metal, usually rectangular or circular on top of a grounded substrate.

As shown in Figure 3.2, the frequency bandwidth increases with the substrate thickness and inversely with the substrate permittivity ϵ_r [68]. Thus, by using thicker low-permittivity substrates, one can increase the bandwidth at the expense of increased lateral size and vertical thickness. The material choice (Rogers RT/duroid 6202) was discussed at the beginning of this chapter. The standard thicknesses for this material are 5, 10, 15, 20, 30, and 60 mil [66]. Its relative permittivity and loss are given

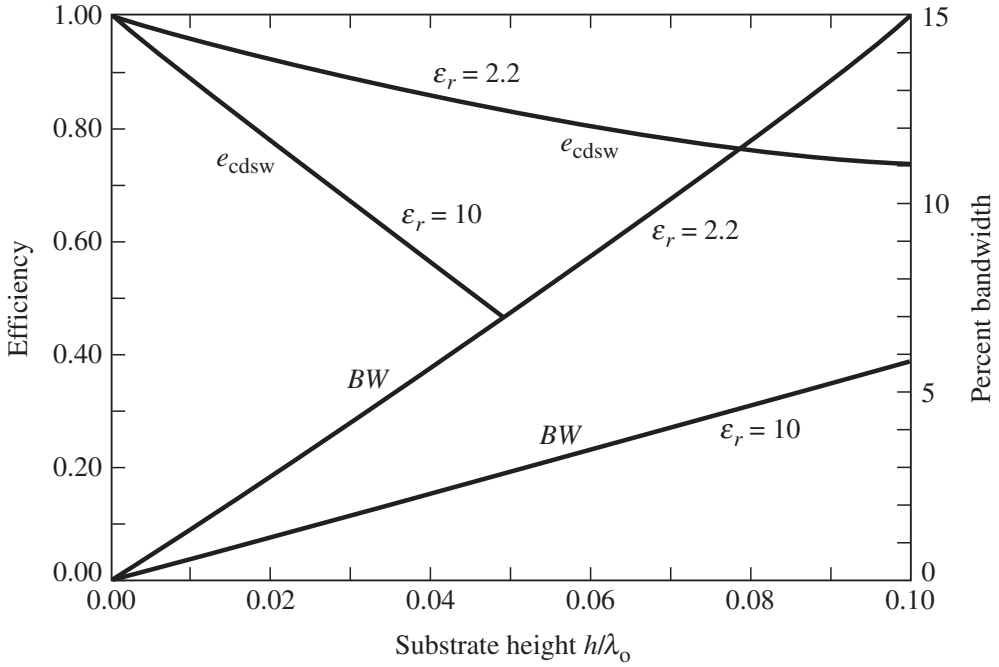

Figure 3.2: Efficiency and bandwidth versus substrate height at constant resonant frequency for a probe-fed rectangular microstrip patch for two different substrates [61, 68].

by $\epsilon_r = 2.94$ and $\tan\delta = 0.0015$, respectively. Substrate height of 60 mil (1.524 mm) is equivalent to $h/\lambda_0 \approx 0.1$ at $f = 13.8$ GHz and a frequency bandwidth of between 10% and 15% can be estimated from Figure 3.2, with $\epsilon_r = 2.94$.

A square patch measuring 5.5 mm×5.5 mm is found to be resonant around $f =$ 13.8 GHz on the above substrate. Note that the smallest element spacing in the Ku band is 8.5 mm, hence there is enough room between adjacent patches.

There are various methods for feeding microstrip antennas: the coaxial-probe feed; the inset feed via microstrip line; the proximity-coupled feed; and the slot-coupled feed [61]. Among those, the in-plane microstrip line feed requires the minimum number of metalization layers and hence is simpler to fabricate. But due to the exposure of feed lines to the free space, they can contribute to spurious radiation and and deteriorate polarization purity. Other methods, on the other hand, use feed lines on an extra layer underneath the ground plane. The ground plane effectively shields the feed lines from the free space and reduces spurious radiation [68]. However, fabrication is a bit more difficult due to the addition of an extra metalization layer and requirement for accurate alignment between layers. In this work, we use probe feeds since they are simple to design, occupy minimum space, and do not degrade polarization purity significantly.

Figure 3.3(a) and (b) show the structure of the patch element. It is modeled with *periodic boundary conditions* (PBC) on side faces of the air-box. The PBCs impose equal electromagnetic field magnitudes and phases on the side faces perpendicular to $\hat{y}$, because there is no scan in this direction. On the side faces perpendicular to $\hat{x}$, the PBCs dictate equal electromagnetic field magnitudes and a phase difference of -252.7° at the center frequency $f = 13.8$ GHz.

There are two input ports: one for E polarization, and the other one for H polarization. These are coaxial ports which are connected to the probes feeding the patch. Figure 3.3(c) shows the real part and imaginary part of the input impedance

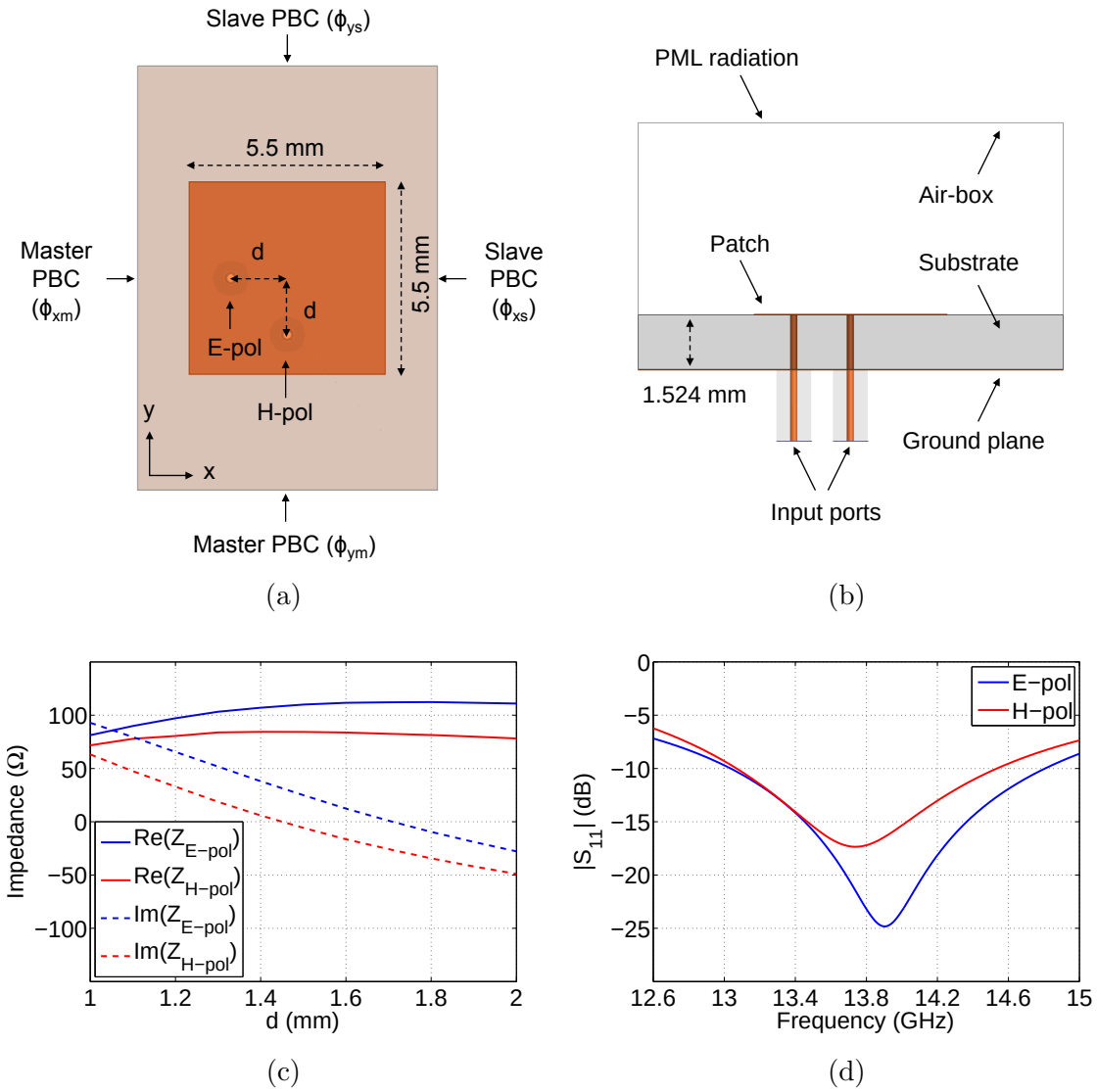

Figure 3.3: The patch element. (a) Top view. $\phi_{xs} - \phi_{xm} = -252.7°$ and $\phi_{ys} - \phi_{ym} = 0°$. (b) Side view. (c) Real and imaginary parts of input impedances as a function of d. (d) Frequency response for $d = 1.6$ mm, with the input impedances normalized to 100 Ω.

for both E-pol and H-pol ports. They are plotted as a function of the probe-feed location d with respect to the center of the patch. It is interesting to note that, although the patch is square and the probe-feed locations are equal in both axes, the input impedances of the two ports are different. This is due to the fact that the PBCs are simulating beam scanning only in the $\hat{x}$-direction, not in the $\hat{y}$-direction. In

other words, since the beam is tilted only in one direction, mutual coupling between elements in different directions are different, and consequently, the input impedances seen by the two ports are different. For polarization purity reasons, instead of using two different d values for two feeding probes, we preferred to keep everything symmetric. A feeding probe that is displaced 1.6 mm from the center of the patch gives an approximately real input impedance of 100 Ω at both ports.

Figure 3.3(d) shows the frequency response of the patch at the input ports. The antenna element is resonant around the center frequency $f = 13.8$ GHz, and the simulated frequency bandwidth in is more than 10% for 10-dB return loss, which is quite enough for this work.

Figure 3.1(c) shows the layer 1 of the Ku-subarray PCB containing nine patch elements.

3.2 1:3 Series Feed Network

A stripline combline feed with an appropriate characteristic impedance for each segment was designed on layer 3. The combline feed was designed to excite three patches with uniform excitations in magnitude and linear phase delay between successive patches. There are six feed lines: three of them are responsible for the E-polarized excitations of the nine patches, and the other three feeds excite the patches for H-polarized radiations. As shown in Figure 3.1(e), each of the six combline feeds is excited by a coaxial via at left. The other end of these vias are connected to the output ports of the parallel power dividers on layers 5 or 7, depending on the polarization.

In the combline feeds, we use T-junction power dividers to control power division ratios and delay lines to control phase shifts. The T-junction is a simple lossless three-port network. Figure 3.4 shows the transmission model of a T-junction. We

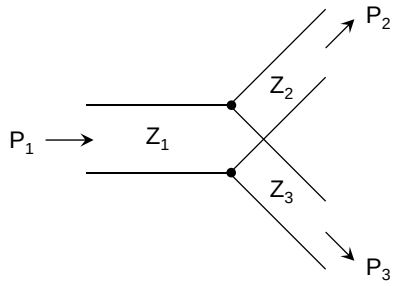

Figure 3.4: Transmission line model of a lossless T-junction used as a power divider.

can choose Z_2 and Z_3 so that the input port 1 is matched and the desired power split is obtained. For the power splitting ratios:

$$P_2 = \alpha P_1$$

$$P_3 = (1 - \alpha) P_1$$

we require [69]

$$\frac{Z_3}{Z_2} = \frac{\alpha}{1-\alpha}, \tag{3.1}$$

$$\frac{1}{Z_1} = \frac{1}{Z_2} + \frac{1}{Z_3}. \tag{3.2}$$

For example, if we want to split the input power so that $P_2 = P_1/3$ and $P_3 = 2P_1/3$, then $Z_2 = 2Z_3$.

The lossless T-junction divider is not matched at all ports and, in addition, does not have an isolation between output ports [70]. Other types of power divider such as the popular Wilkinson divider incorporate resistive loads to improve the match. However, realization of resistors in stripline fabrication process increases the manufacturing complexity and risk significantly. Therefore, many microstrip patch arrays use the simple split-line power divider, or T-junction [60].

For the series feed network inside Ku-subarray, consider Figure 3.5. There are two T-junction power dividers and two delay-lines. The T-junctions split the input power

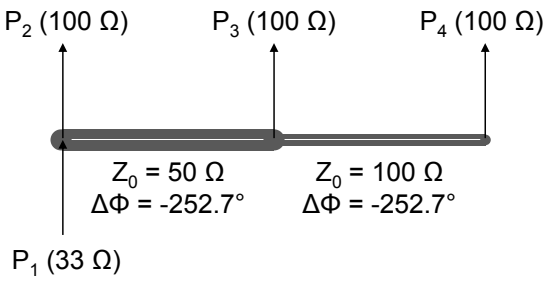

Figure 3.5: Structure of the series feed network inside Ku-subarray. Phase shifts are calculated for the center frequency $f = 13.8$ GHz.

equally between output ports 2, 3 and 4. Assume that the input impedance of the patches at the resonant frequency are 100 Ω. Using (3.1) and (3.2), for equal power distribution, the characteristic impedance of the first and second delay-lines should be 50 Ω and 100 Ω, respectively. In this case, the port impedance of the input port is 33 Ω.

The required phase difference between two successive output ports is $-252.7°$ at the center frequency $f = 13.8$ GHz. This value is calculated by noting that $k_g s$ and kd in (2.3) are the phase differences between adjacent patches in the feed-line and air, respectively. Thus, using (2.3), (2.10) and $k_{Ku} = 360°/\lambda_{Ku}$, we yield $\Delta\Phi_{Ku} = k_g s = \gamma_{Ku} \times k_{Ku} d_{xKu} = 1.8 \times 0.39 \times -360° = -252.7°$. These phase differences can be adjusted by optimizing the lengths of the delay-line segments connecting neighboring patches.

3.2.1 Test Board

For preliminary test purposes, a test circuit is designed and fabricated in six layers, as shown in Figure 3.6. The stack-up is shown in Appendix A. It is important to note that simple measurement techniques require a 50 Ω port impedance at all circuit terminals. This requirement can be met by using tapered-line impedance matching transformers at the ports with impedances other than 50 Ω. The configuration and function of each layer is described as follows:

1. *Layer 1:* The 100 Ω output impedances are converted to 50 Ω using three 100-to-50 Ω tapered-line impedance matching transformers. There are three microstrip-to-coplanar waveguide with ground (MS-CPWG) transitions at the outputs for mounting end-launch SMA connectors.

2. *Layer 2:* Ground plane

3. *Layer 3:* This is a stripline layer that contains the 1:3 series feed network and a 33-to-50 Ω impedance matching transformer.

4. *Layer 4:* Ground plane

5. *Layer 5:* Empty layer

6. *Layer 6:* Ground plane. Input port is accessible on this layer using a panel-mount SMA connector. A plated via is located between this layer and layer 3 and transfers the input signal to the series feed network.

The measured magnitude and phase responses of the 1:3 series feed network are shown in Figures 3.6(c) and 3.6(d). The ideal IL performance will correspond to an equal power transmitted to all three ports. The S-parameters in Figure 3.6(c) show that there is approximately a 2.5-dB variation to the power each output port receives, which is partially due to the addition of the non-ideal impedance matching transformers and also imperfect connector attachments. The phase differences between successive output ports are close to the target value of $-252.7°$ at the center frequency $f = 13.8$ GHz.

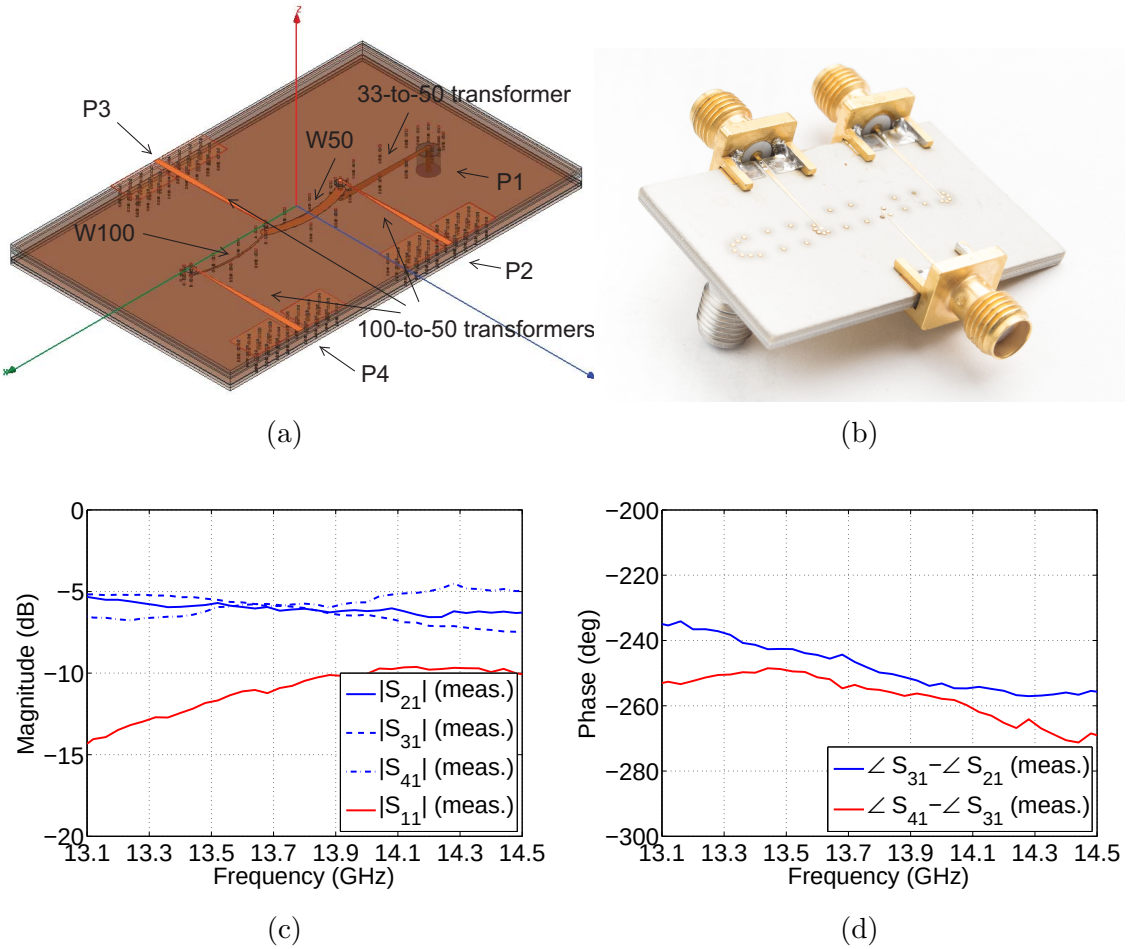

Figure 3.6: Test board for the Ku-subarray series feed network. (a) HFSS model. $W_{50} = 0.85$ mm, $W_{100} = 0.15$ mm. (b) Fabricated. (c) The magnitude of measured S-parameters. (d) The phase of measured S-parameters.

3.3 1:3 Parallel Power Divider

There are two 1:3 parallel power dividers in a Ku subarray: one for the E-polarization on layer 5 and the other one for the H-polarization on layer 7, as shown in Figures 3.1(g) and 3.1(i), respectively. Each of these power splitters is excited by a coaxial via. The other end of these vias are on layer 8 and they are the inputs of the Ku-subarray. These inputs will be fed by two glass beads. The glass beads link the Ku-subarray to the SSL directional couplers of the subaperture which couple the power off the series feed SSL.

Many power divider circuits have been studied in the literature. In planar configurations, two particular circuit types are often used: the symmetric geometry with radially oriented lines [71–73] and the Wilkinson-type geometry [74, 75].

An equal split Wilkinson power divider is shown in Figure 3.7(a). In general, it can be made to give arbitrary power division. The Wilkinson-type power dividers benefit from high isolation between output ports. But they require resistors between them which is very challenging and costly for fabrication in the SL configuration.

Radial power dividers, as shown in Figure 3.7(b), use a circular microstrip center-fed disk structure. At the center of the disk is a coaxially fed port which is the input port. The other N ports are microstrip line ports symmetrically located around the circumference of the circular disk. Due to their geometrical symmetry, these power dividers do not exhibit any imbalance in either the amplitude or the phase of the output signals at any frequency [76]. This property makes them very attractive in many RF applications. But a circular disk geometry with output lines extending radially in all directions is not appropriate for the purpose of this work, where radiating elements are placed on a rectangular grid.

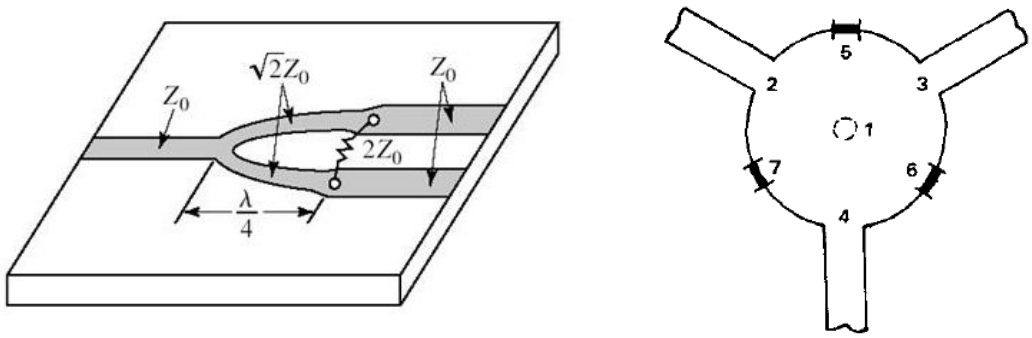

(a) (b)

Figure 3.7: Two types of planar power dividers commonly used in literature. (a) An equal-split Wilkinson power divider [70]. (b) A center-fed microstrip disk three-way power divider [76].

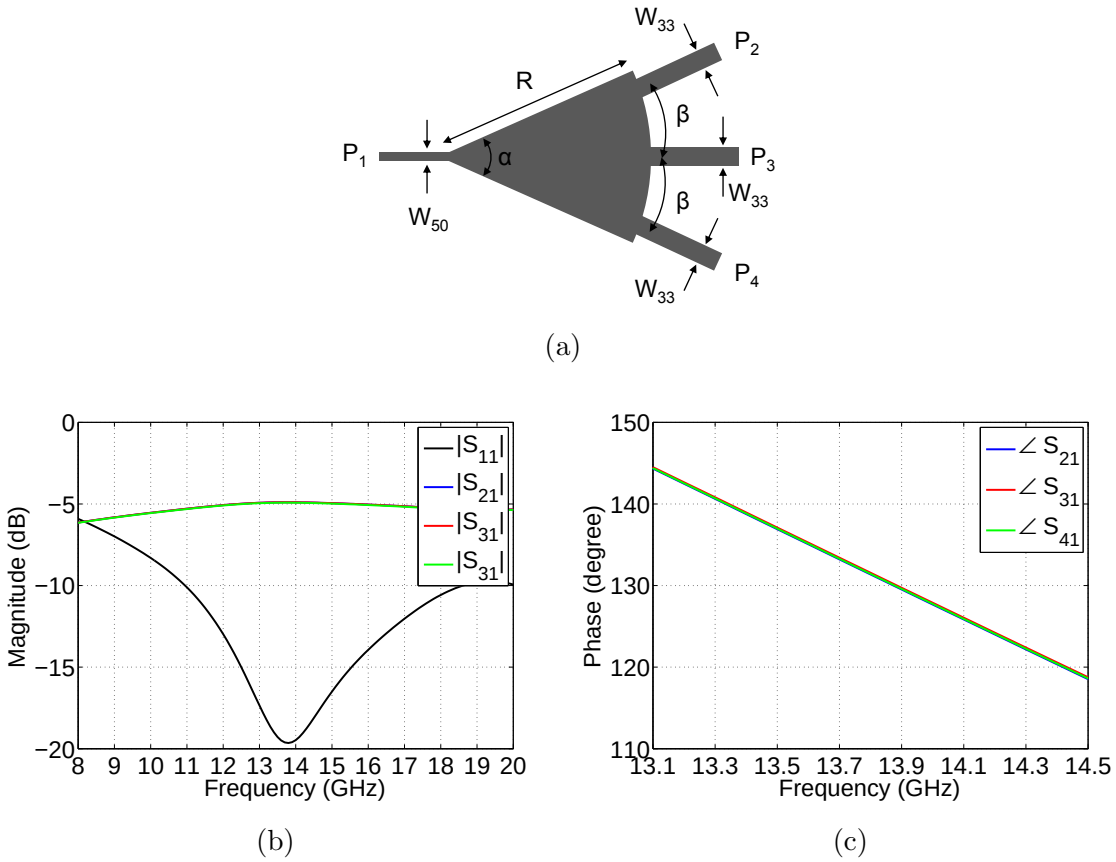

Figure 3.8: The sectorial 1:3 power divider circuit. (a) Geometry. $W_{50} = 0.3$ mm, $W_{33} = 0.6$ mm, $R = 8.5$ mm, $\alpha = 20°$, $\beta = 7.5°$. (b) Magnitude of the simulated S-parameters. (b) Phase of the simulated S-parameters.

Another possible geometry, with almost linearly aligned output ports, is the sectorial power divider circuit shown in Figure 3.8(a). This power divider consists of a taper of the stripline width in the form of a circular sector with three output ports along the arc. In this work, we used this power divider for two reasons: first, it does not require isolation resistors which make the fabrication process risky and costly; second, the output ports can be linearly aligned.

A comprehensive theoretical analysis of this geometry is carried out in [76] and some design charts are available in [77]. The power level at the output ports can be controlled by adjusting the locations and/or widths of the planar lines connected to

these ports. This work requires equal amplitudes and phases at the output ports of the 1:3 parallel power divider. Thus, the location of the output lines are symmetric and their widths are equal. The characteristic impedances of the output ports are chosen to be 33 Ω, to match the input impedances of the series feed networks of the Ku-subarray. The characteristic impedance of the input port is 50 Ω and matches the impedance of the glass bead. The radius of the sector R controls the center frequency of operation. The sector angle α, and the angle β between the output ports control the RL, IL and bandwidth. The dimensions of the power divider have been parametrically optimized in simulation for best operation around 13.8 GHz.

The simulated S-parameters of the divider are shown in Figures 3.8(b) and 3.8(c). In simulation, the circuit shown in Figure 3.8(a) is sandwiched between two Rogers RT/duroid 6202 substrates with 0.524 mm thicknesses and ground planes on outer surfaces. The ILs from port 1 to the three output ports are identical at 4.9 dB which are very close to the ideal lossless IL of $10\log_{10}3 = 4.77$ dB. The input RL is high at 19.5 dB at 13.8 GHz. A 10-dB frequency bandwidth of 55% is achieved in simulation which is much wider than the required 10% bandwidth. The output phases are identical, as desired.

3.3.1 Test Board

As discussed in the previous section, for preliminary test purposes, a test circuit is designed and fabricated in six layers, with the same stack up (see Appendix A). The HFSS model and the photograph of the fabricated board are shown in Figures 3.9(a) and 3.9(b), respectively. The configuration and function of each layer is described as follows:

1. *Layer 1:* Empty layer
2. *Layer 2:* Ground plane
3. *Layer 3:* Empty layer

4. *Layer 4:* Ground plane

5. *Layer 5:* This is a stripline layer that contains the 1:3 parallel power divider with 50 Ω input and 33 Ω output impedances. The 33 Ω output impedances are converted to 50 Ω using three 33-to-50 Ω tapered-line impedance matching transformers.

6. *Layer 6:* Ground plane. Input and output ports are accessible on this layer using four panel-mount SMA connectors. Four plated vias are located between this layer and layer 5 and transfer the signal to the power divider.

The SMA connector and its glass bead are shown in Figures 3.9(c) and 3.9(d), respectively. The connectors are attached to the board using MG Chemicals 8331S silver epoxy. The PCB fabrication house had plugged (filled) the input/output vias with a non-conductive material and there was no safe way to drill them post-fabrication. Thus, we were unable to use the glass bead. Instead, we soldered a small amount of solder on the vias and filled the female sockets in the center of the connectors with silver epoxy before mounting the connectors on the board.

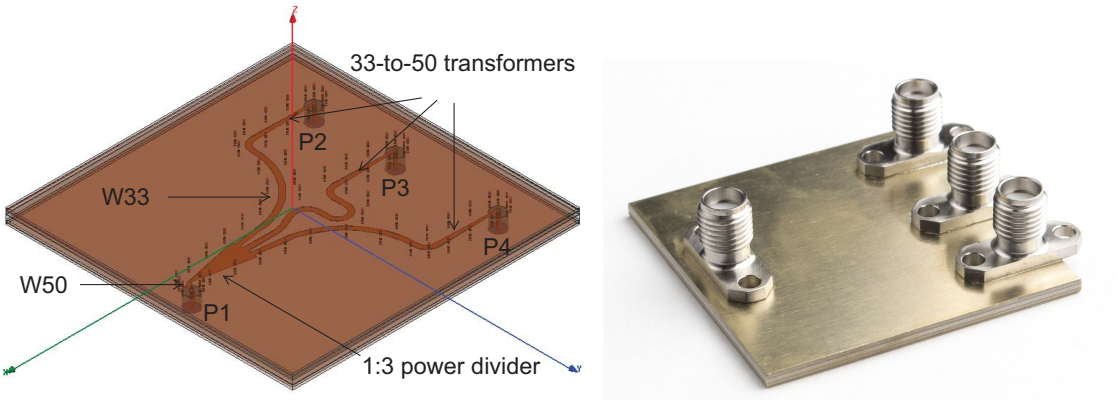

(a) (b)

Figure 3.9: Test board for the 1:3 parallel power divider of the Ku-subarray. (a) HFSS model. (b) Fabricated.

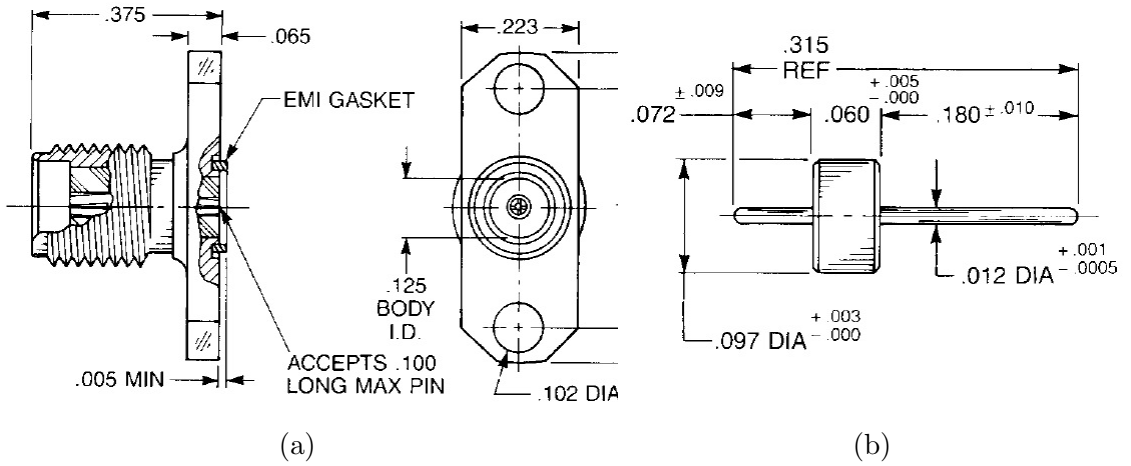

Figure 3.10: The panel-mount SMA connector and its glass bead. All dimensions are in inches. (a) AEP 9144-9513-000. (b) AEP 920-55.

The measured magnitude and phase responses of the 1:3 series feed network are shown in Figure 3.11. TRL calibration is performed to remove the effect of SMA connectors. This calibration method and its standards are discussed in Appendix C.

The ideal performance will correspond to equal power and phases at all three ports. Preliminary measurement results revealed that the frequency response—especially the phase response—is highly sensitive to the quality of connector attachments and differs from one port to another. To depict this issue, we have assembled and tested two power divider test boards. The magnitude and phase responses of the board I are shown in Figures 3.11(a) and 3.11(b). A maximum phase difference of 15° is observed between ports 3 and 4 at 14.3 GHz. Figures 3.11(c) and 3.11(d) show the frequency response of the board II at the first attempt. In this case, a maximum phase difference of 5° is observed between ports 2 and 3 at 14.1 GHz. In the next attempt, some more silver epoxy was added to the side walls of the connector on port 2 to mechanically strengthen the connection, but the frequency response deteriorated, as seen in Figures 3.11(e) and 3.11(f). In this case, a maximum phase difference of 10° is observed between ports 2 and 3 at 14.2 GHz.

TRL calibration requires similar connector attachment qualities for all of the connections to achieve the best results. Here, this requirement was not met, due to the inability of using glass beads.

However, the measured ILs and RLs are more promising than the phase responses. The ideal IL of a lossless 1:3 power divider is 4.77 dB. But the ILs shown in Figures 3.11(a), 3.11(c) and 3.11(e) are as low as 3.8 dB at some frequency points. This is due to the fact that the length of the thru standard in the TRL calibration kit is not zero. The measured IL of the thru standard with nonzero length is 1 dB to 1.5 dB in the frequency band, which should be added to the measured ILs in Figure 3.11. Hence, the range of ILs of the fabricated power divider after removing the effect of the lines connected to the ports is expected to be in the 4.8–5.3 dB range.

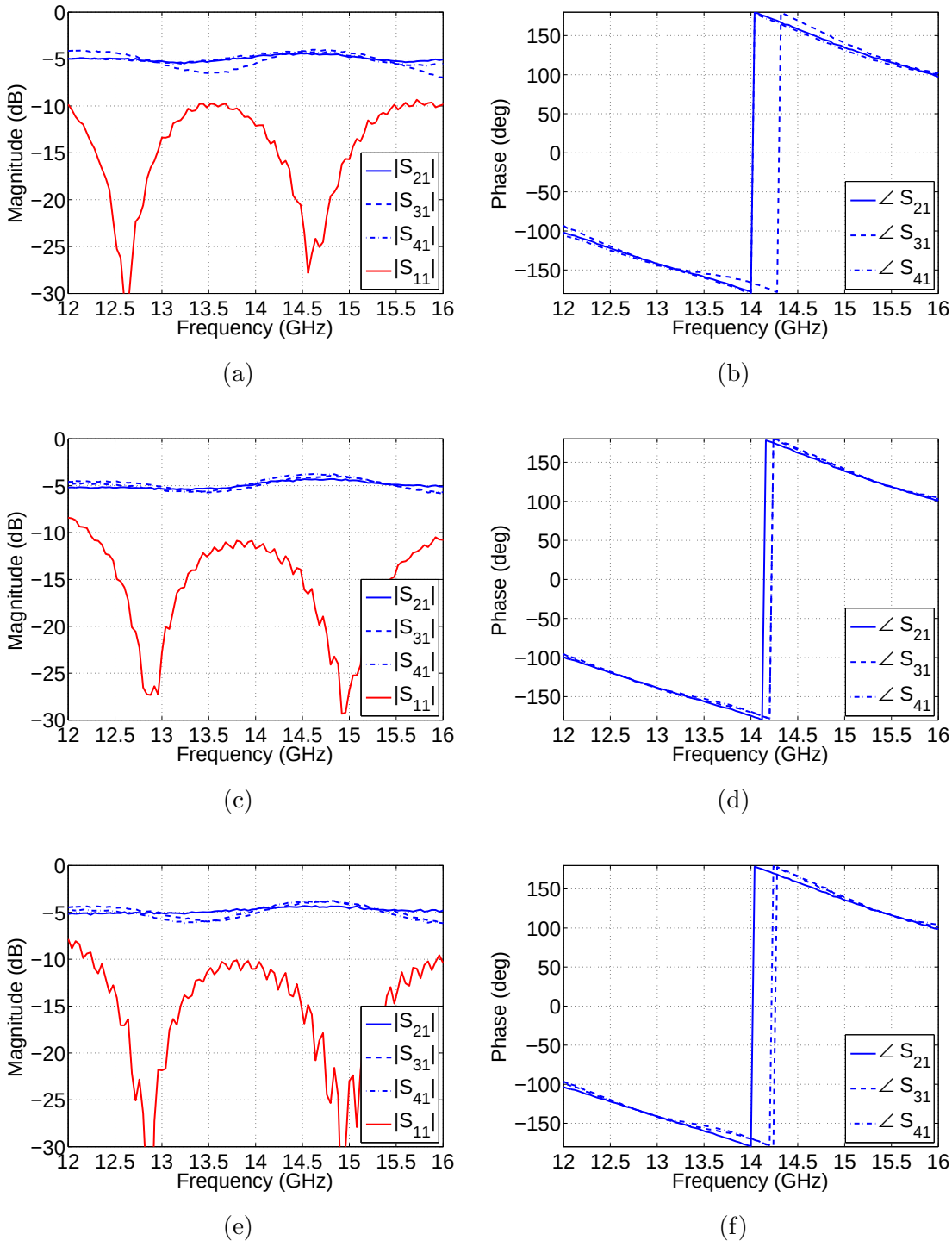

Figure 3.11: Measured responses of the 1:3 parallel power divider test board. The network analyzer is calibrated using TRL method, as discussed in Appendix C (a) Magnitude (board I). (b) Phase (board I). (c) Magnitude (board II, attempt I). (d) Phase (board II, attempt I). (e) Magnitude (board II, attempt II). (f) Phase (board II, attempt II).

3.4 Standalone Performance

The 3×3 Ku-subarray shown in Figure 3.12 has been designed and simulated using Ansys HFSS to test the dual-polarized radiation capability. Top and side faces of the air-box are modeled as *perfectly matched layers* (PML). A PML is an artificial absorbing layer, commonly used to truncate computational regions to simulate wave propagation problems exposed to free-space. The key property of a PML is that waves incident upon it do not reflect at the interface. This property allows the PML to strongly absorb outgoing waves from the interior of a computational region without reflecting them back into the interior. In this work, PML is preferred to radiation boundary condition, because it functions significantly better for incident angles up to 70° [78].

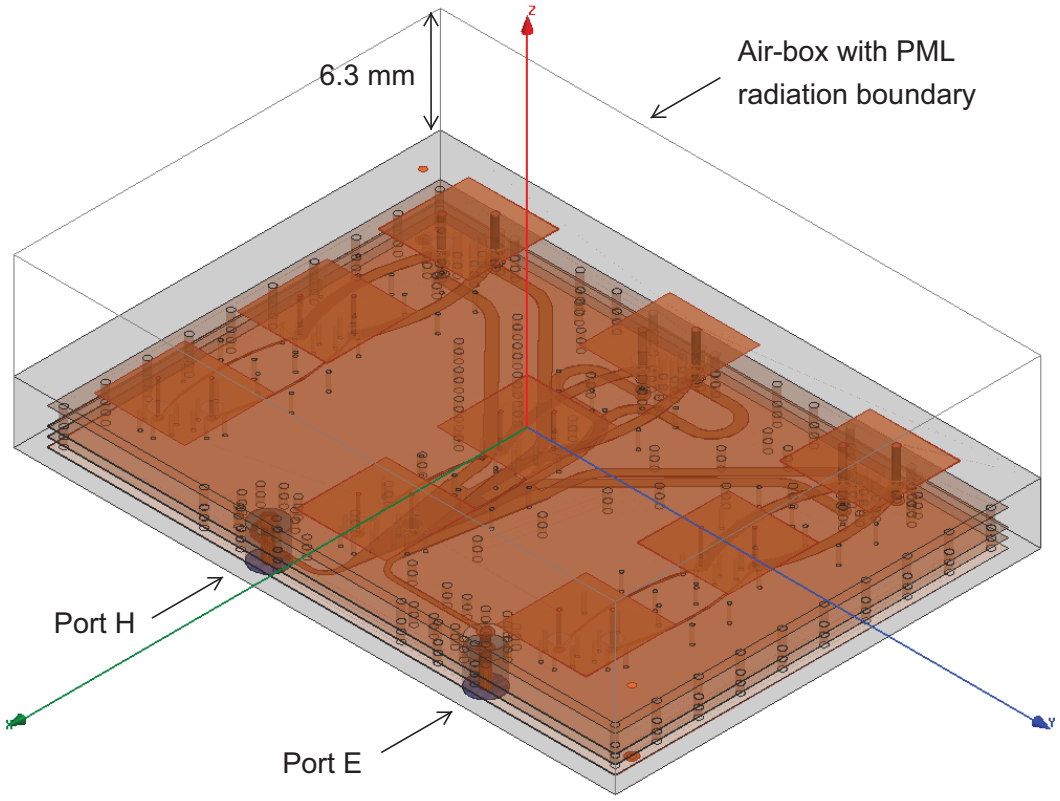

Figure 3.12: Ansys HFSS model of the Ku-subarray.

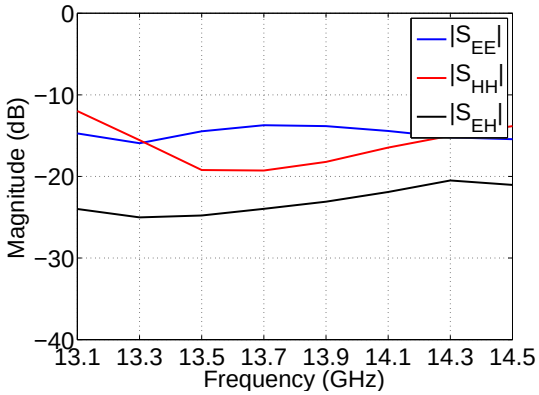

Figure 3.13: Simulated S-parameters of of the Ku-subarray.

Figure 3.13 plots the return losses and the isolation between the input ports of the Ku-subarray as a function of frequency. The return losses are better than 12 dB at all frequencies for both polarizations. Also, more than 20 dB isolation is expected between the E-pol and H-pol ports.

Figure 3.14 plots the radiation patterns of the subarray in both planes for both polarizations. The $x - z$ plane is defined as the *scan plane*. Similarly, the $y - z$ plane is defined as the *orthogonal plane*. Maximum co-polarized gains of 11.9 dBi and 12.4 dBi are estimated for the E-pol and H-pol excitations, respectively. The cross-polarized gains are less than -5 dBi and -7 dBi in the main-beam region, for the E- and H-polarized radiations, respectively. The main-beam region is defined as $-60^\circ < \theta < -40^\circ$ on the scan plane.

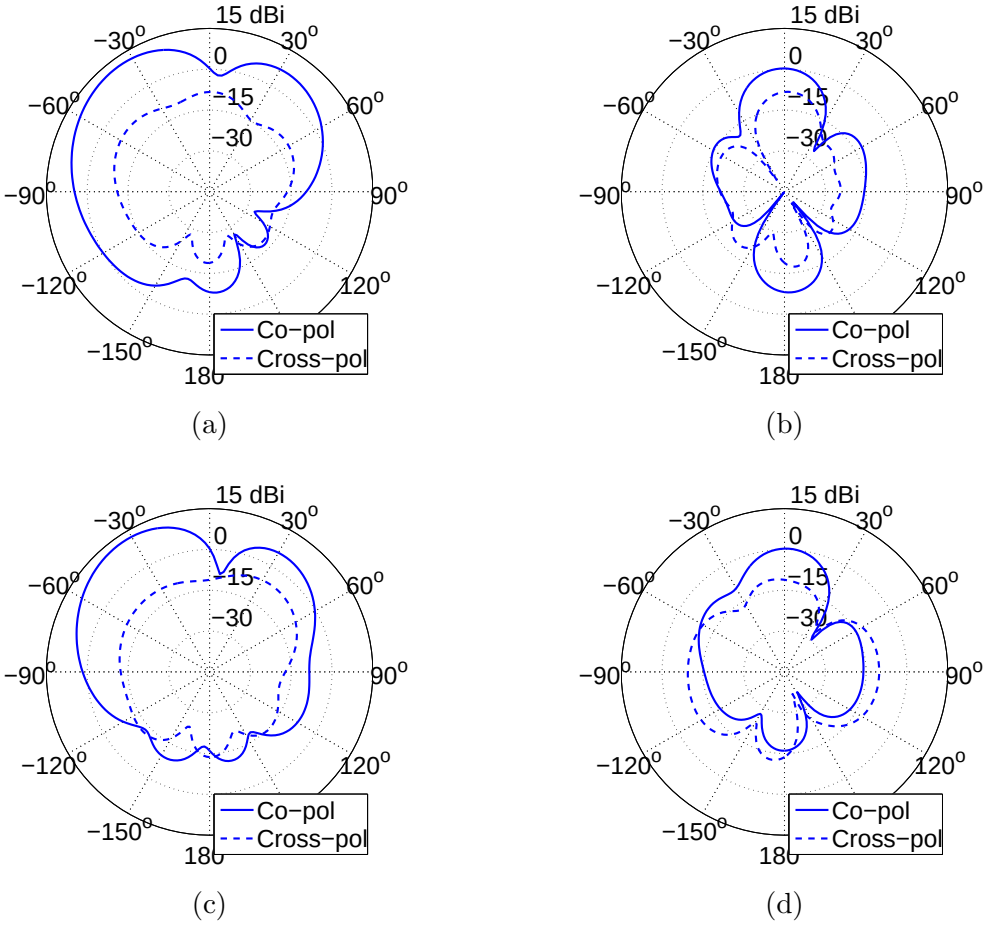

Figure 3.14: Simulated co-polarized and cross-polarized radiation gains of the Ku-subarray as a function of θ. (a) Scan plane ($x-z$) for E-pol excitation. (b) Orthogonal plane ($y-z$) for E-pol excitation. (c) Scan plane for H-pol excitation. (d) Orthogonal plane for H-pol excitation.

3.5 Infinite Array Performance

To evaluate the performance of the Ku-subarray in an infinite array environment, we have re-simulated the model in Figure 3.12 with PBCs on side faces and PML on top face of the air-box. The PBCs impose equal electromagnetic field magnitudes and phases on the side faces perpendicular to $\hat{y}$, because there is no scan in this direction. On the side faces perpendicular to $\hat{x}$, the PBCs dictate equal electromagnetic field magnitudes and a phase difference of $3 \times -252.7^\circ \approx -758^\circ$ at the center frequency $f = 13.8$ GHz.

The input reflection coefficients and the isolation between the input ports of the Ku-subarray with PBCs are shown in Figure 3.15 as a function of frequency, for both polarizations. The return losses are better than 10 dB at all frequencies for both polarizations. Also, the minimum isolation between E-pol and H-pol ports is expected to be around 23 dB. This implies that the cross-polarized fields caused by the coupling between the ports in a uniform arrangement of the individual Ku-subarrays could be as high as -23 dB. Therefore, some cross-polarization suppression techniques need to be applied.

Figure 3.16 plots the radiation patterns of the subarray in both planes for both polarizations, with taking the mutual coupling effects into account. Maximum co-

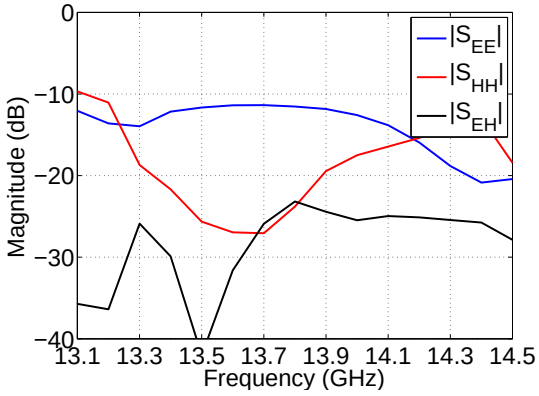

Figure 3.15: Simulated S-parameters of of the Ku-subarray with PBCs.

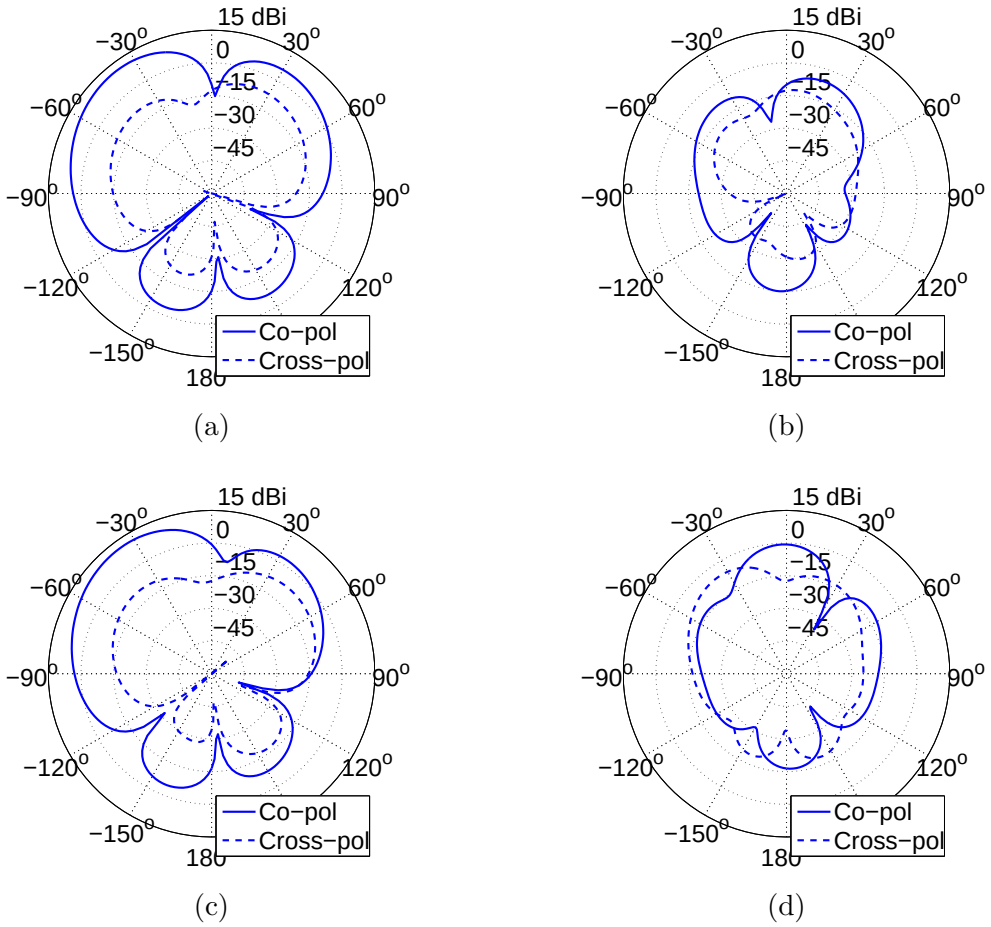

Figure 3.16: Simulated co-polarized and cross-polarized radiation gains of the Ku-subarray with PBCs as a function of θ. (a) Scan plane ($x-z$) for E-pol excitation. (b) Orthogonal plane ($y-z$) for E-pol excitation. (c) Scan plane for H-pol excitation. (d) Orthogonal plane for H-pol excitation.

polarized gains of 11.3 dBi and 11.4 dBi are estimated for the E-pol and H-pol excitations, respectively. The maximum cross-polarization levels are about -20 dB in the main-beam region ($-60° < \theta < -40°$ on the scan plane).

3.6 Measurement Results

The smallest measurable unit in the Ku band is the Ku-subarray which consists of 3×3 patch antennas and their feeding networks. A Ku-subarray on a finite ground plane with dummy slots is fabricated and its radiation properties and S-parameters are

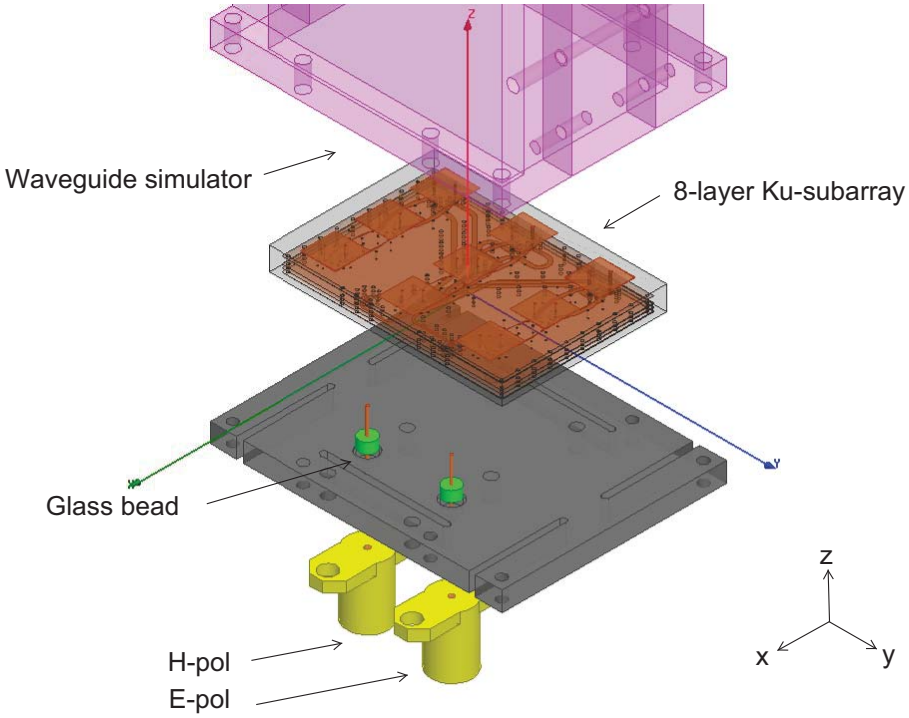

Figure 3.17: Exploded view of the Ku-subarray, the feeding mechanism and the waveguide simulator.

measured. Dummy slots are not excited and merely enforce the boundary conditions which may exist in the full array.

The fabricated parts are shown in Figure 3.17. There are two excitation ports: one for E-polarization and the other one of H-polarization. The input ports are SMA connectors which are connected to the input ports of the 8-layer PCB via glass beads.

For active impedance measurements, a waveguide simulator will be used. This enables us to measure the impedance of the Ku-subarray as if it is in an infinite array of like elements. Appendix D discusses the theory and design procedure of waveguide simulators. The other end of the waveguide simulator is terminated with an RF absorber.

3.6.1 In Free-space

In order to measure the radiation patterns and the standalone S-parameters of the Ku-subarray, the waveguide simulator of Figure 3.17 is removed. Figure 3.18 shows the photograph of the antenna under test (AUT). The Network Analyzer is calibrated using custom Short-Open-Load (SOL) calibration standards. The calibration planes are put on the mating plane of the 8-layer PCB and the aluminum plate.

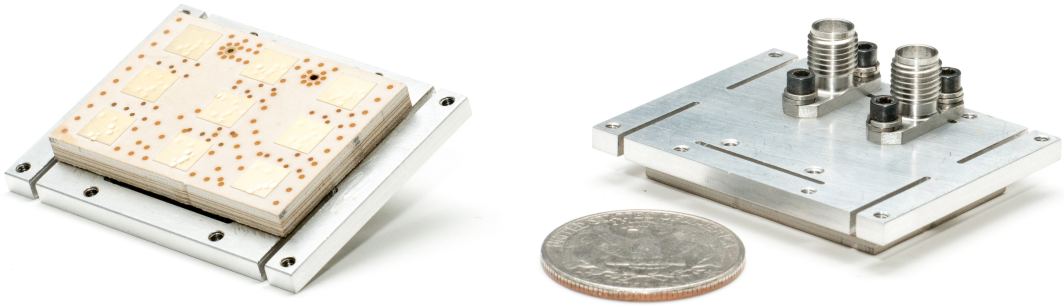

(a) (b)

Figure 3.18: Photograph of the Ku-subarray PCB mounted on an aluminum plate. (a) Top side. (b) Bottom side.

Figure 3.19 shows the simulated and measured S-parameters of the Ku-subarray for both polarizations. The antenna radiates into free-space. The return loss is better than 9 dB in the frequency band of 13.1—14.5 GHz.

Figure 3.20 shows the measurement setup in the antenna chamber. Only the AUT is shown in this photo which is set up as the receiver. A standard gain horn antenna is used as the transmitter on the other side of the chamber. The radiation patterns of the Ku-subarray on the scan plane ($x - z$) are shown in Figure 3.21. Each graph plots both co-polarized and cross-polarized gains. The start (13.1 GHz), mid-band (13.8 GHz) and stop (14.5 GHz) frequencies are simulated and measured, for both polarizations.

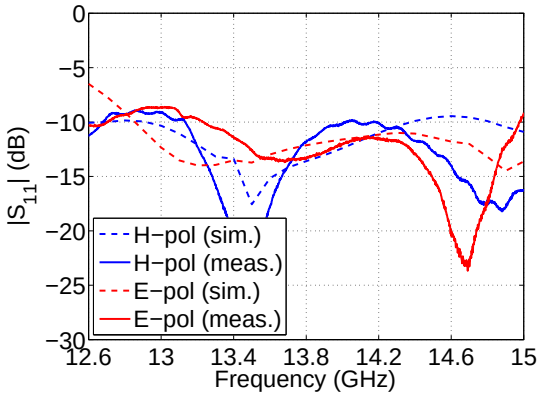

Figure 3.19: Simulated and measured S-parameters of the Ku-subarray radiating into free-space.

The measured and simulated patterns agree reasonably well. In the desired range of scan angles ($-60^\circ < \theta < -40^\circ$), the measured cross-polarization levels are better than -20 dB for the lower frequencies. In the higher frequencies, however, the cross-polarization levels increase to about -15 dB. A feeding scheme that can effectively improve cross-polarization levels will be discussed in Section 3.7.

Figure 3.20: Photograph of the Ku-subarray in the far-field chamber.

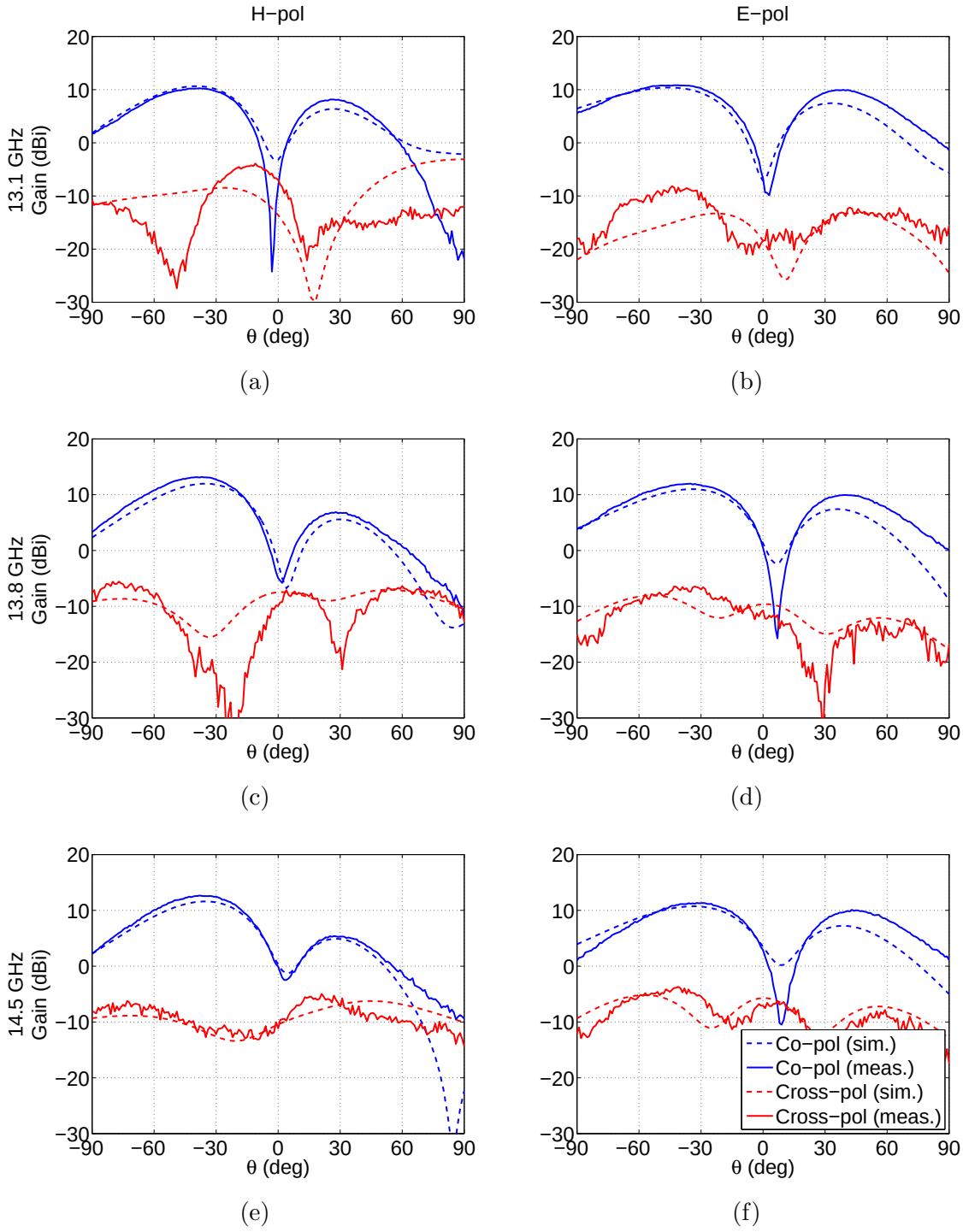

Figure 3.21: Co-pol and cross-pol realized gains of the Ku-subarray on the scan plane $(x-z)$. All graphs have the same legend. (a) H-pol at 13.1 GHz. (b) E-pol at 13.1 GHz. (c) H-pol at 13.8 GHz. (d) E-pol at 13.8 GHz. (e) H-pol at 14.5 GHz. (f) E-pol at 14.5 GHz.

3.6.2 Inside Waveguide

In order to measure the active impedance of the Ku-subarray, a waveguide simulator is used. The measurement setup is shown in Figure 3.22. The Ku-subarray is inserted into one side of the waveguide and an RF absorber is inserted into the other side.

As discussed in Appendix D, in this work, it is only practical to measure the active impedance of the H-pol port. Figure 3.23 shows the measurement and simulation results. According to Figure D.5(b), in this design, the frequency of interest is 13.1 GHz where both waveguide simulator and the array have the same scan angle. At 13.1 GHz, the simulation and measurement results agree very well and the input VSWR is less than 2, which demonstrates a great impedance match, even with mutual coupling.

(a) (b)

Figure 3.22: Photograph of the Ku-subarray inside waveguide simulator. (a) Front side. (b) Back side.

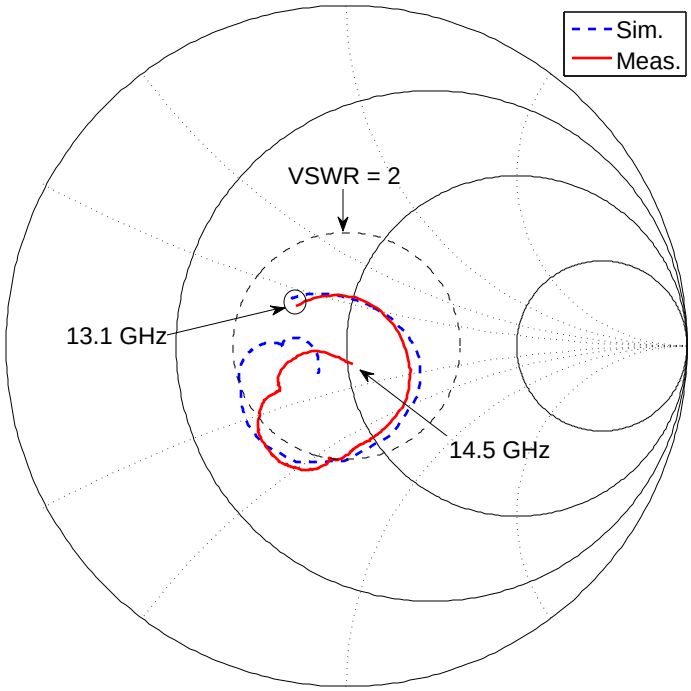

Figure 3.23: Smith chart plot of simulated and measured active impedance loci for the H-pol port of the Ku-subarray.

3.7 Improvement of Cross-polarization Levels

An array constructed of identically oriented and fed dual polarization antenna elements has the same cross-polarization level as the individual elements [39]. Hence, without employing any cross-polarization suppression technique, the cross-polarization level of the Ku-array would not be better than that of the Ku-subarray, i.e. -15 dB in the higher frequencies of the Ku-band.

This level can be significantly improved by using mirrored feed technique as shown in Figure 3.24(b) [40]. Consider four Ku-subarrays in a 2×2 grid. Each Ku-subarray has two ports, one for E-polarization and another one for H-polarization.

In the conventional configuration (Figure 3.24(a)), the individual elements have the same orientation and there will be no cross-polarization suppression. On the other hand, the configuration of Figure 3.24(b) offers substantial cross-polarization

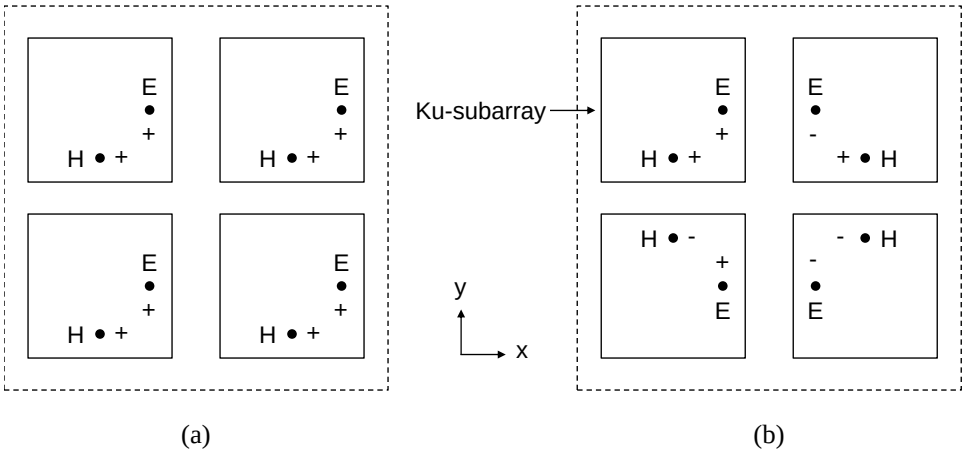

Figure 3.24: Conventional (a) and mirrored feed (b) arrangements for four Ku-subarrays.

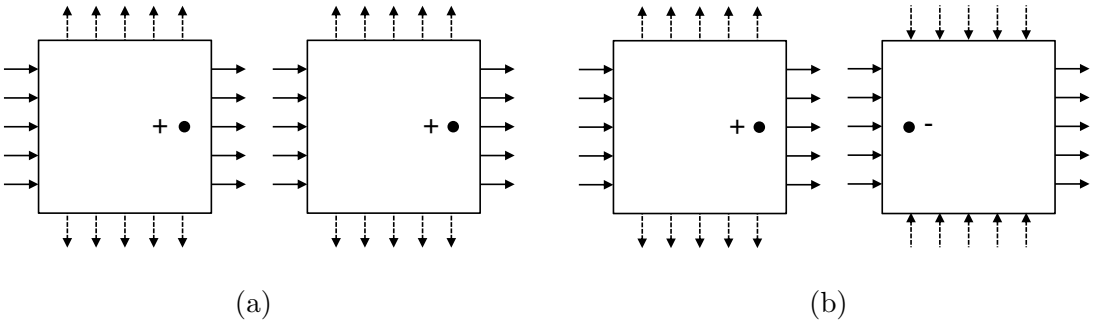

Figure 3.25: Co-polarized (solid lines) and cross-polarized (dashed lines) fields generated by antenna elements. (a) Conventional feed. (b) Mirrored feed.

improvements by mirroring some elements in the horizontal and/or in the vertical planes.

For each configuration, it is shown how a particular port should be fed to give all elements the same effective excitation. Ports marked "+" must be fed directly and ports marked "−" must be fed by 180° phase delay. This ensures that the co-polar fields for the elements add in phase toward the desired scan angle.

In order to study the principle of operation, we consider simple 1×2 arrays of antenna elements with single feeds. The co-polarized and cross-polarized fields gen-

erated by antenna elements are shown in Figure 3.25 [38]. The co-polarized fields are shown by solid lines in the horizontal direction. The cross-polarized fields are shown by dashed lines in the vertical direction.

For the conventional case, it is clear from Figure 3.25(a) that the cross-polarized fields cancel in the vertical plane, whereas in the horizontal plane they add in-phase. On the other hand, configuration of Figure 3.25(b) feeds pairs of antenna elements at the opposite ends and with a 180° phase shift. The cross-polarized fields now cancel in both vertical and horizontal planes. Note that co-polarized fields re-enforce in both cases.

CHAPTER 4

KU-BAND SUBAPERTURE

Each Ku-subaperture consists of six consecutive Ku-subarrays along the $\hat{x}$-direction. In this chapter, the feeding method used in a subaperture will be discussed. The architecture of the subaperture is shown in Figure 4.1. The input of a Ku-subaperture is a WR-62 waveguide. A waveguide-to-suspended stripline (WG-SSL) transition converts the transmission medium to SSL. SSL delay-lines and couplers split the power between the subarrays with appropriate magnitudes and phases.

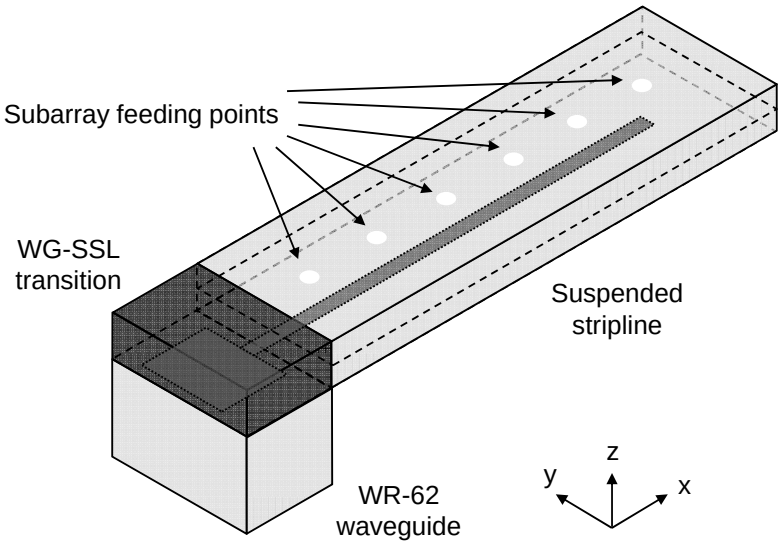

Figure 4.1: Architecture of the suaperture.

4.1 Waveguide-to-Suspended Stripline Transition

4.1.1 Introduction

Basic designs of waveguide-to-microstrip (WG-MS) transition employ an E-plane probe transition [79,80], in which a microstrip on a dielectric substrate is inserted into the waveguide from the broad-wall side (Figure 4.2(a)). The waveguide is extended to the other side of the probe and shorted at a quarter wavelength's distance, namely a back-short, to match the impedance and achieve good transmission properties.

For a broader bandwidth, the strip probe was replaced with a patch element in [81], which is shown in Figure 4.2(c). A back-short could put restrictions on package design and limit compactness.

The idea of slot-fed microstrip antennas (or resonators) was used in [82] to eliminate the back-short (Figure 4.2(b)). In this method, fields are coupled from the microstrip to a patch antenna element deposited on an additional substrate in the waveguide, via a slot in the ground plane. With this transition, the waveguide structure is placed on only one side of the microstrip circuit. However, due to an additional piece of substrate inside the waveguide, fabrication of this structure is still challenging.

An easier-to-fabricate approach is taken in two independent studies of single substrate WG-SSL transitions [83, 84], in which a radiating element is placed on the other side of the same substrate and is excited by proximity coupling. These designs use patch elements to reduce the size while achieving a low insertion loss and broad frequency bandwidth.

Here, we will focus on our design as reported in [84,85] with additional studies on the coupling structure and the design procedure. This design achieves a bandwidth that is 1.5 times broader than that in [83], while the electrical length of its back-short is three times shorter. The transition is fabricated and measured for validation.

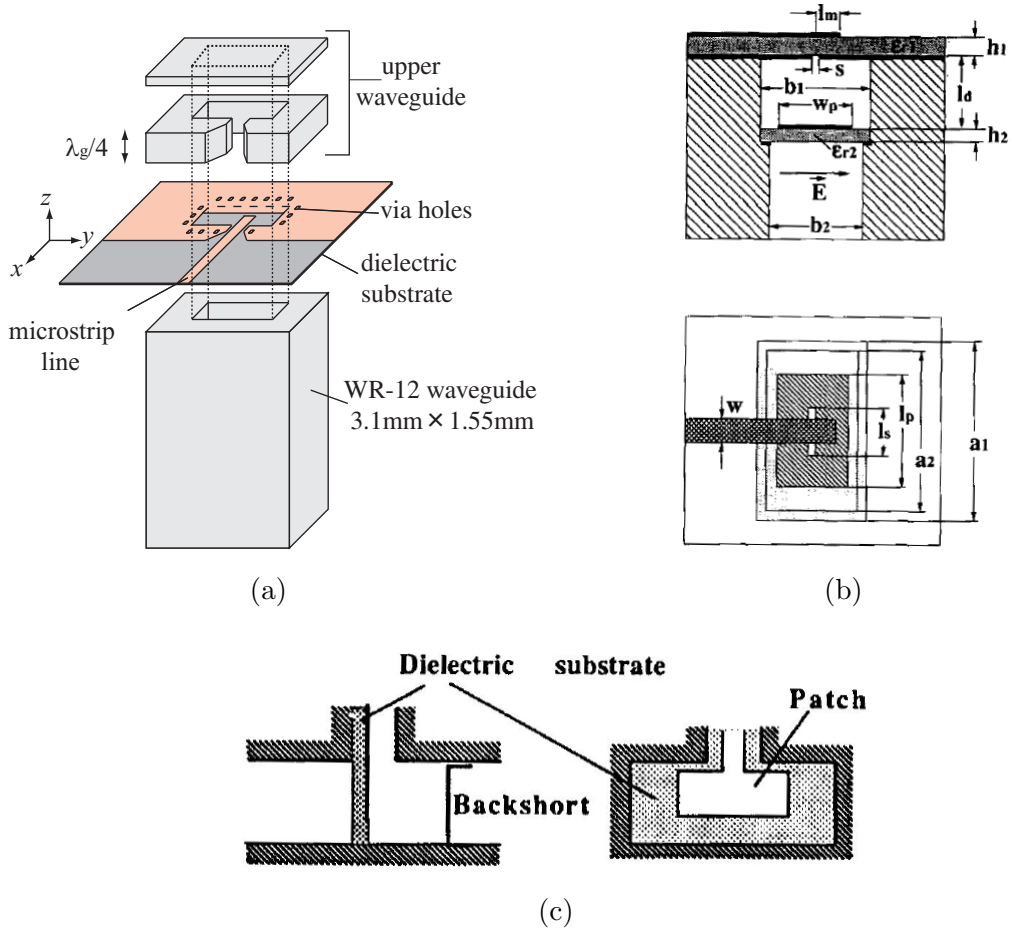

Figure 4.2: E-plane perpendicular WG-MS transitions in literature: (a) From [79], (b) From [82], (c) From [81].

4.1.2 Configuration

Figure 4.3 illustrates the proposed WG-SSL transition. The TEM transmission mode of the SSL is first converted to the TM_{01} resonant mode of the patch antenna as a matching element and then to the TE_{10} fundamental mode of the rectangular waveguide. The SSL directly connects to the first patch element on the same layer of the dielectric substrate and a parasitic patch element on the other side is excited via coupling.

The capacitive nature of proximity coupling is used to tune the antenna for impedance match over a broader bandwidth. A larger air separation between the

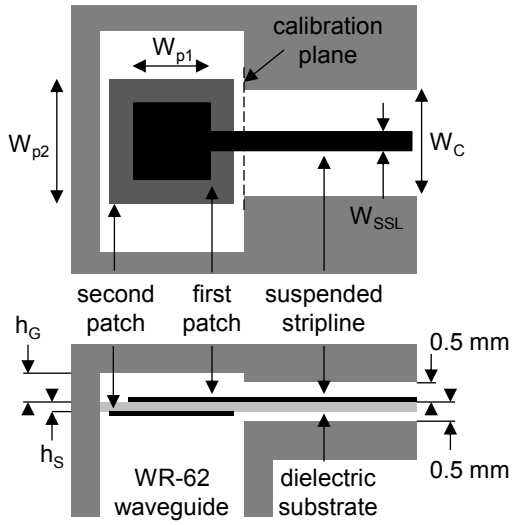

Figure 4.3: Top and side views of the geometry of the perpendicular WG-SSL transition. The physical dimensions for Ku-band are given by $W_{P1} = 5.2$ mm, $W_{P2} = 7.2$ mm, $h_G = 1$ mm, $h_S = 0.127$ mm, $W_{SSL} = 1.3$ mm, and $W_C = 5.8$ mm (patches are square).

patches and ground plane, h_G, allows fields to radiate into the waveguide over a broader bandwidth by weakening the bond of fields to the planar circuit. This height is limited by package design considerations. In this design, h_G is equal to 1 mm, which is only $\lambda_g/30$—a 86% reduction from a quarter wavelength—where λ_g is the guided wavelength in the waveguide at 13.8 GHz.

A Rogers RT/duroid 5880 substrate with a thickness of 0.127 mm, a dielectric constant of 2.2, and a loss tangent of 0.0009 is employed to realize a WG-SSL transition centered at 13.8 GHz. For a standard Ku-band WR-62 rectangular waveguide, the cross-sectional dimensions are 15.8 mm $\times$ 7.9 mm.

The transition design is simulated using Ansys HFSS. Figure 4.4 shows the electric field distribution on the substrate at 13.8 GHz. Excitation of the TM_{01} mode beneath the patch antenna can be observed.

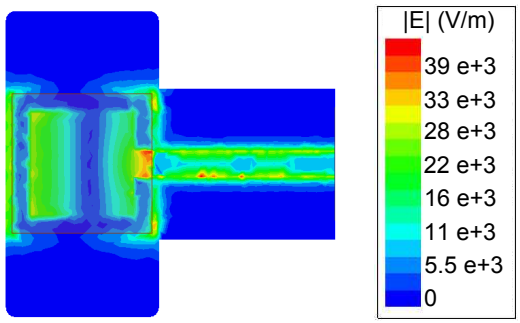

Figure 4.4: Electric field strength on the substrate at the center frequency, 13.8 GHz for an incident power of 1 W.

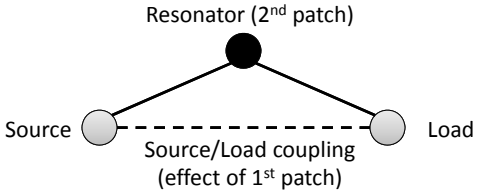

Figure 4.5: Coupling and routing scheme of the transition with two patch elements

4.1.3 Design Guidelines and Discussion

This kind of a transition having a resonator as a matching element is analogous to a single-pole coupled resonator bandpass filter with source-load cross-coupling, as shown in Figure 4.5. It has been shown that a resonating filter with n resonators could have up to n transmission zeros if the source and the load are cross-coupled [86]. The second patch is the main resonator in this system whose dimension, W_{P2}, determines the passband characteristics as shown in Figure 4.6(b). The first patch, on the other hand, plays the role of source-load cross-coupling and its dimension, W_{P1}, modifies the out-of-band response. Larger W_{P1} results in larger cross-coupling between source and load, resulting in a frequency shift of the transmission zero toward the center frequency [87], as can be seen in Figure 4.6(a).

To design this transition, one can estimate the dimensions of the second patch, W_{P2}, using

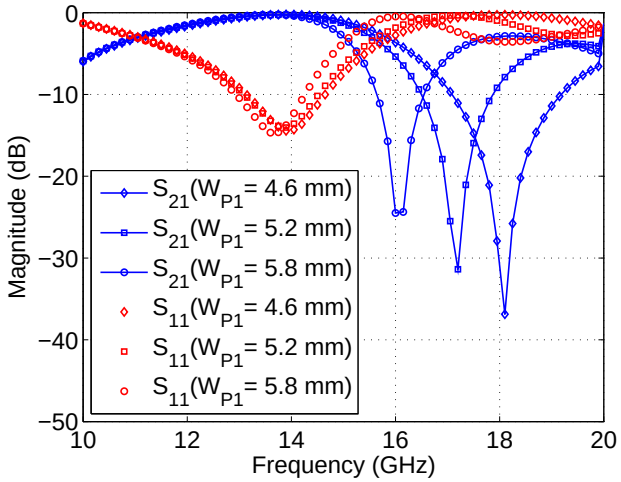

(a)

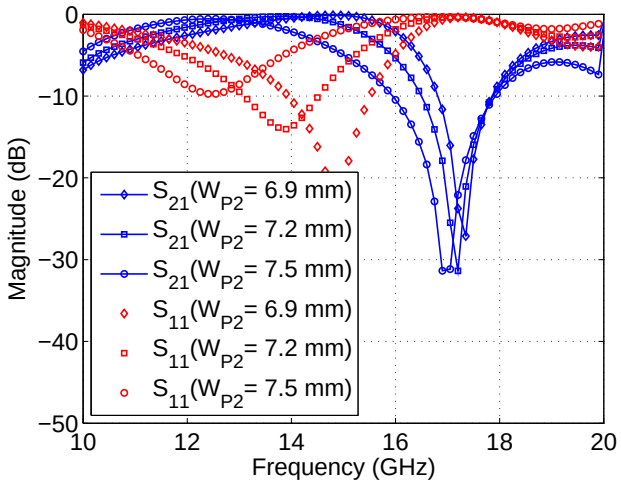

(b)

Figure 4.6: Variation of the simulated frequency responses of the WG-SSL transition with respect to W_{P1} and W_{P2}. (a) Adjustment of W_{P1} with $W_{P2} = 7.2$ mm (b) Adjustment of W_{P2} with $W_{P1} = 5.2$ mm

$$\lambda_0/3 \leq W_{P2} \leq \lambda_0/2, \tag{4.1}$$

where λ_0 is the wavelength at center frequency, f_0. Due to the proximity of the patch to the waveguide side walls and the resulting fringing fields, the patch dimensions need to be tuned very close to the lower bound of (4.1) to achieve the desired resonant

frequency. The dimension W_{P1} of the first patch determines the magnitude of the cross-coupling coefficient, which specifies the location of the transmission zero. One can achieve a broader frequency bandwidth by moving the frequency of the transmission zero away from the passband. Since no closed-form solution exists for this phenomenon, numerical simulation and optimization can be performed to find the optimal dimension.

Increasing the distance h_G between the patch and its ground results in a broader bandwidth at the expense of increased volume. The channel width of the suspended stripline, W_C, must be carefully selected for a proper transmission response. The metallic guide hosting the SSL also serves as a rectangular waveguide of dimensions $W_C \times 1$ mm. In order to prevent any waveguide mode from propagating within this guide, W_C needs to be narrower than a half wavelength. Under this condition, only the SSL mode will propagate as all the waveguide modes are evanescent.

4.1.4 Fabrication and Measurement

Two WG-SSL transitions were cascaded in a back-to-back configuration to form an SSL-WG-SSL transition. For measurement purposes, two end-launch SMA connectors were also added to the SSL ports. Photographs of this transition are shown in Figure 4.7. To remove the effect of the SMA connectors and the coax-to-SSL transitions, TRL calibration was performed and the measurement plane was set at the broad wall of the waveguide (see Figure 4.3). More information about the TRL calibration standards for this transition are available in Appendix C.2.

Scattering parameters of the back-to-back transition were measured with an Agilent N5230A network analyzer. Figure 4.8 compares the measured and simulated frequency responses of the SSL-WG-SSL transition. Except for a slight shift in the center frequency, the simulated and measured results show an excellent agreement. The IL of the back-to-back transition is 0.18 dB at 13.8 GHz, making the IL of a

single transition equal to 0.09 dB. The 10-dB RL bandwidth of 12% is observed in measurement.

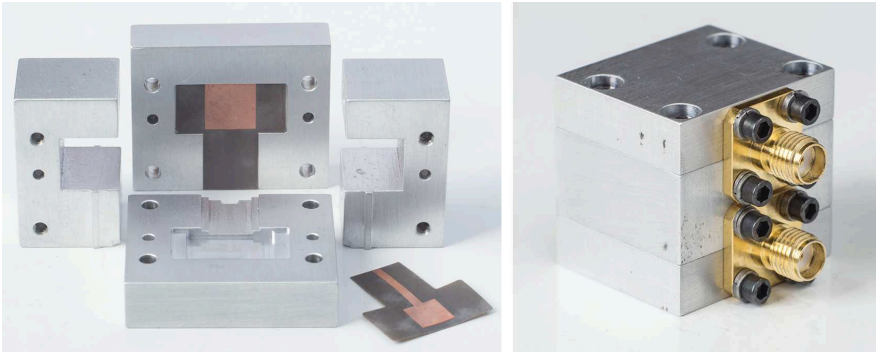

Figure 4.7: Photographs of the dismantled and assembled SSL-WG-SSL transition

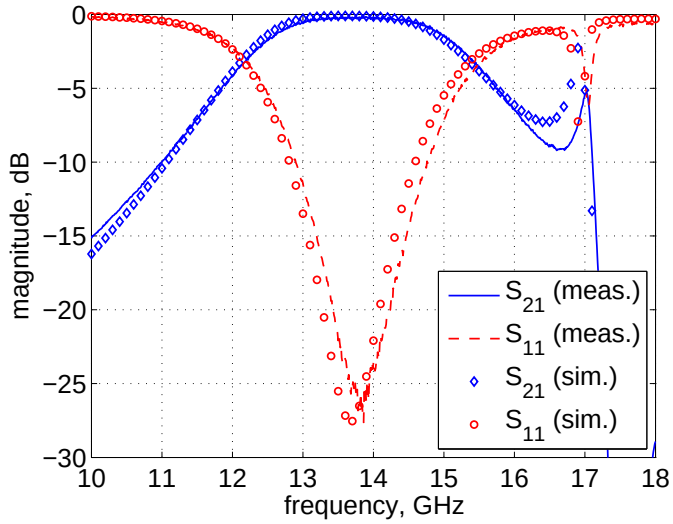

Figure 4.8: Simulated and measured frequency responses of the SSL-WG-SSL transition

The resonance around 17 GHz is due to the two transition junctions and the WG transmission line in-between, which together form a resonant structure. The cavity formed sby the waveguide and two transitions at both ends will resonate when the length of the waveguide becomes an integer multiple of a half wavelength, which occurs around 17 GHz for the lowest-order mode.

4.1.5 Comparison

Table 4.1 compares the transition characteristics of this work with other WG-SSL transitions as well as several WG-MS transitions. This paper uses patch elements to reduce the size and IL of the transition for a comparable BW, as opposed to using a simple probe and a long back-short in [80]. The BW of the WG-MS transition in [82] is comparable to this design. It does not need a back-short but it still needs a cover plate to shield the MS from surrounding environment. The WG-SSL in [83] needs a longer back-short and its measured BW is narrower than this design.

Table 4.1: Measured results of several WG-SSL and WG-MS transitions

Paper	Output	BW (@ RL)	IL (@f_0)	Back-short
[80]	MS	16% (10 dB)	0.25 dB (30 GHz)	$\lambda_g/4$
[82]	MS	10% (15 dB)	0.30 dB (76 GHz)	None
[83]	SSL	5.7% (14 dB)	0.21 dB (26 GHz)	$\lambda_g/10$
This	SSL	12% (10 dB)	0.09 dB (14 GHz)	$\lambda_g/30$

CHAPTER 5

C-BAND SUBARRAY

In this chapter, the design, simulation, and fabrication of the frequency-scanning array for C band will be discussed.

5.1 Review of Slot Antennas

Slot antennas are very small in one dimension and easy to integrate in the shared-aperture array. In Section 2.2, it was discussed how a slot antenna is a great candidate for the application of this work. The cross-polarization of slot antennas are generally very low and they can be excited directly by planar circuits, like SSLs. These properties make them great candidates for the antenna elements of shared-aperture arrays.

A basic slot antenna is shown in Figure 5.1(a). It consists of a rectangular cut in a large thin flat sheet of metal with the slot free to radiate on both sides of the sheet.

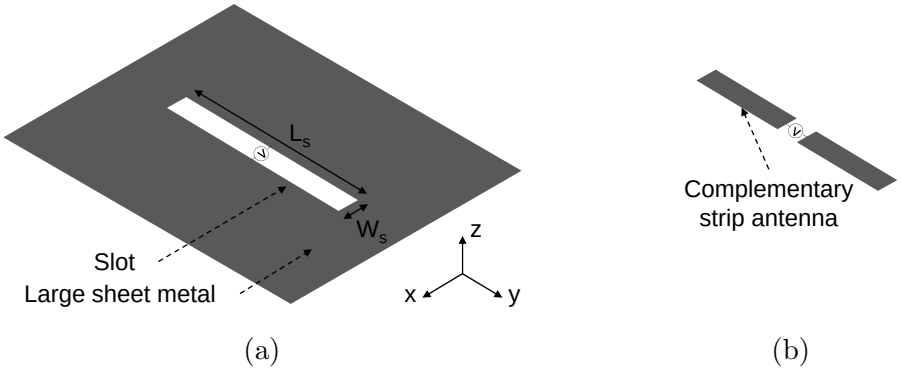

Figure 5.1: Configuration of a basic slot antenna on a large sheet metal (a) and its complementary strip antenna equivalent (b).

The slot is excited by a voltage source such as a balanced parallel transmission line connected to the opposite edges of the slot at its center.

The electric field distribution in the slot can be obtained from the relationship between the slot and complementary strip antennas, as shown in see Figure 5.1(b). It has been shown that the electric field distribution (magnetic current) in the slot is identical to the electric current distribution (magnetic field) on the complementary strip. In the illustrated rectangular slot, the electric field is perpendicular to the long dimension, and its amplitude vanishes at the ends of the slot [64]. Thus, the fields radiated by this antenna are linearly polarized in the $\hat{x}$ direction, namely E-polarized in this work. For the H-polarized radiation, the slot should be rotated by 90° around the z-axis.

In practical designs, since one side is either completely enclosed or it is desired that the radiation on one side be minimized, the slot antenna is not free to radiate on both sides of the surface. Also, mechanical fabrication restrictions often require that the slot be cut in something other than a thin sheet. In these cases, the influence of the thick metal sheet on the impedance and radiation efficiency of the slot antenna is significant.

In Figure 5.1(a), the dimension of the slot is $L_s \times W_s$. The slot length L_s is usually about $\lambda/2$ at the center frequency. But there is not always enough room for that in the arrays with certain limitations on lattice shape and element spacing. To shift the resonant frequency of a smaller slot down to the desired band, one can load it at the ends (e.g., I shaped slot) or add a layer of dielectric with $\epsilon_r > 1$ over it. The former degrades polarization purity, hence will not be considered in this work. The latter will be discussed in more detail in Section 5.5.

Narrower slots have better cross-polarization isolation but they tend to be narrowband [64]. A practical design may result from a compromise between these two

properties. It should also meet the requirements of the milling process for fabricating the slots.

Slot antennas can be fed in several ways: tapping into a transmission line, coupling to a resonant cavity, and feeding them directly with voltage sources [64]. In this research, we will use the first method whereby slots are cut along an SSL. When a slot is cut into the ground plane of an SSL and it interrupts the flow of current, forcing it to go around the slot, power is coupled from the transmission line through the opening to free space.

There are several approaches to control the power coupled to a slot. One way to do that is offsetting the crossing point of the feed-line from the center of the slot. Another way of doing that is varying the length of the slot L_s. In this work, we decided to use the second method, i.e. varying L_s, without offsetting the SSL from the center of the slot. This makes the design of the feeding SSL easier, since it eliminates the need for large phase compensations caused by offsetting.

5.2 Review of Slot Arrays

The most popular slot array is the slotted-waveguide which has been studied extensively. Slots can be on the broad-wall or the narrow-wall of the waveguide. Figure 5.2 shows different types of on a rectangular waveguide. The functionality of each of these slots is described in [64] as: "Slot g does not radiate because the slot is lined up with the direction of the sidewall current. Slot h does not radiate because the transverse current is zero there. Slots a, b, c, i, and j are shunt slots because they interrupt the transverse currents (J_x , J_y) and can be represented by two-terminal shunt admittances. Slots e, k, and d interrupt J_z and are represented by series impedance. Slot d interrupts J_x, but the excitation polarity is opposite on either side of the waveguide centerline, thus preventing radiation from that current component. Both J_x and J_z excite slot f. A Pi- or T-impedance network can represent it." One

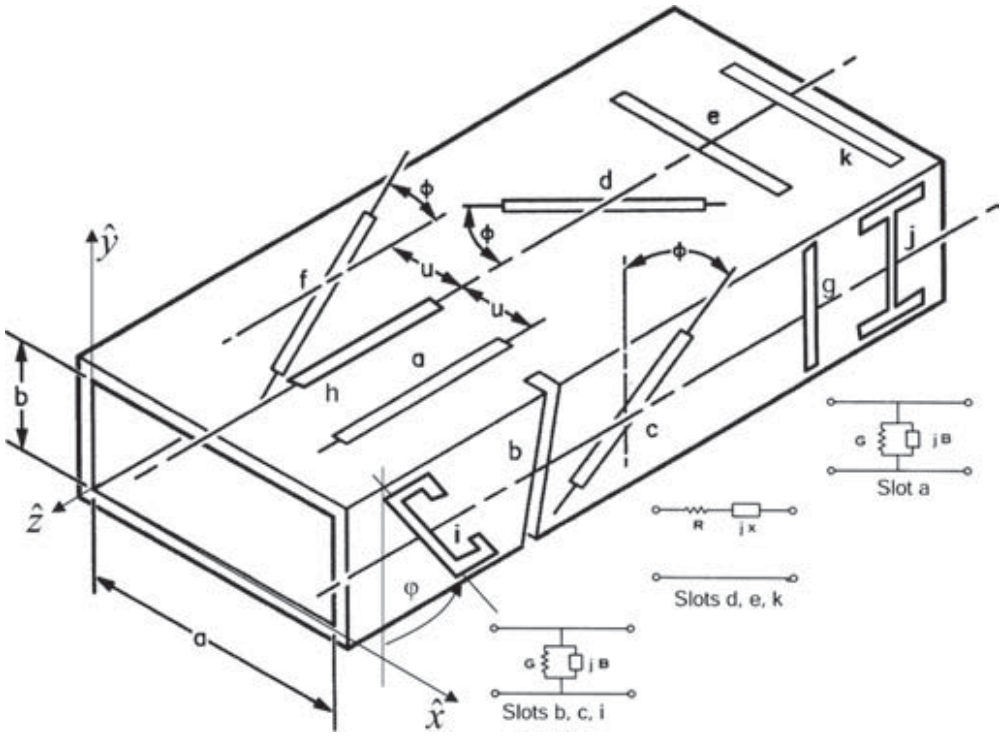

Figure 5.2: Different types of slot cut in the broad-wall and narrow-wall of a rectangular waveguide [64].

can control the power coupled to a slot by rotating/displacing it with respect to a peak current direction/location.

Waveguide slot arrays are also classified by the nature of the wave inside waveguide: standing-wave arrays and traveling-wave arrays. The standing wave arrays have elements spaced $\lambda_g/2$ and radiate a beam broadside to the waveguide [64]. They are usually fed at one end of the waveguide with the other end terminated by short circuit. Traveling-wave arrays are preferred in applications where the main beam is tilted or where frequency scanning is desired. Element spacing should not be $\lambda_g/2$ and the end of the waveguide must be terminated in a matched load.

The main disadvantage of waveguide slot arrays is their size and weight, especially when they require snake feed for frequency scanning. Addition of another polarization

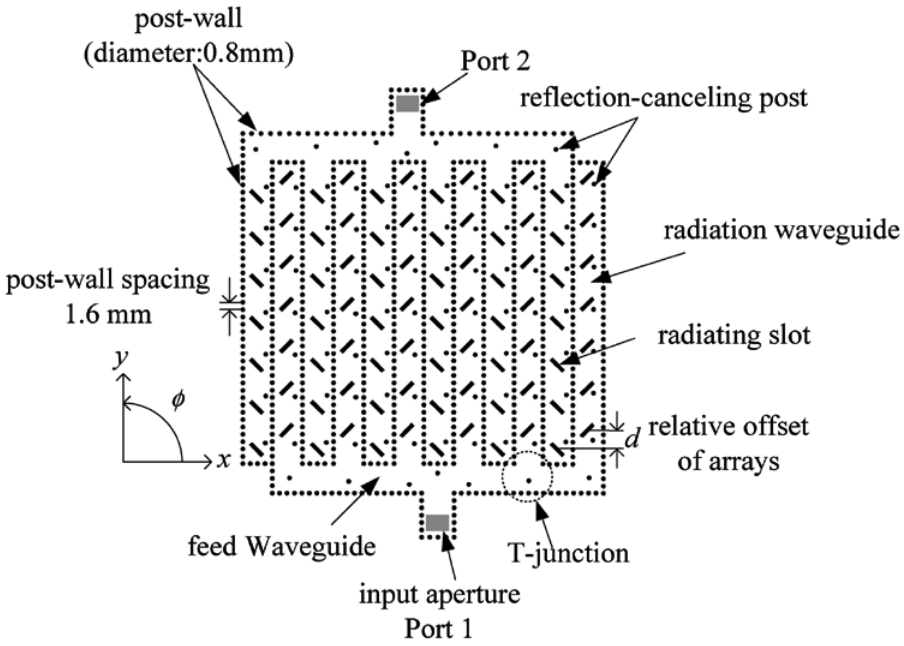

Figure 5.3: A parallel-plate slot array for dual-linear polarization radiations at broadside [88].

and another frequency band makes their design even more complicated. Planar slot arrays are more compact. Figure 5.3 shows a parallel-plate slot array on a single substrate. This is a standing-wave slot array for broadside radiation of orthogonal 45° linearly-polarized waves [88]. It lacks the frequency scanning capability.

It is extremely easier to realize snake feeds with planar transmission lines such as MS, SL, or SSL than with bulky waveguides. The compactness of planar transmission lines allows us to integrate four of them in a shared aperture, as needed for two polarizations and two frequency bands. The other concern is the insertion loss. We choose to use SSL snake feeds to excite slot antennas, since they are very low profile and have very low insertion loss. To the author's knowledge, unlike waveguide slot arrays, not much work has been reported in the literature on slot array antenna fed by SSL. This work is the first of its kind.

5.3 Single Element

To assess the characteristics of the antenna in C band, feeds and slots responsible for the C-band radiation has been designed and analyzed. We will start with analyzing a single slot for the E-polarization. Then we will add another slot for the H-polarization and study their performances taking the interaction between them into account.

The aluminum housing and the SSL feed are shown in Figure 5.4. The SSL feed is meandered to increase the total length between ports such that the desired phase factor of 1.45 is achieved. The dimensions of the slot are given by $L_s \times W_s$. The slot is designed to be as narrow as possible for polarization purity. Considering the fabrication limitations, we chose $W_s = 1$ mm. L_s will be varied to control the coupling between the slot and the SSL delay-line. The upper face of the aluminum housing is modeled as an infinite ground plane. Top and side faces of the (invisible) air-box are modeled as radiation boundaries.

Figure 5.5 plots the magnitude and phase of the transmission coefficient S_{21} as a function of frequency. As seen in Figure 5.5(a), longer slots result in lower $|S_{21}|$ which means that more power is radiated through the slot. For C-band element spacing of $0.45\lambda_C$ and slow-wave phase factor of 1.45, the required feed-line phase delay between

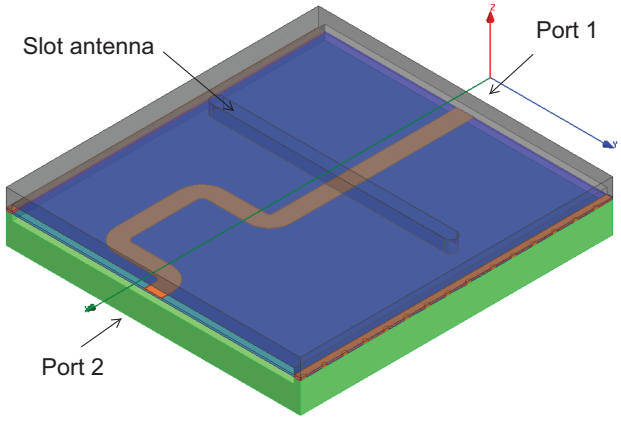

Figure 5.4: C-band slot and the SSL feed models in Ansys HFSS. $W_s = 1$ mm.

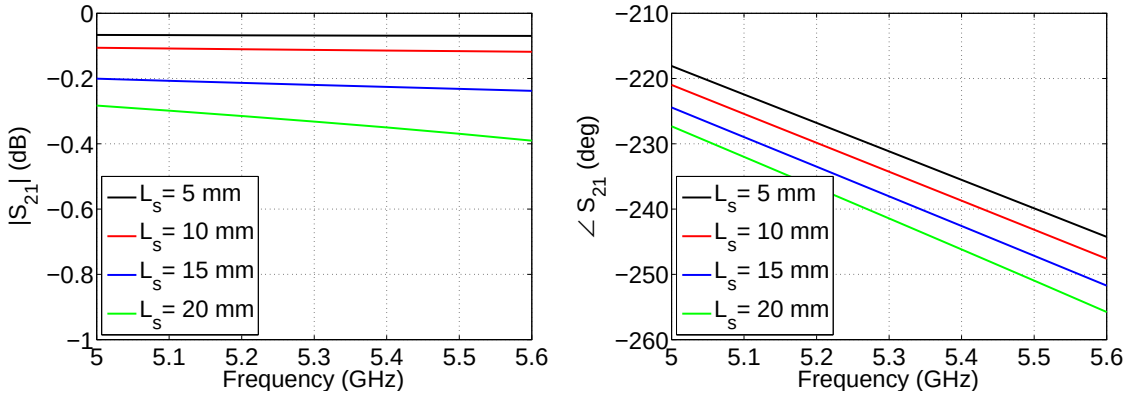

(a) (b)

Figure 5.5: Simulation results of the C-band slot and the SSL feed. (a) The magnitude of the transmission coefficient. (b) The phase of the transmission coefficient.

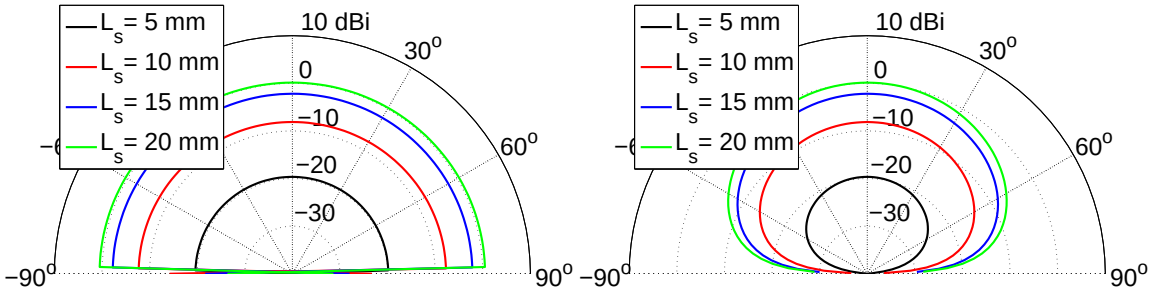

(a) (b)

Figure 5.6: Simulated total gain of the C-band slot. (a) E-plane. (b) H-plane.

two consecutive slots should be equal to $(0.45 \times -360^\circ) \times 1.45 \approx -235^\circ$ at the center frequency of 5.3 GHz. Figure 5.5(b) shows that the phase differences between ports 1 and 2 are very close to this value. However, varying the length of slot yields some deviation from -235°. The amount of meandering can be fine tuned for different slot lengths to achieve the desired phase delay.

The simulated total gains of the slot antenna are plotted in Figure 5.6 for several slot lengths, for both E- and H-planes. Clearly, the total gain increases with the length of the slot.

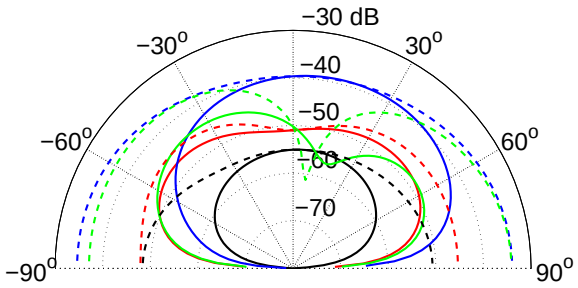

Figure 5.7: Simulated cross-polarization levels of the C-band slot. Solid lines correspond to the H-plane, and dashed lines correspond to the E-plane calculations.

For a single slot, the cross-polarization level is plotted in Figure 5.7 for several slot lengths, for both E- and H-planes. It is as low as −40 dB at broadside and is better than −33 dB at other angles.

5.4 Subarray

The C-subarray consists of two perpendicular slots and SSL feed-lines. In this section, the interaction between the two slots will be studied. Two possible arrangements for the slots in a rectangular lattice are shown in Figure 5.8. Because of the symmetrical placement of the slots in Figure 5.8(b), better cross-polarization isolation is expected.

Table 5.1 compares the simulated cross-polarization levels for an array of two perpendicular slots with dimension 15 mm×1 mm in the two arrangements shown in Figure 5.8. Cross-polarization levels are calculated on the scan plane ($\phi = 0°$). A significant decline in the cross-polarization level is obtained using the arrangement of Figure 5.8(b).

The dual-polarized C-subarray shown in Figure 5.9 has been designed and simulated using Ansys HFSS. The upper face of the aluminum housing is modeled as an infinite ground plane. Top and side faces of the (invisible) air-box are modeled as

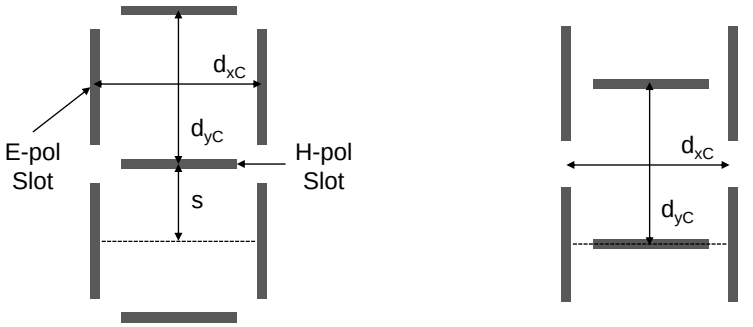

(a) (b)

Figure 5.8: Two possible arrangements for E-pol and H-pol slots in a rectangular lattice. (a) $s = d_{yC}/2$. (b) $s = 0$.

Table 5.1: Comparison of the simulated cross-polarization levels for an array of two perpendicular slots for two different arrangments.

Arrangmet	Excited slot	Cross-polarization
Figure 5.8(a)	E-pol	-22 dB
Figure 5.8(a)	H-pol	-13 dB
Figure 5.8(b)	E-pol	-38 dB
Figure 5.8(b)	H-pol	-40 dB

radiation boundaries. A wall of plated vias has been placed between the two SSLs in order to prevent coupling. Hence, the isolation between the SSL circuits is maximum.

The radiation patterns of the subarray in both planes for both polarizations are shown in Figure 5.10. For both polarizations, the cross-polarization levels are better than -25 dB in the desired range of scan angles ($-60° < \theta < -40°$ on the scan plane).

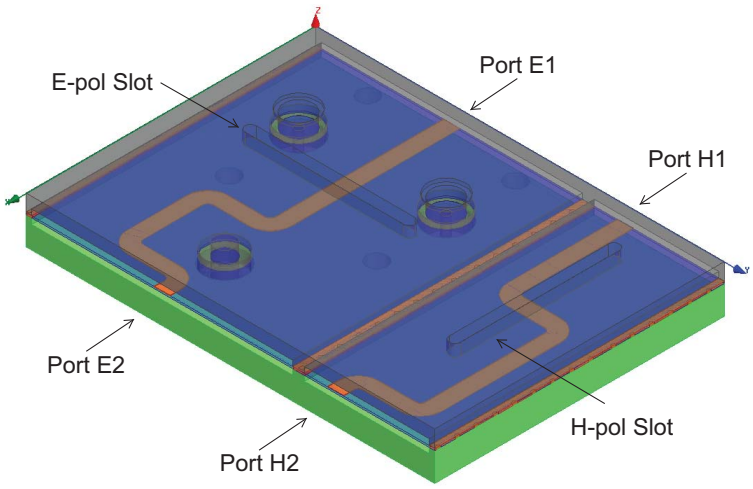

Figure 5.9: A dual-polarized C-subarray consisting of two perpendicular slots and SSL feed-lines.

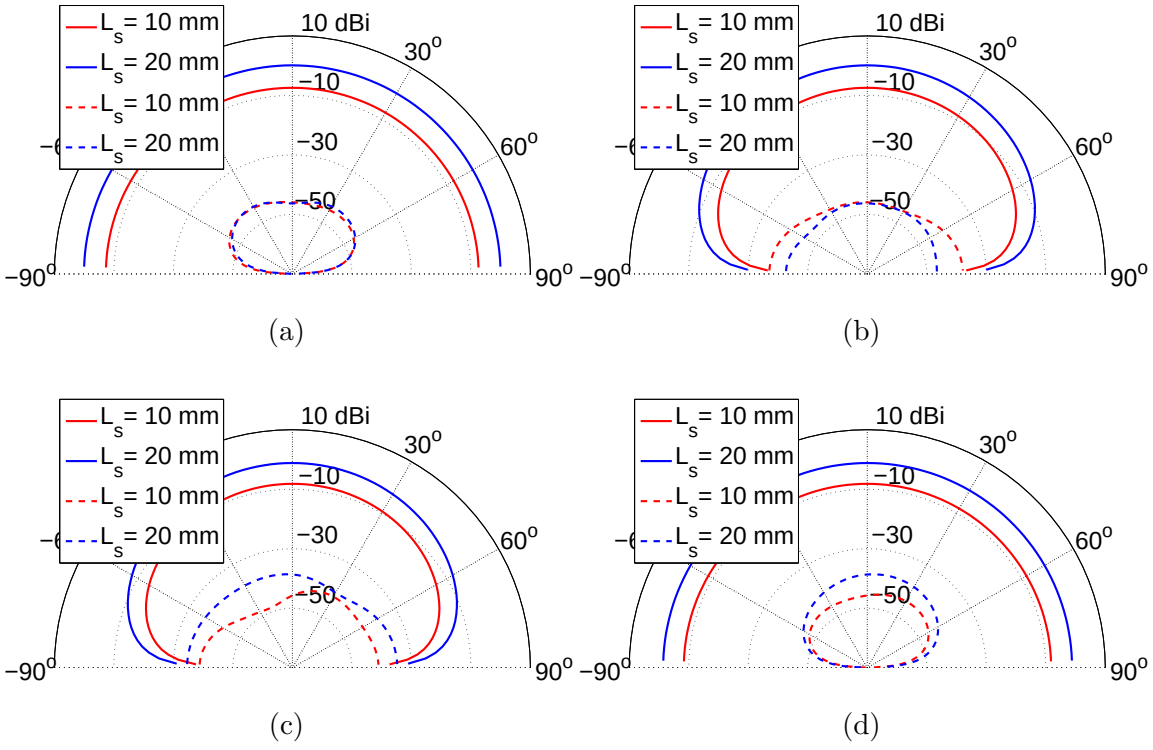

Figure 5.10: Simulated co-polarized (solid lines) and cross-polarized (dashed lines) radiation gains of the C-subarray. (a) Scan plane ($x-z$) for E-pol slot excitation. (b) Orthogonal plane ($y-z$) for E-pol slot excitation. (c) Scan plane for H-pol slot excitation. (d) Orthogonal plane for H-pol slot excitation.

5.5 Covering with Dielectric

As noted before, in this design, there is not enough room for the slots to be $\lambda/2$ long at the center frequency 5.3 GHz. To shift the resonant frequency of the smaller slot down to the desired band, we decided to make use of the existing Ku-subarray PCB as a low-loss dielectric cover over the slots. The ground planes of the 8-layer Ku-subarray PCB are designed in a way that they do not disturb the radiation path from the slot to free-space significantly. This method is shown in Figure 5.11. To prevent the C-band fields from penetrating into the Ku-band circuitry and exciting parallel-plate propagating modes, a conducting wall around the perimeter of each slot is created. This is implemented using a series of closely-spaced grounded vias around the slots in the 8-layer PCB.

Table 5.2 compares the simulated radiation efficiency ϵ_{rad} of a slot with and without the 8-layer PCB. The dimensions of the slot are given by 20 mm$\times$1 mm and infinite ground plane boundary condition is applied to the upper face of the aluminum housing. Using dielectric covers, the radiaion efficiencies are increased more than twofold for both slots.

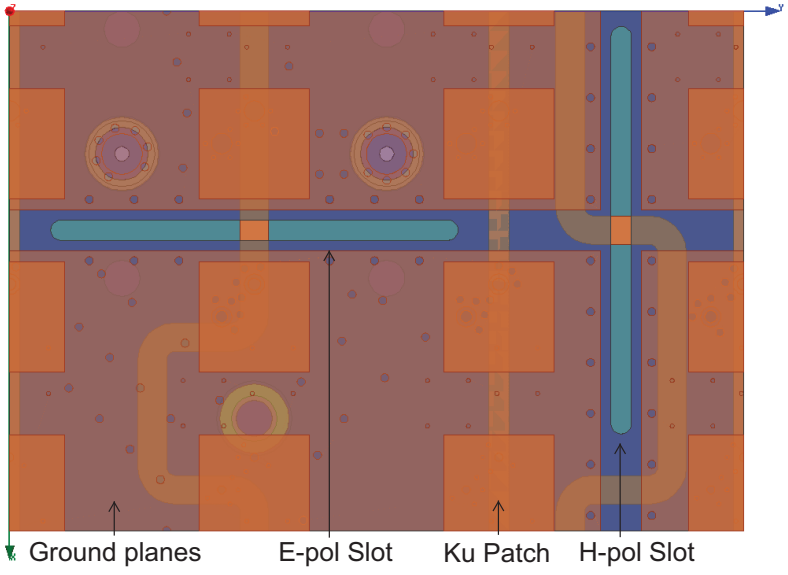

Figure 5.11: C-subarray covered by the Ku-subarray 8-layer PCB

Table 5.2: Comparison of the simulated radiation efficiencies of a slot with and without the dielectric cover.

	Slot	ϵ_{rad}
Without Cover	E-pol	39%
Without Cover	H-pol	40%
With Cover	E-pol	89%
With Cover	H-pol	85%

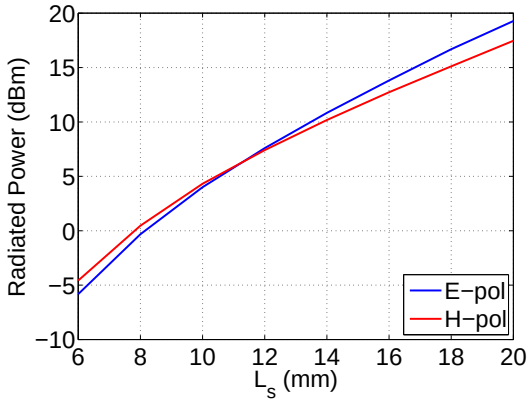

Figure 5.12: Radiated power of the slot as a function of slot length, L_s. The available power is 1 W.

Figure 5.12 shows the radiated power by the E-pol and H-pol slots as a function of their lengths. It uses the simulation model of Figure 5.11 with 1 W input power. This graph is useful for the defining slot lengths to achieve the desired aperture illumination taper.

5.6 Infinite Array

To evaluate the performance of the C-band slots in an infinite array environment, we have re-simulated the model in Figure 5.11 with PBCs on side faces and PML on top face of the (invisible) air-box. The PBCs impose equal electromagnetic field magnitudes and phases on the side faces perpendicular to $\hat{y}$, because there is no scan in this direction. On the side faces perpendicular to $\hat{x}$, the PBCs dictate equal elec-

tromagnetic field magnitudes and a phase difference of -235° at the center frequency $f = 5.3$ GHz.

Figure 5.13 plots the radiation patterns of the subarray in both planes for both polarizations, with taking the mutual coupling effects into account. Slot dimensions are given by 20 mm×1 mm. Maximum co-polarized gains of 4.43 dBi and 1.57 dBi are estimated for the E-pol and H-pol slots, respectively. The cross-polarized gains are less than -38 dBi and -29 dBi at any angle θ, for the E-pol and H-pol slots, respectively.

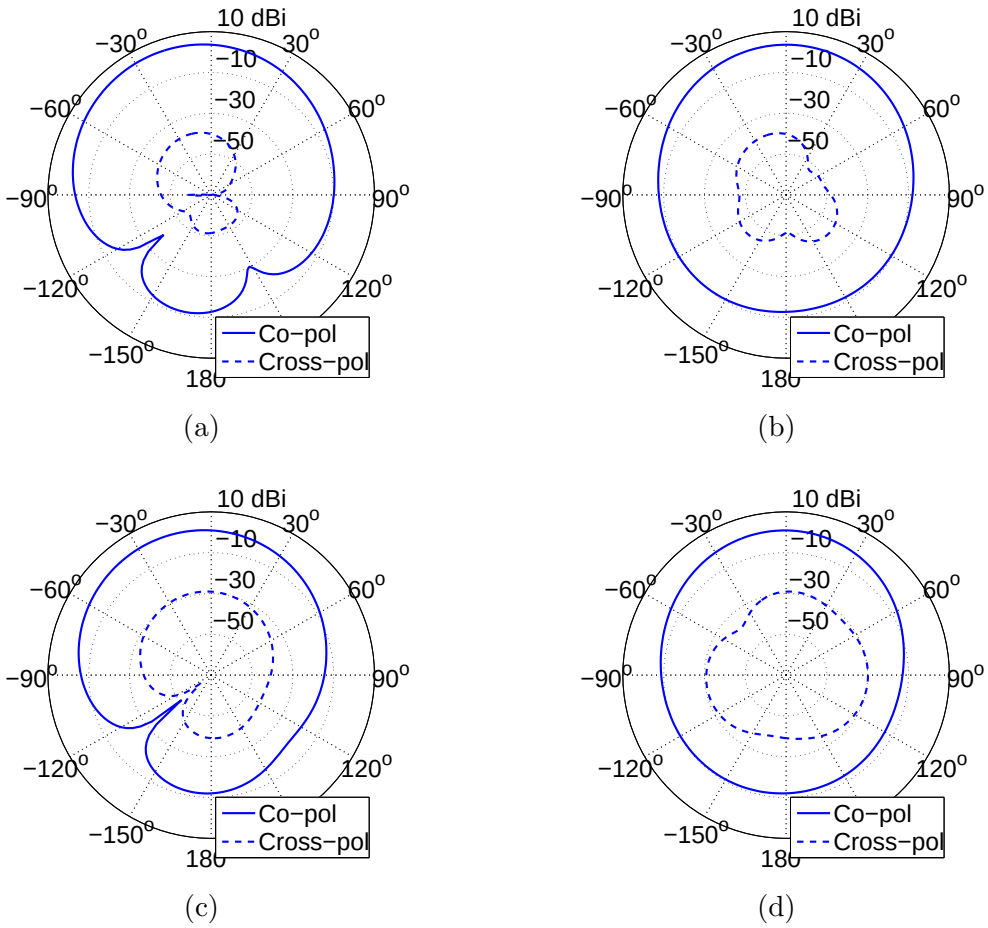

Figure 5.13: Simulated co-polarized and cross-polarized radiation gains of the C-subarray at $f = 5.3$ GHz. (a) Scan plane $(x - z)$ for E-pol slot excitation. (b) Orthogonal plane $(y - z)$ for E-pol slot excitation. (c) Scan plane for H-pol slot excitation. (d) Orthogonal plane for H-pol slot excitation.

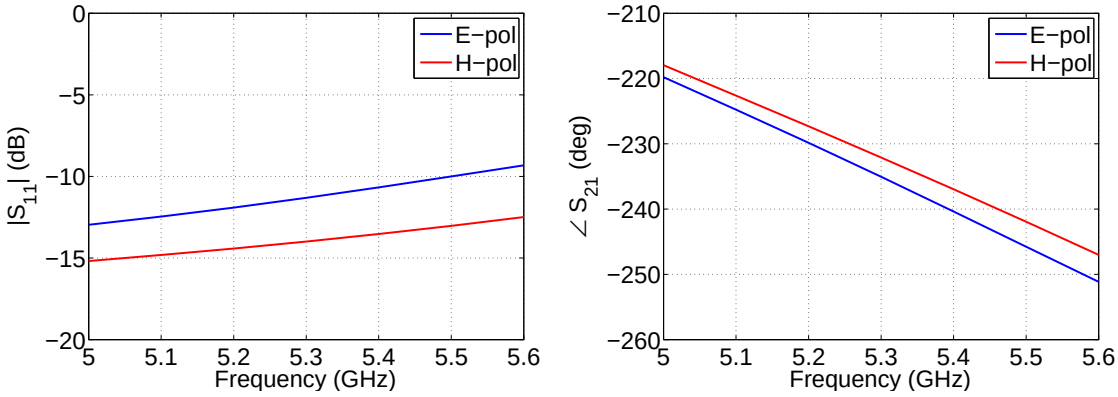

(a) (b)

Figure 5.14: Simulated S-parameters of the C-subarray with PBCs. (a) The magnitude of the reflection coefficient. (b) The phase of the transmission coefficient.

Figure 5.14 plots the $|S_{11}|$ and the $\angle S_{21}$ of the C-subarray with PBCs as a function of frequency. The return loss at the input ports are better than 9 dB at any frequency, for both polarizations. This is for a 20 mm-long slot. For shorter slots, better return losses are expected, since they disturb the current path less. For this research, the maximum slot length will be 20 mm, since it's a large array and a very small power will be coupled to every slot antenna. The phase differences between the input and output ports of the subarray are very close to the desired value of -235° at center frequency 5.3 GHz, as seen in Figure 5.14(b).

5.7 Measurement Results

A slot on a finite ground plane is fabricated and its radiation properties and S-parameters are measured. It is shown in Appendix D that in order to measure the active impedance of the slot, we need to enclose one and half slot antennas within the metallic walls of a rectangular waveguide. This enables us to measure the impedance of the slot antenna as if it is in an infinite array of like elements. Appendix D discusses the theory and design procedure of waveguide simulators in more details.

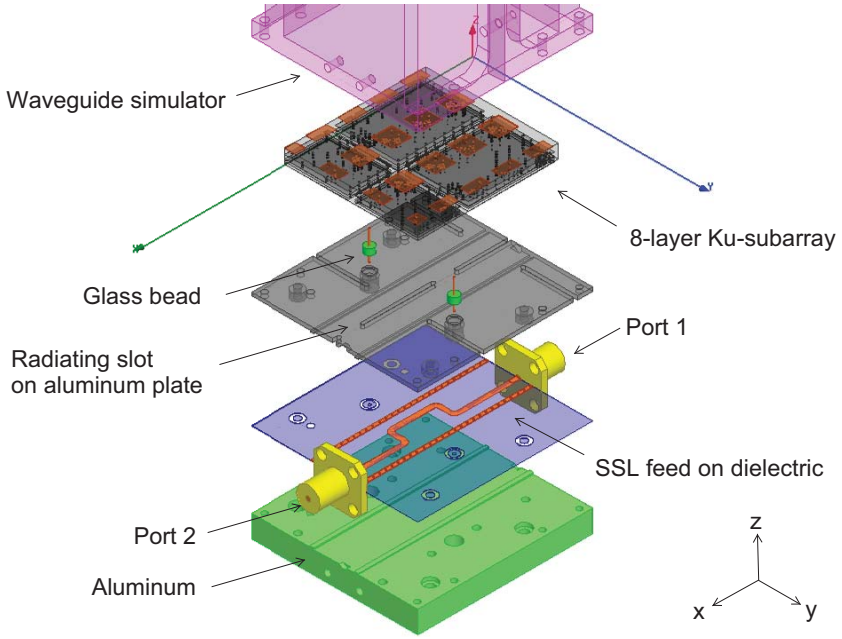

Figure 5.15: Exploded view of the C-band slot, the SSL feed and the waveguide simulator.

The fabricated parts are shown in Figure 5.15. This model is a slice of the full array. It consists of one H-polarized full slot, and a half slot. In addition, there are four E-polarized partial slots. As discussed in Appendix D, it is only practical to measure the active impedance of the H-polarized slots. Hence, only the full slot is excited which radiates H-polarized fields. The excitation is via an SSL feed. There is a section of the 8-layer PCB on top of the slots, as discussed in Section 5.5. For active impedance measurements, a waveguide simulator will be used. The other end of the waveguide simulator is terminated with an RF absorber.

5.7.1 In Free-space

In order to measure the radiation patterns and the standalone S-parameters of the slot, the waveguide simulator of Figure 5.15 is removed. Figure 5.16 shows the photograph of the antenna under test (AUT). The Network Analyzer is calibrated using a custom TRL calibration kit (see Appendix C.3). The input and output

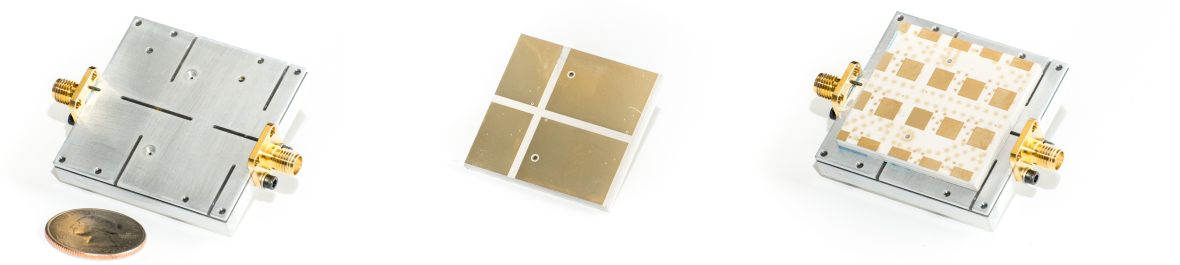

(a) (b) (c)

Figure 5.16: Photographs of the C-band AUT. (a) The slot and its feed. (b) Back side of the 8-layer PCB. (c) Assembled.

calibration planes are put on the SSL feed lines at the center of the adjacent slots. This allows us to accurately measure the phase delay and insertion loss of the feed line between two consecutive slot elements.

Figure 5.17 shows the simulated and measured S-parameters of the H-polarized slot antenna radiating into free-space. The insertion loss (including radiation through slot) is between 0.5 dB and 0.6 dB and the return loss is better than 12 dB in the frequency band of 5.0—5.6 GHz. The measured phase delay at the center frequency $f = 5.3$ GHz is -235.5° which is very close to the required phase delay of -235° (see Section 5.3).

Figure 5.18 shows the measurement setup in the antenna chamber. The radiation patterns of the slot on the scan plane ($x-z$) and the orthogonal plane ($y-z$) are shown in Figure 5.19. Each graph plots both co-polarized and cross-polarized gains. The start (5.0 GHz), mid-band (5.3 GHz) and stop (5.6 GHz) frequencies are simulated and measured.

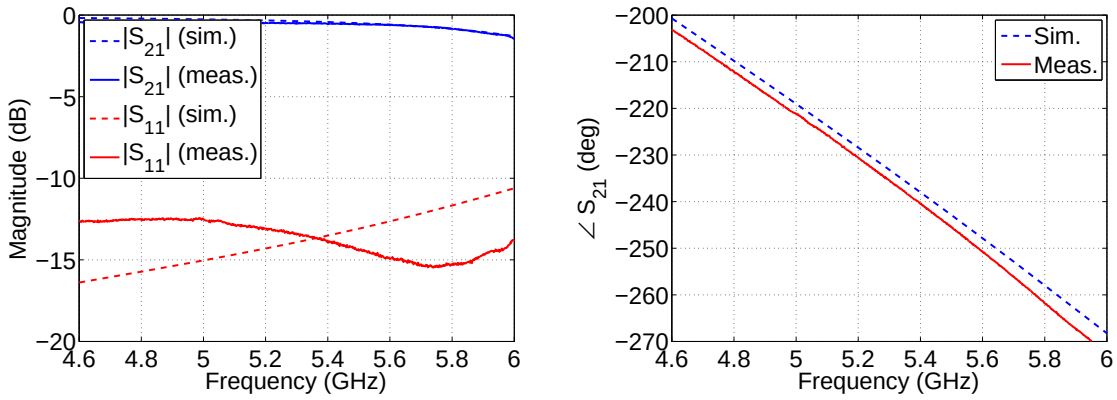

(a) (b)

Figure 5.17: Simulated and measured S-parameters of the C-band slot. (a) The magnitude. (b) The phase.

Figure 5.18: Photograph of the C-band slot in the far-field chamber.

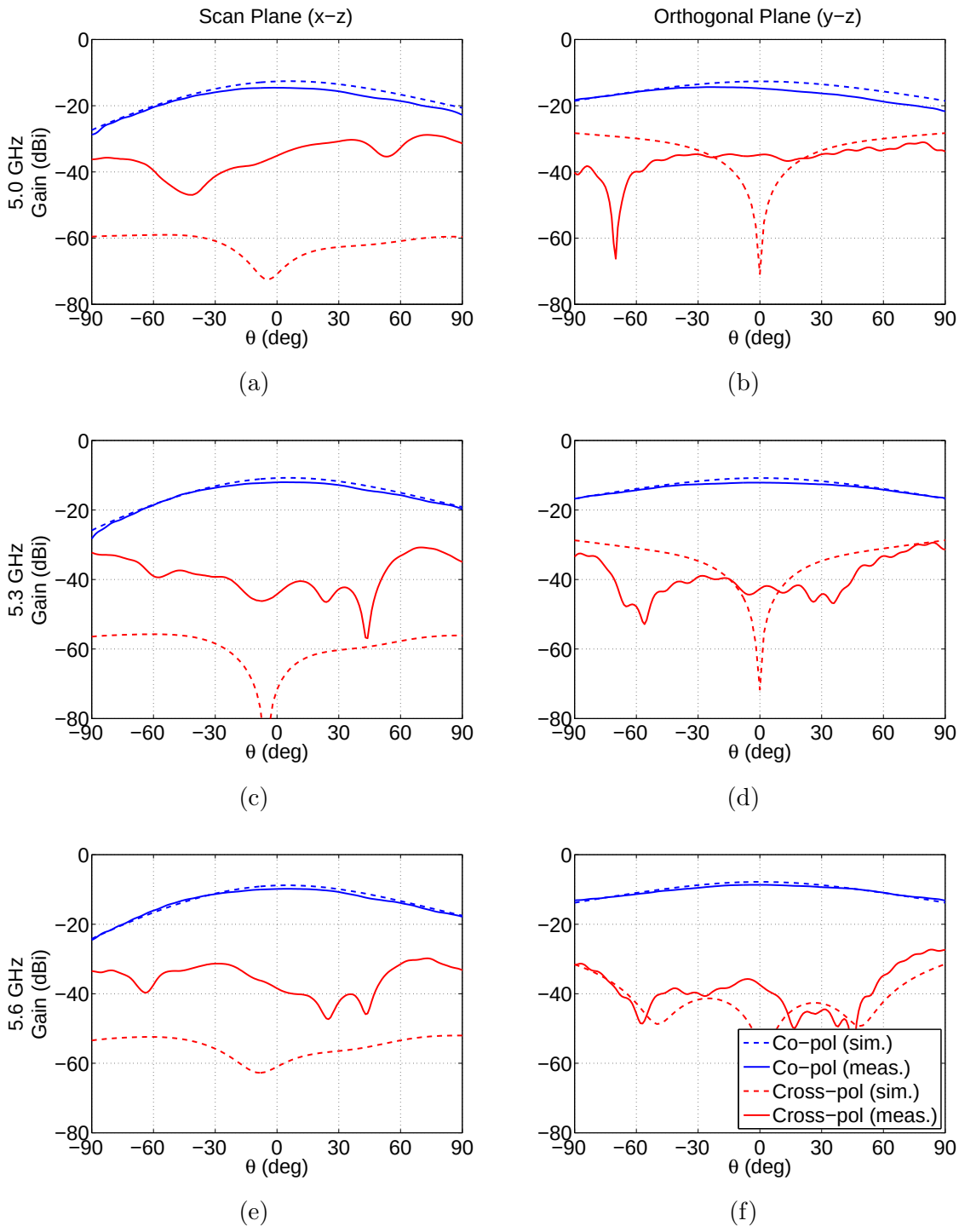

Figure 5.19: Co-pol and cross-pol realized gains of the C-band slot. All graphs have the same legend. (a) Scan plane at 5.0 GHz. (b) Orthogonal plane at 5.0 GHz. (c) Scan plane at 5.3 GHz. (d) Orthogonal plane at 5.3 GHz. (e) Scan plane at 5.6 GHz. (f) Orthogonal plane at 5.6 GHz.

The measured and simulated co-polarized gains agree very well. Although the measured cross-polarization levels are very different from simulation result, they are better than -20 dB in the desired range of scan angles ($-60^\circ < \theta < -40^\circ$ on the scan plane).

The discrepancy between simulated and measured cross-polarization levels can be explained by the effect of prasitic radiations. Since this is a very low gain antenna ($<$ -10 dBi), parasitic radiations from other parts of the setup—the cable, for instance—may be large and contribute to high cross-polarization levels.

An insertion loss of 0.5 dB (Figure 5.17(a)) means that less than 10% of input power is radiated through the slot. The remaining 90% of power is transferred from port 1 to port 2 (Figure 5.15). The large amount of power that propagates in the transmission lines creates substantial surface currents which may find their way to the outside surface of the AUT, due to the fabrication and assembly imperfections. Any current on the outer surface of the AUT or setup is capable of radiating energy and increasing the cross-polarization levels.

As a proof of this argument, we revised the simulation model as shown in Figure 5.20(a). Instead of directly exciting the SSL feed line with ideal wave ports, this model includes SMA connectors and a cable excited from the open end. The SMA connectors and the cable are precisely modeled to represent the actual components accurately. The simulated and measured radiation patterns on the scan plane at the center frequency $f = 5.3$ GHz are shown in Figure 5.20(b). Clearly, the simulated cross-polarization level is significantly increased by about 30 dB compared to Figure 5.19(c). It now agrees very well with the measurement result.

There are many surface currents that contribute to the cross-polarized radiations: currents on the right-angle bend, on the SMA connectors, and on the cable. Note that in this model we have used a right-angle bend to align the axis of cable with the desired polarization. In other words, parasitic surface currents (J_y) on the longer portion of

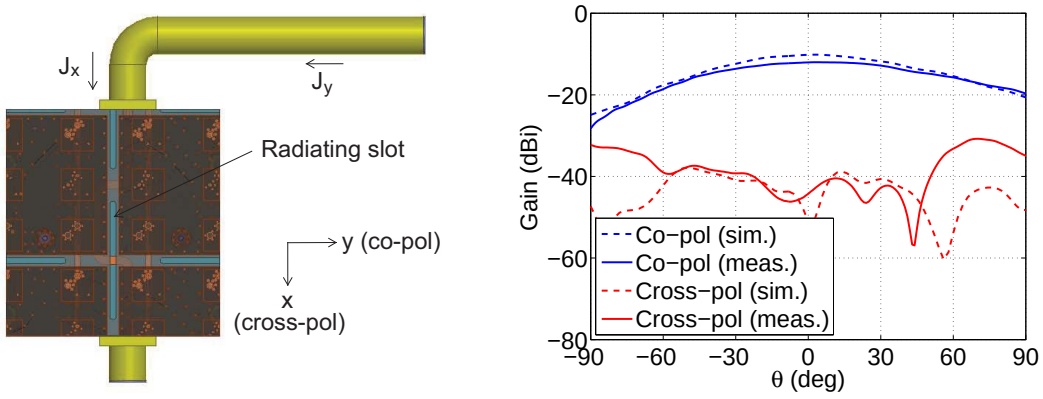

(a) (b)

Figure 5.20: The effect of parasitic surface currents on cross-polarization level. (a) The HFSS model. (b) Realized gains on the scan $(x-z)$ plane at $f = 5.3$ GHz.

the cable should generate co-polarized fields (E_y). Nevertheless, cross-polarization level is still high.

In practice, not only is it impossible to mitigate all of these surface currents but also it is very difficult to perfectly align the cable in the preferred direction, while measurement. In the full array case, however, much greater percentage of power will radiate through the slot array. Therefore, parasitic currents will be negligible and cross-polarization levels may be lower.

Another source of parasitic radiation is the exposure of the TEM waves inside SMA connector to free-space at its mating plane with the SSL. Figure 5.21 shows how fields can leak out of the AUT when travelling from the connector to the SSL. This might be a strong source of cross-polarized radiation. For practical reasons, it is impossible to completely diminish this exposure in the current measurement setup. In the full array case, there will not be any end-launch connectors; the SSL will be fed by a rectangular waveguide and the waveguide will be excited by a probe. Therefore, all feeding structures and transitions will be confined inside AUT, without any exposure to free-space.

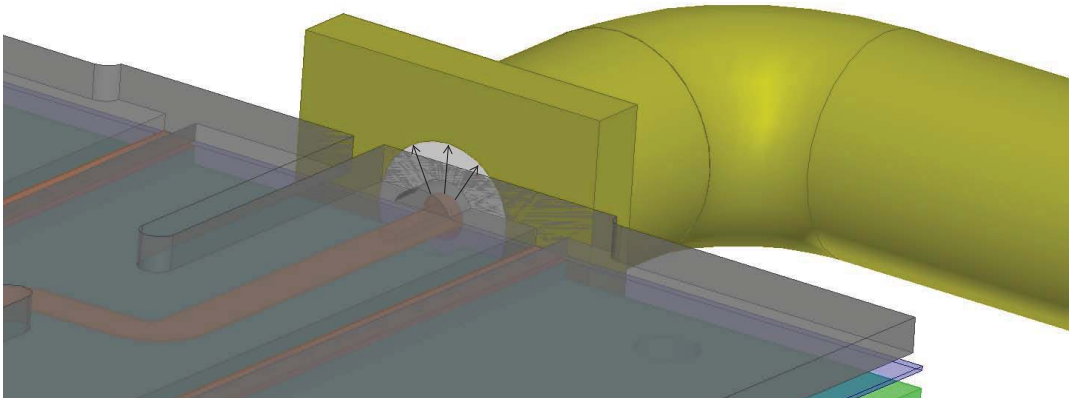

Figure 5.21: TEM fields inside SMA are exposed to free-space at the mating plane of the SMA with the SSL. These fields can leak out of the AUT and increase cross-polarization levels.

5.7.2 Inside Waveguide

In order to measure the active impedance of the C-band slot, a waveguide simulator is used. The measurement setup is shown in Figure 5.22(a) and (b). The AUT is inserted into one side of the waveguide and an RF absorber is inserted into the other side.

As discussed in Appendix D, in this work, it is only practical to measure the active impedance of the H-pol slot. Figure 5.22(c) shows the measurement and simulation results. According to Figure D.5(a), in this design, the frequency of interest is 5.4 GHz where both waveguide simulator and the array have the same scan angle. At 5.4 GHz, the simulation and measurement results agree well and the input VSWR is less than 2, which demonstrates a great impedance match, even with mutual coupling.

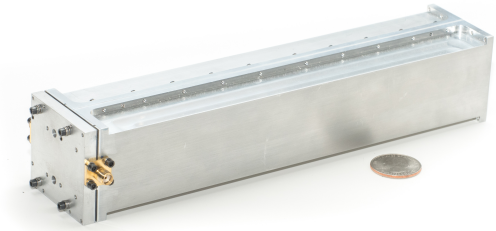

(a)

(b)

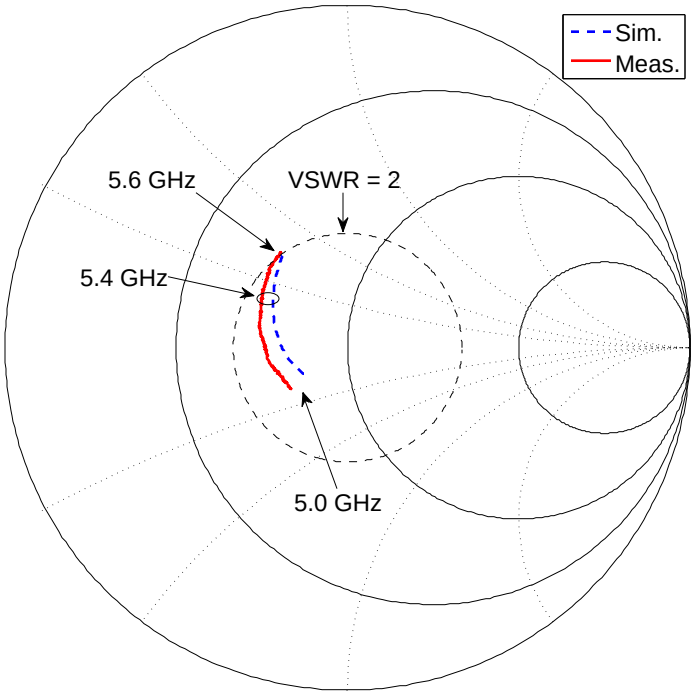

(c)

Figure 5.22: Front (a) and back (b) side of the C-band slot inside waveguide simulator. (c) Smith chart plot of simulated and measured active impedance loci for the C-band slot.

CHAPTER 6

SUMMARY, CONCLUSION AND FUTURE WORK

The architecture of a dual-band dual-polarized frequency-scanning array has been designed. The array is capable of scanning the $x - z$ plane with frequency in the range 40°—60° off broadside. It has been shown that interleaving two different types of antenna elements for the two frequency bands is a reasonable choice. It uses microstrip patch elements for Ku band and slot elements for C band. This required four separate feeding networks to drive the antenna elements in two bands for two polarizations.

In order to achieve lower transmission loss and for modularity, the aperture is divided into smaller units of subapertures and subarrays. Each unit uses the appropriate type of transmission line according to the allowed size and loss: rectangular waveguides, suspended striplines and striplines. In order to pass the signal between different media, a broadband perpendicular E-plane waveguide-to-suspended stripline transition has been designed and fabricated in Ku band. A frequency bandwidth of 12% and an insertion loss of 0.09 dB has been achieved in the measurement of the transition.

Each subarray has been designed to host nine dual-polarized Ku-band microstrip patch antennas and two perpendicular C-band slot antennas, sharing the aperture. Microstrip patches and their stripline feed networks has been integrated into an 8-layer PCB and the slots are formed on an aluminum plate under the PCB. The PCB covers the slots, but they can radiate through the openings in the ground planes of

the PCB. It was shown that this increased the radiation efficiency of the slots from 40% to around 85%. The slots are fed by suspended-striplines from below.

There are two orthogonal sets of slot arrays–one for each polarization. In order to minimize the interaction between these two sets and decrease cross-polarization levels, a symmetrical lattice has been proposed in which the surface currents created by one slot array do not get perturbed by the orthogonal slot array.

The Ku-subarray has been measured. Its input return loss was more than 9 dB in the entire frequency bandwidth and its realized gains were better than 10 dBi. Cross-polarization levels were less than -20 dB in the lower frequencies. In the higher frequencies, however, cross-polarization levels were as high as -15 dB. It has been discussed that by using mirrored feed configuration, the cross-polarization levels of the array can be improved significantly.

For the C-subarray, measured input return loss was better than 12 dB in the entire frequency bandwidth. Measured realized gain at the center frequency was -12 dBi, and cross-polarization level was better than -20 dB. It has been argued that the cross-polarization levels of the array will be even lower than this. One reason for measuring high cross-polarization levels was the parasitic radiations from the AUT and measurement setup. It has been discussed that for low-gain antennas like this one, parasitic radiations from other parts of the setup can be comparable with the desired radiations from the AUT. The full-array, on the other hand, is a high-gain antenna and measurements will be more accurate.

The future work would be building several copies of the subarryas and assembling the array. The required components are as follows:

- *Panels of Ku-subarrays:* For simplicity and repeatability, many Ku-subarray can fit on a single panel and built simultaneously. The panel size and the number of subarrays on it depends on the fabrication constraints specified by the PCB manufacturer.

- *Panels of C-band slot arrays:* Again, the number of panels depends on the comfort level of the machine shop. The metal plate hosting the slots is only 1 mm thick and hence its area must be limited to avoid bending.

- *Subaperture-level components:* WG-SSL transitions for Ku band; SSL snake feeds for Ku band; directional couplers which couple power off the SSL lines to the glass beads in the Ku band.

- *Aperture-level components:* WG corporate feed networks for both C and Ku bands; WG-SSL transitions for C band; SSL snake feeds for C band; slow-wave guides for Ku band.

As noted before, in order to improve the cross-polarization levels in the Ku band, mirrored feed configuration should be used. This technique must be applied in the SSL snake feed of the Ku-band.

APPENDIX A

STACK-UP OF THE 6-LAYER TEST BOARDS

Figure A.1 shows the stack-up of the test boards for the Ku-subarray circuits. It consist of six layers of copper cladding with Rogers RT/duroid 6202 and 2929 Bondply materials in-between as the core and the prepreg, respectively.

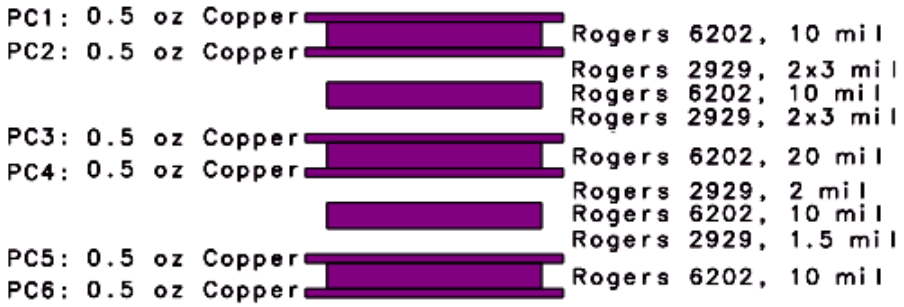

Figure A.1: Stack-up of the 6-layer test boards.

APPENDIX B

FABRICATION PROCESS OF THE 8-LAYER PCB

As discussed in Chapter 3, buried and blind vias make the fabrication process more challenging and costly. Different types of vias are shown in Figure B.1. Through vias are the oldest and simplest via configurations originally used in 2-4 layer PCB designs. The signals originate and terminate from the outer layers of the PCB. A blind via is a copper plated hole, just like a regular via, except that it interconnects only one external layer of the PCB with one or more internal layers, but does not go all the way through the board. A buried via is a copper plated hole that interconnects one or more internal layers, but does not connect to an external layer, hence the hole is completely internal or buried within the board [89, 90].

The common method for realizing these kind of vias is sequential layer build. With this method, layers are drilled, imaged, plated, etched, and laminated several times, depending on the connections to be made. After the drills are plated, the undesired part of them are drilled out in a process called back-drilling. Back-drilling removes the connection between layers which were not supposed to be connected. Finally

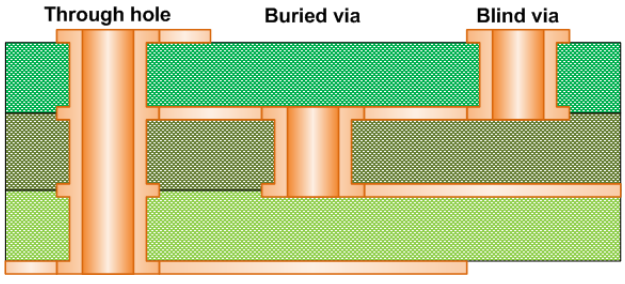

Figure B.1: Different types of vias shown in a cross-sectional view of a multi-layer board [91].

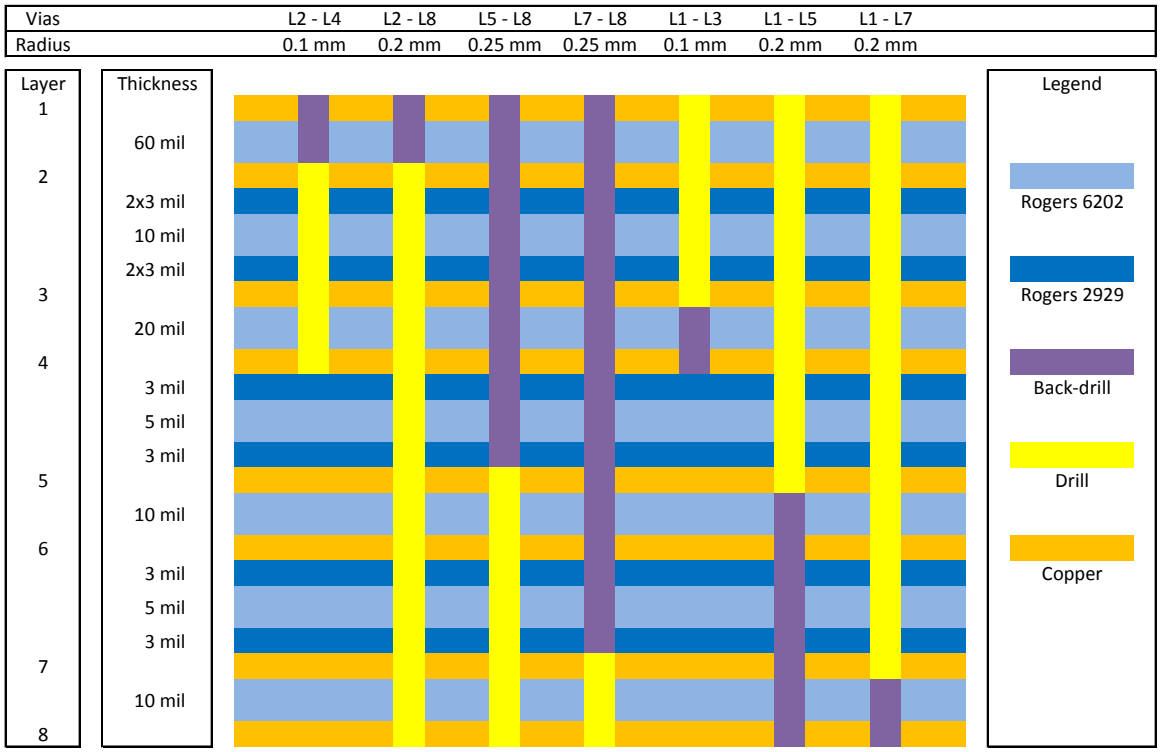

Figure B.2: Configuration of the vias in the Ku-subarray PCB.

the holes are filled with a filling material with physical properties close to the core material.

Figure B.2 shows the configuration of the vias used in this work. The core materials are RT/Duroid 6202 and they are bonded together with Rogers 2929 bondplies. The 2929 bondply is an unreinforced, hydrocarbon based thin film adhesive system intended for use in high performance, high reliability multi-layer constructions. The relative permittivity and loss of this material are given by $\epsilon_r = 2.9$ and $\tan\delta = 0.003$, respectively [67].

The fabrication process is as follows:

1. Layers 1 to 4 and 5 to 8 are laminated separately, and called *1-4 sub-assembly* and *5-8 sub-assembly*, respectively.

2. The 1-4 sub-assembly is drilled and plated to start creating L2-L4 and L1-L3 vias. At this stage they are still through vias.

3. The 1-4 sub-assembly is back-drilled from top without hitting layer 2, to make L2-L4 vias blind.

4. The 1-4 sub-assembly is back-drilled from bottom without hitting layer 3, to make L1-L3 vias blind.

5. The holes of the 1-4 sub-assembly are filled with non-conductive material and over-plated.

6. The 1-4 and 5-8 sub-assemblies are connected to build the *1-8 assembly*.

7. The 1-8 assembly is drilled and plated to start creating L2-L8, L5-L8, L7-L8, L1-L5, and L1-L7 vias. At this stage they are still through vias.

8. The 1-8 assembly is back-drilled from top to make L2-L8, L5-L8, and L7-L8 vias blind.

9. The 1-8 assembly is back-drilled from bottom to make L1-L5 and L1-L7 vias blind.

10. The holes of 1-8 assembly are filled with non-conductive material and over-plated, leaving a co-planar copper.

APPENDIX C

TRL CALIBRATION STANDARDS

TRL calibration was developed for making accurate measurements of non-coaxial devices at microwave and millimeter-wave frequencies. It is commonly used for in-fixture and on-wafer environments. The basic form uses a zero-length thru, a longer thru (usually called the line), and a high-reflect standard like open or short. There are many variations of TRL that substitute different standards (like lines for thrus, or loads for lines), but they all use the same error model and its associated assumptions. One of the biggest advantages of TRL is that the standards are generally easy to fabricate and they have simpler definitions than the standards used with SOLT. This means that for many non-coaxial applications, TRL can offer superior accuracy. For TRL, it is only required to know the impedance and approximate electrical length of the line standards, and the reflect standards can be any high reflection devices like shorts or opens. TRL does not require a load standard, which is desirable because it is difficult to make accurate high frequency, non-coaxial load standards. It is also not required to define the capacitance and inductance of the reflection standards [92–94].

C.1 For 6-Layer Test Boards

Figure C.1 shows the TRL standards used to calibrate the network analyzer in the Ku band to measure the S-parameters of the 6-layer test boards. All standards lie on the layer 5 of the stack-up shown in Appendix A. The input and output SMA connectors mount on the bottom layer (layer 6) and their center pins are connected to the vias between layers 6 and 5. Using these standards, we put the reference

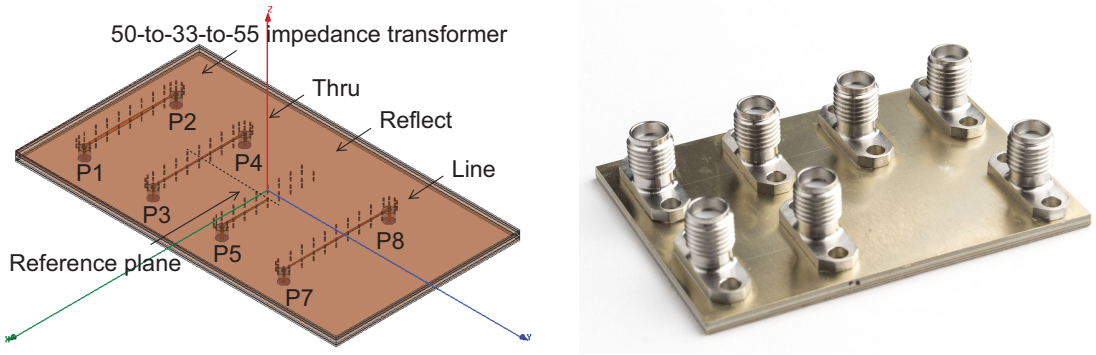

(a) (b)

Figure C.1: The calibration standards for the Ku-band 6-layer test boards. (a) HFSS model. (b) Fabricated.

plane of the measurement in the middle of the thru standard, or equivalently at the end of the reflect (open) standard. The characteristic impedance of the striplines in the calibration standards are 50 Ω. It should be noted that the 50-to-33-to-50 Ω impedance transformer between ports P1 and P2 is a back-to-back pair of 33-to-50 Ω tapered-line impedance matching transformers and is not a part of the calibration standards. It is designed for other purposes and therefore, it will not be discussed here.

For the thru step, the test ports are ususally connected together directly (zero length thru) or with a short length of transmission line (non-zero length thru). In this work, since there should be a minimum spacing between SMA connectors for fabrication and assembly purposes, we should use a non-zero length thru. The characteristic impedance of the stripline should be 50 Ω and the attenuation or phase (delay) need not be known. The transmission frequency response and port match are measured in both directions by measuring all four S-parameters. The reference plane is established in the middle of the non-zero length thru.

For the reflect step, identical high reflection coefficient standards (open circuit in this work) are connected to each test port and S_{11} and S_{22} are measured. The reflection coefficient magnitude is optimally 1.0, but need not be known.

For the line step, a short length of transmission line (longer than the thru standard) is inserted between the network analyzer ports and again the frequency response and port match are measured in both directions by measuring all four S-parameters. Insertion phase of the line must not be the same as the thru. The phase difference between the thru and line must be between 20° and 160°. Measurement uncertainty will increase significantly when the insertion phase nears 0° or an integer multiple of 180°. Optimal line length is $\lambda/4$ or 90° of insertion phase relative to the thru at the middle of the desired frequency span. Therefore, in this research, we set the phase difference to be 90° at the center frequency 13.8 GHz.

C.2 For WG-SSL Transition

Figure C.2 shows the TRL standards used to calibrate the network analyzer in the Ku band to measure the S-parameters of the back-to-back WG-SSL transition. Using these standards, we put the reference plane of the measurement in the middle of the thru standard, or equivalently at the end of the reflect (open) standard. The characteristic impedance of the SSLs in the calibration standards are 50 Ω. Same principles as discussed above apply here for designing these TRL standards.

C.3 For C-band SSL

Figure C.3 shows the TRL standards used to calibrate the network analyzer in the C band to measure the S-parameters of the C-band slot antenna. Just like discussed above, we put the reference plane of the measurement in the middle of the thru standard.

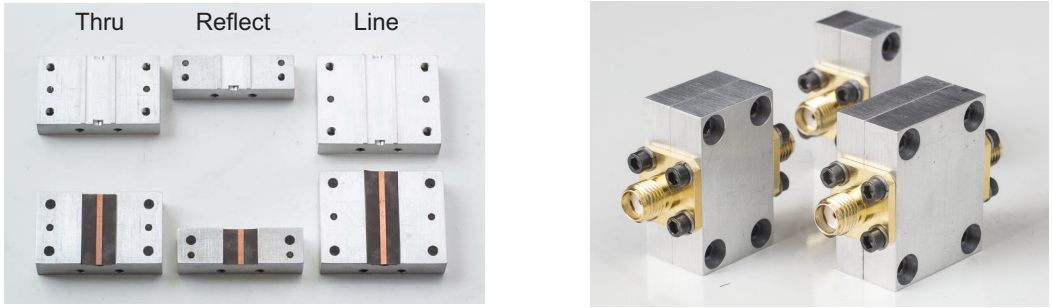

(a) (b)

Figure C.2: The calibration standards for the back-to-back WG-SSL transition. (a) Dismantled. (b) Assembled.

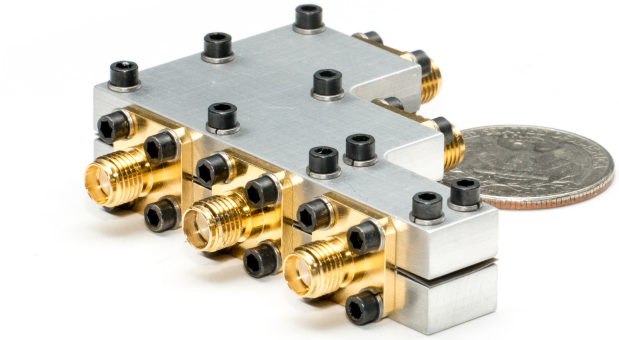

Figure C.3: The calibration standards for the C-band SSL. From left to right: line, thru, reflect.

APPENDIX D

WAVEGUIDE SIMULATOR

The active impedance is defined as that impedance seen by a generator connected to one array element when all other array elements are active [95]. Direct measurement of active impedance requires fabrication of the full array. However, it is not reasonable to build the entire array without any previous knowledge of the performance of the elements when mutually coupled with each other. Alternatively, by simple measurements of a few elements inside of waveguides, their active impedance in the antenna array may be determined [60, 96–100]. This technique allows us to economically test the antenna elements of an array without building and measuring the entire array. Metallic walls of the rectangular waveguide act like symmetrical boundary conditions around the elements. This causes the enclosed antenna elements to behave as though they are in an infinite array of like elements [101].

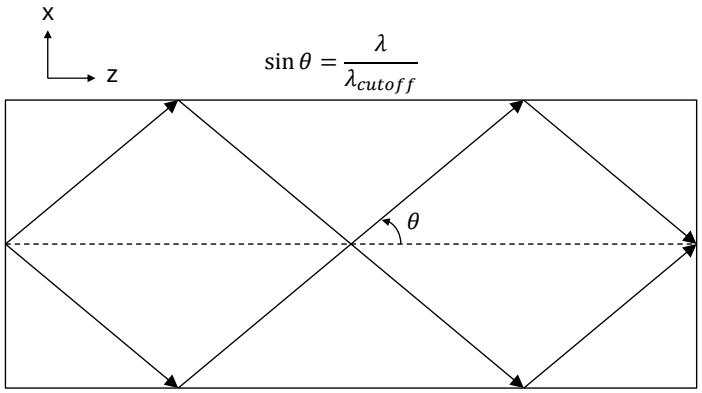

Figure D.1: Decomposition of TE_{10} mode into two plane-waves in rectangular waveguide. The angle between plane-waves' propagation direction and the axis of waveguide, θ, is a function of wavelength and waveguide dimensions.

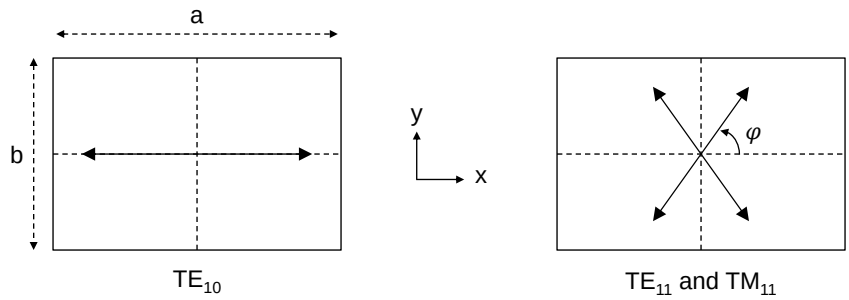

Figure D.2: Directions of propagation of plane-waves, projected onto the transverse plane of the waveguide.

The waveguide simulation method utilizes the fact that any propagating wave in a waveguide can be decomposed into plane-wave components. For instance, as shown in Figure D.1, two plane-waves are sufficient to describe the dominant TE_{10} mode in a metallic rectangular waveguide. The directions of propagation of the plane-wave components for the TE_{10} mode lie in planes parallel to the broad wall of the waveguide. For higher-order TE_{mn} and TM_{mn} modes, with $m > 0$ and $n > 0$, four plane-wave components are needed to completely describe the propagation [102]. Figure D.2 illustrates the directions of propagation of plane-waves, projected onto the transverse plane of the waveguide, for three different modes [96].

For TE_{mn} and TM_{mn} modes, propagation direction of the plane-waves can be represented by θ and ϕ angles in the standard spherical coordinate system (see Figures D.1 and D.2). They are given by [60, 95]

$$\sin\theta = \frac{\lambda}{\lambda_{cutoff}} \tag{D.1}$$

$$\tan\phi = \frac{na}{mb}, \tag{D.2}$$

where λ is the free-space wavelength and λ_{cutoff} is the cutoff wavelength for the particular mode of propagation in the waveguide. a and b are the dimensions of the waveguide in the x and y directions. Clearly, at the cutoff frequency, where

$\lambda = \lambda_{cutoff}$, the plane-waves make a right angle with the axis of waveguide and do not propagate.

In this work, we are only interested in propagation in the $x - z$ plane of the array ($\phi = 0$). According to (D.2), TE_{mn} and TM_{mn} modes with $n > 0$ yield $\phi \neq 0$, and hence, are not suitable for this application. On the other hand, the lowest order TM mode is TM_{11}. Therefore, TE_{m0} are the only modes we can use in this work.

In any simulator, each waveguide mode corresponds to one scan angle, one scan plane, and one polarization—E or H. Thus, to measure the array performance for different beam-radiation conditions, different waveguide simulators or different modes of propagation are needed.

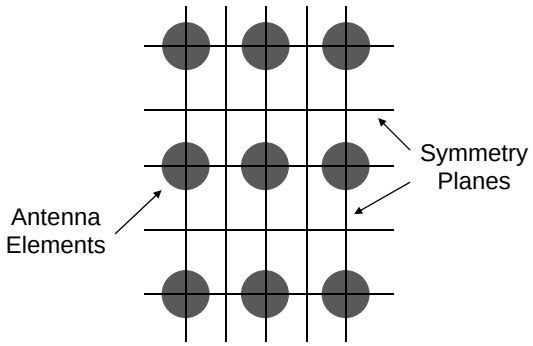

Figure D.3: Symmetry planes of a rectangular array of antenna elements.

The waveguide cross section must be quantized according to the array planes of symmetry as shown in Figure D.3. In principle, an infinite number of higher-order modes are available. Choosing any one of these modes together with an appropriate large cross section, one can yield almost any desired set of scan angles and scan planes. However, for practical reasons, it is desirable to restrict the cross section to a size requiring a reasonably small number of elements. In addition, it is best to use lower order modes to minimize spurious-mode problems [96].

It is interesting to note that some sets of symmetry planes cut antenna elements in one-half or one-quarter. Such partial elements do not need to be fed, since they are effectively shorted by the waveguide walls [98].

All TE modes in the rectangular waveguide consist of H-polarized waves, due to the H_z field component. Similarly, all TM modes in the waveguide consist of E-polarized waves, due to the E_z field component. Consequently, to simulate the E- and H-polarized radiations, we should excite the TM and TE modes in the waveguide, respectively [96]. As mentioned earlier, since the plane of propagation for TM modes do not align with the $x-z$ plane, we cannot use them in this work. Hence, using the waveguide simulation method, we are only able to measure the active impedance of H-polarized radiation.

Design procedure for waveguide simulators:

1. Determine appropriate propagation modes inside waveguide simulator based on the scan plane of the array: only TE_{m0} modes lie on the $x-z$ scan plane.

2. The waveguide walls can only lie on symmetry planes of the array. Determine the symmetry planes: see Figure D.3.

3. For each possible combination of waveguide dimensions and propagation modes, calculate the scan angle as a function of frequency: use equations (D.1) and (D.2).

4. Choose the practically smallest waveguide dimension which supports the lowest order modes in the specified range of scan angle (40°—60°): see Figure D.4.

The above steps are performed and the results are shown in Figure D.4. For the C band, a rectangular waveguide that encloses one and half slot antenna (Figure D.4(a)) is the smallest waveguide that supports TE_{10} mode in the desired range of scan angles. Figure D.4(c) shows that as the frequency increases from 5 GHz to 5.6 GHz, the scan angle of the TE_{10} mode decreases from 52°to 44°.

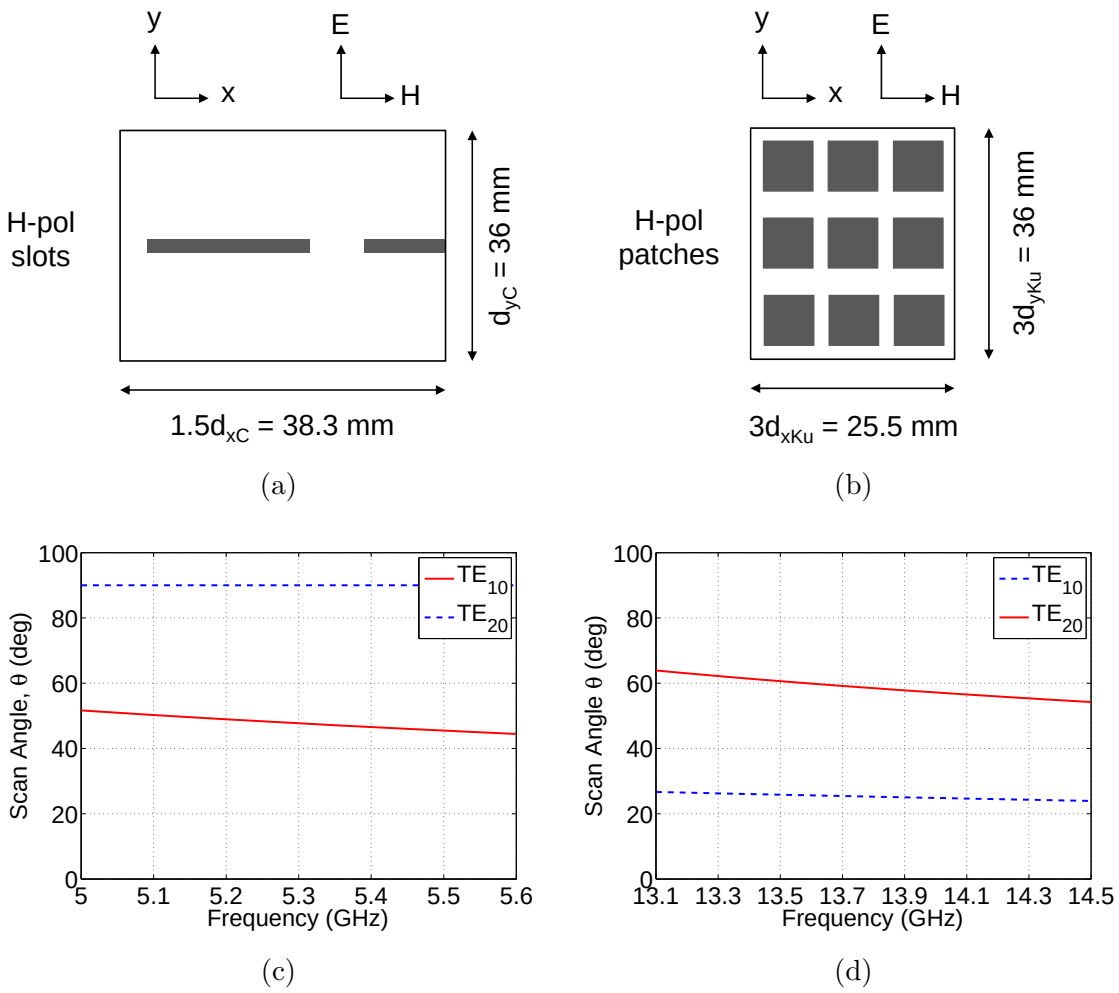

Figure D.4: Waveguide simulator cross sections and antenna elements for C-band (a) and Ku band (b). Propagation angle of the plane-wave inside waveguide simulator as a function of frequency, for different modes for C-band (c) and Ku-band (d). The scan angle of interest in this work is 40°—60°.

Due to the specific feeding scheme in this work, the smallest unit in the Ku band is a Ku-subarray which consists of an array of 3×3 patch elements. Thus, the smallest cross section for the waveguide simulator in this band will enclose 9 patch elements (see Figure D.4(b)). For this waveguide simulator, Figure D.4(d) shows that the scan angle of TE_{20} mode varies between 64°—54°, for the frequency range of 13.1—14.5°.

Figure D.5(a) overlays the propagation angle of the TE_{10} mode inside the C-band waveguide simulator (see Figure D.4(a)) with the scan angle of the C-band slot array

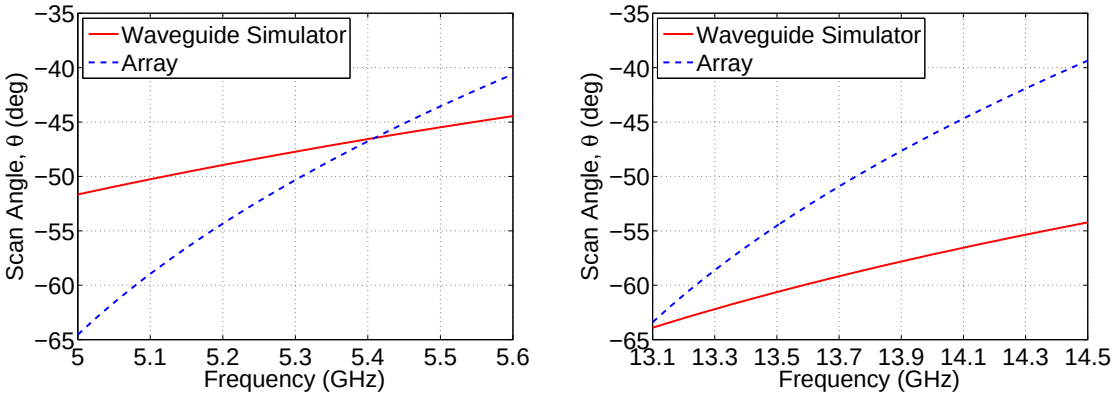

(a) (b)

Figure D.5: Scan angle inside waveguide simulator and scan angle of the array as functions of frequency. (a) In C band, the intersection point is around 5.4 GHz. (b) In Ku band, the intersection point is around 13.1 GHz.

(see Figure 2.9(a)). Measured active impedance of the slot antenna will only be valid at the intersection point of the two curves. i.e. $f = 5.4$ GHz. Similarly, according to Figure D.5(b), measured active impedance of the Ku-subarray will be meaningful around $f = 13.1$ GHz.

APPENDIX E

CAD DRAWINGS OF THE FABRICATED PARTS

The dimensions of the fabricated parts are shown in this appendix. Note that the dimensions might be slightly differet from what was shown for individual elements. For example the patch antenna dimensions were 5.5 mm×5.5 mm when individually designed in Section 3.1, but after putting everything together and simulating the entire Ku-subarray, they had to be fine tuned to 5.4 mm ×5.4 mm.

E.1 C-band

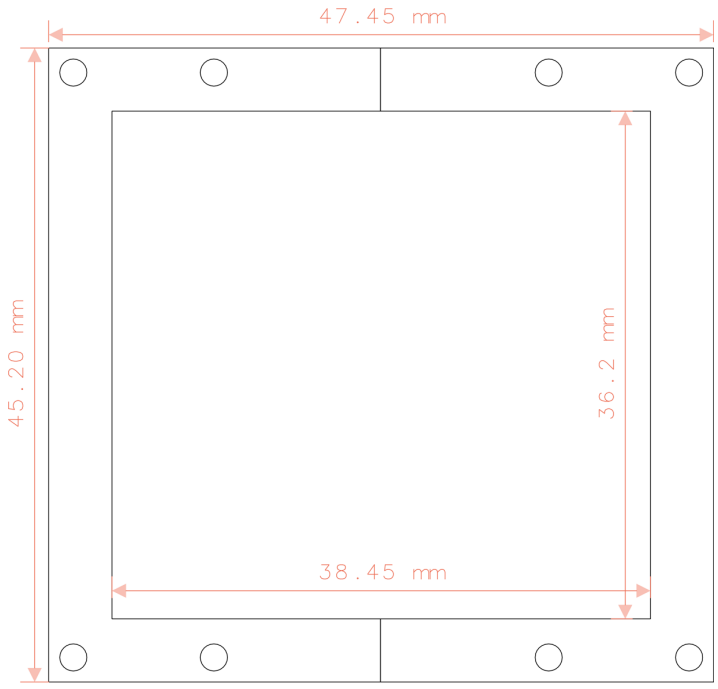

Figure E.1: Cross section of the C-band waveguide simulator. The waveguide simulator is 220 mm long.

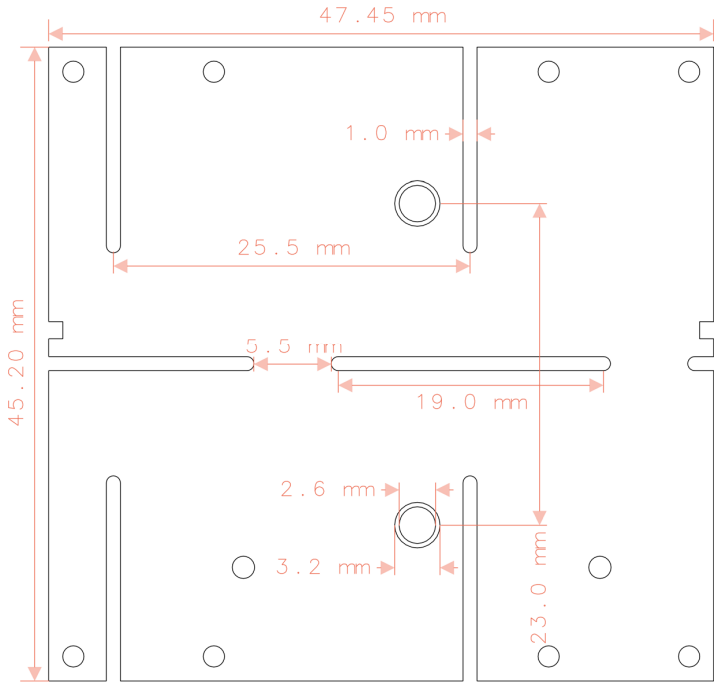

Figure E.2: Cross section of the metal plate containing the slot antennas for C-band.

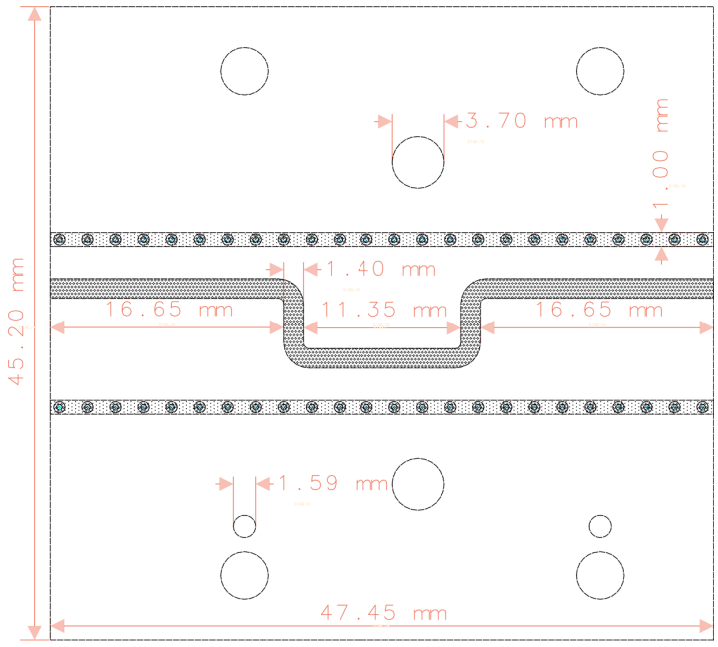

Figure E.3: Layout of the C-band SSL. The substrate is an RT/Duroid 5880 with 5 mil thickness and 1 oz copper cladding. Figure E.2 covers the top of this board and a solid metal plate covers it from below.

E.2 Ku-band

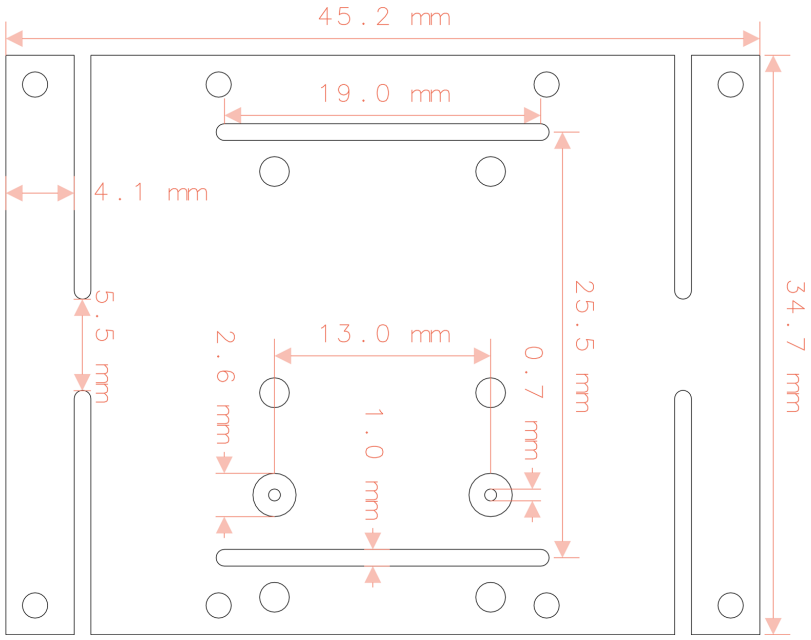

(a)

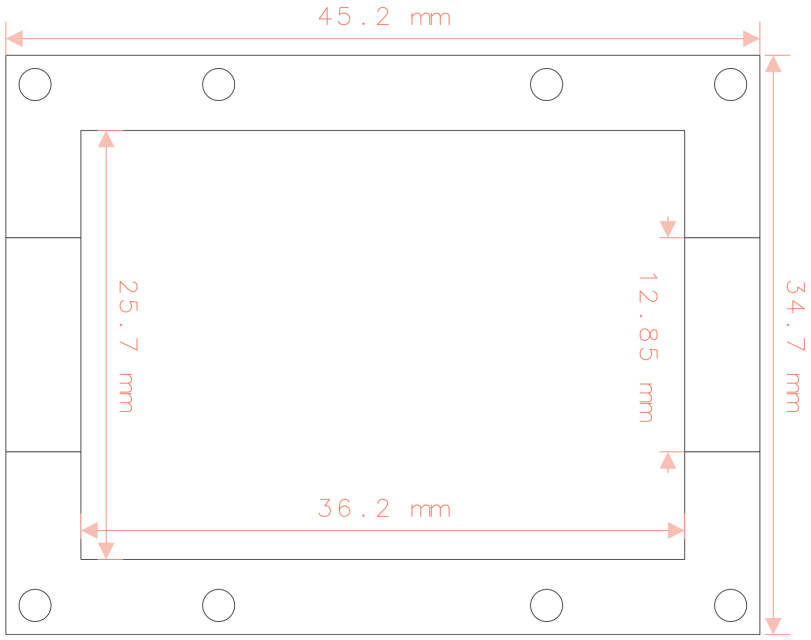

(b)

Figure E.4: Cross section of (a) the supporting metal plate and (b) the waveguide simulator for Ku-band. The waveguide simulator is 100 mm long. The metal plate supports the Ku-subarray PCB and hosts the glass beads.

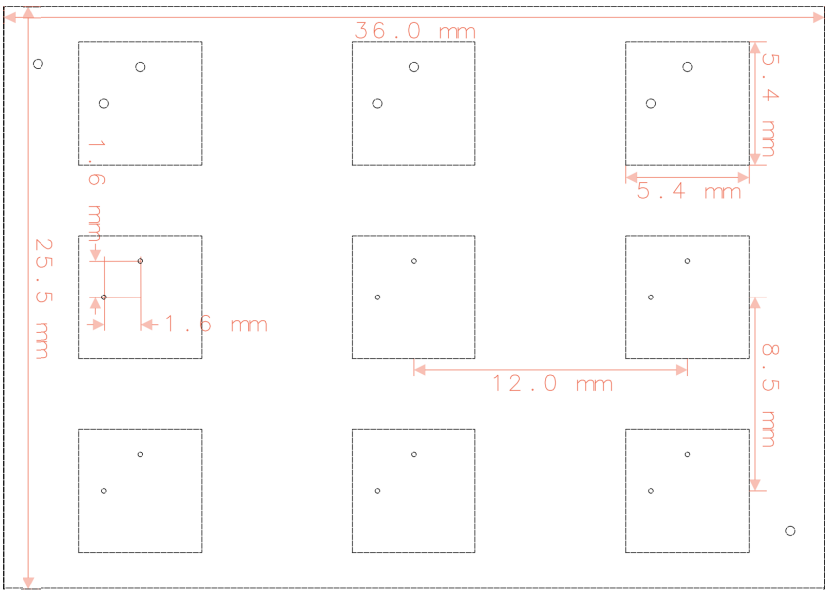

(a)

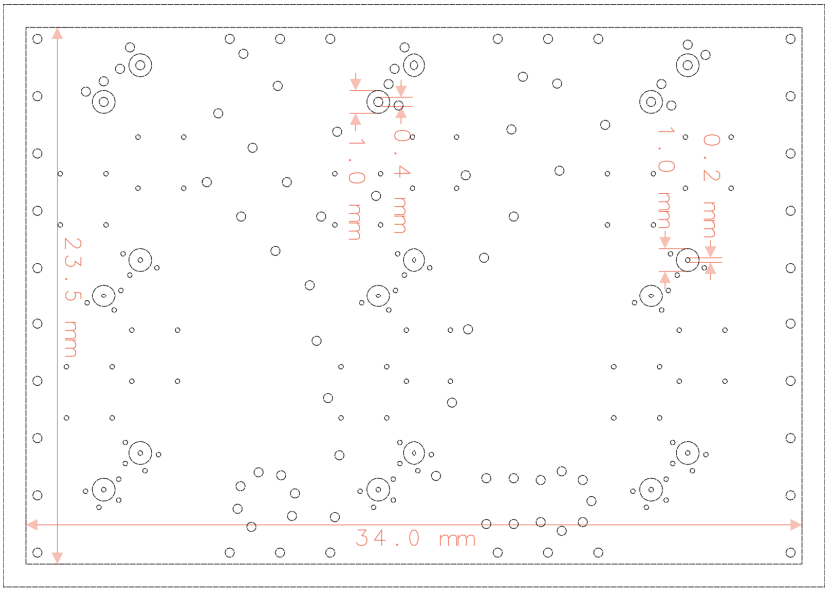

(b)

Figure E.5: Outline drawing of the metalization layers of the Ku-subarray PCB. The shaded drawings were shown in Figure 3.1. (a) Layer 1. (b) Layer 2.

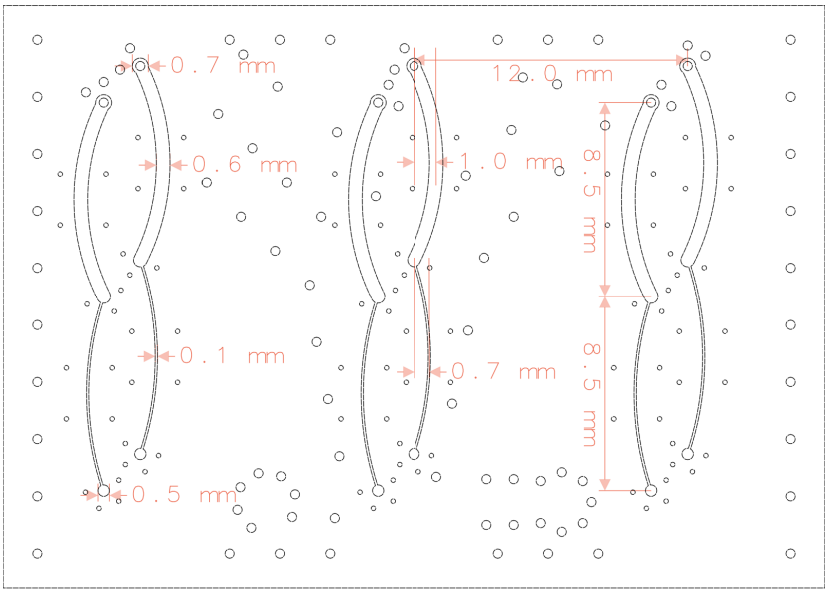

(c)

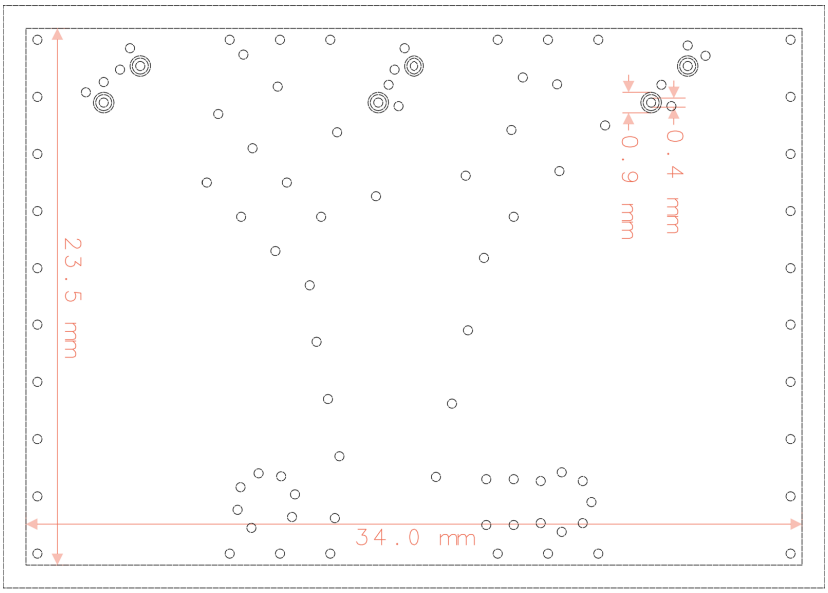

(d)

Figure E.5 (cont.): (c) Layer 3. (d) Layer 4.

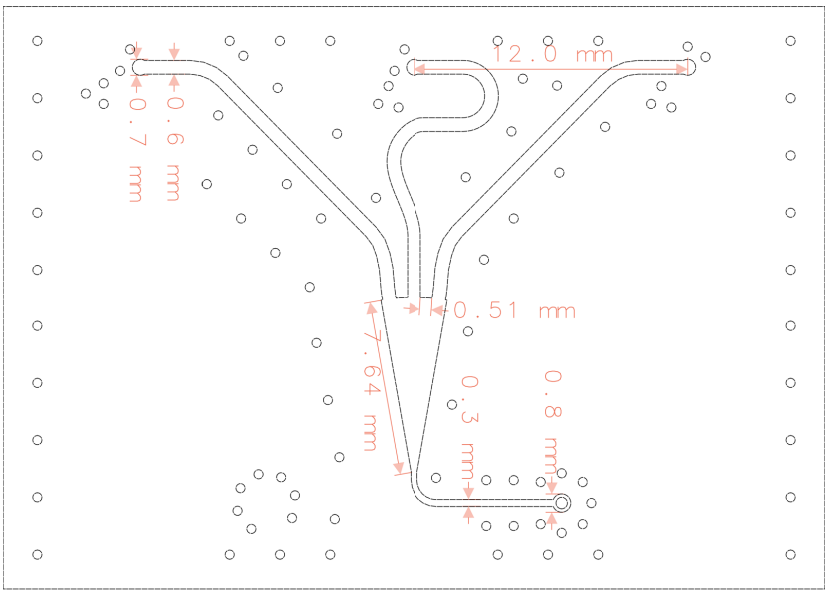

(e)

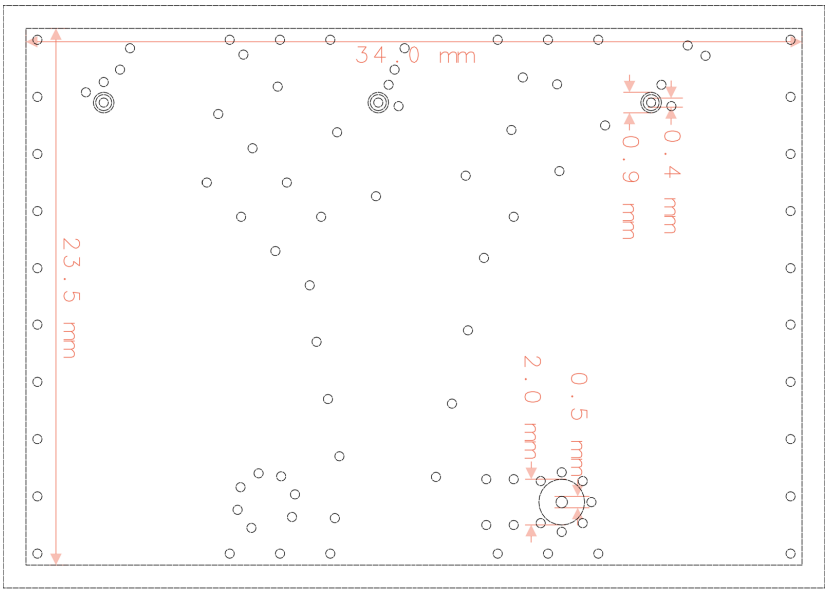

(f)

Figure E.5 (cont.): (e) Layer 5. The output traces of the 1:3 parallel power divider are designed to be equally long and present equal phases at the outputs. (f) Layer 6.

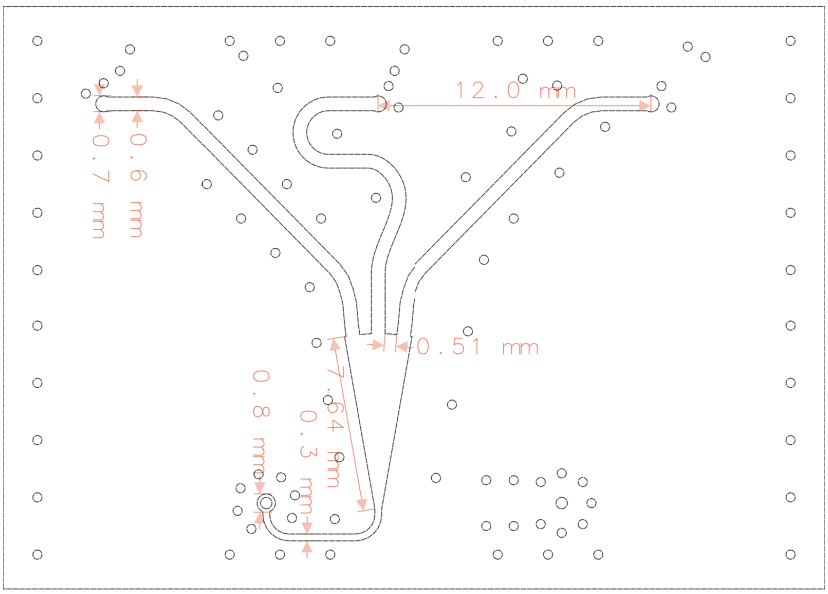

(g)

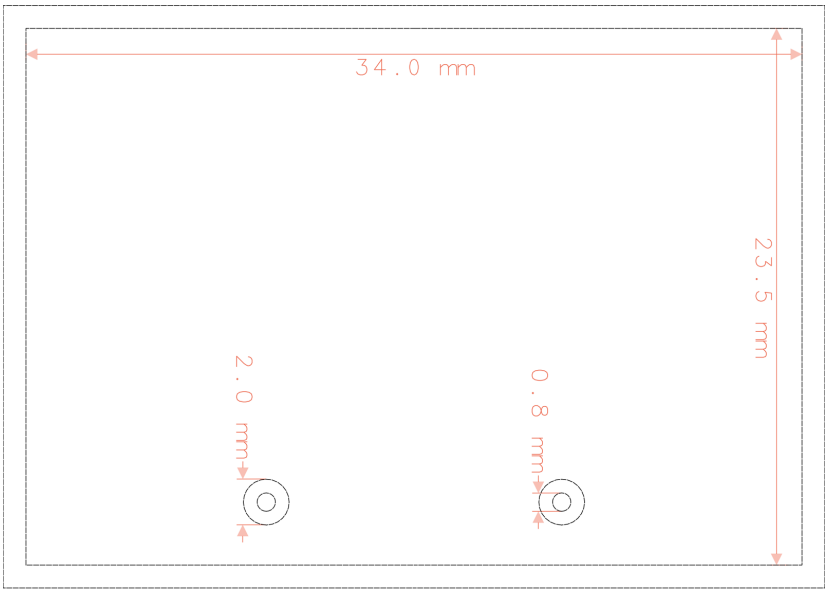

(h)

Figure E.5 (cont.): (g) Layer 7. The output traces of the 1:3 parallel power divider are designed to be equally long and present equal phases at the outputs. (h) Layer 8.

BIBLIOGRAPHY

[1] R. A. Pielke Jr, J. Gratz, C. W. Landsea, D. Collins, M. A. Saunders, and R. Musulin, "Normalized hurricane damage in the united states: 1900–2005," *Natural Hazards Rev.*, vol. 9, no. 1, pp. 29–42, 2008.

[2] S. Rose, P. Jaramillo, M. J. Small, I. Grossmann, and J. Apt, "Quantifying the hurricane risk to offshore wind turbines," *Proc. National Academy Sci.*, vol. 109, no. 9, pp. 3247–3252, 2012.

[3] Joel Cline. (2014) Hunting hurricanes and data to help build better offshore wind turbines. [Online]. Available: www.energy.gov

[4] P. L. Heinselman, D. L. Priegnitz, K. L. Manross, T. M. Smith, and R. W. Adams, "Rapid sampling of severe storms by the national weather radar testbed phased array radar," *Weather and Forecasting*, vol. 23, no. 5, pp. 808–824, 2008.

[5] D. Zrnic, J. Kimpel, D. Forsyth, A. Shapiro, G. Crain, R. Ferek, J. Heimmer, W. Benner, T. McNellis, and R. Vogt, "Agile-beam phased array radar for weather observations," *Bulletin of the American Meteorological Soc.*, vol. 88, no. 11, pp. 1753–1766, 2007.

[6] S. Karimkashi, G. Zhang, A. Kishk, W. Bocangel, R. Kelley, J. Meier, and R. Palmer, "Dual-polarization frequency scanning microstrip array antenna with low cross-polarization for weather measurements," *IEEE Trans. Antennas Propag.*, vol. 61, no. 11, pp. 5444–5452, Nov 2013.

[7] J. Dvorsky, "Implementation of dual-polarization on an airborne scatterometer and preliminary data quality," Master's thesis, UMass Amherst, 2012.

[8] M. Smith, R. Crowley, and R. Roeder, "SeaWinds - a new spaceborne radar for measuring ocean wind vectors," in *IEEE Southeastcon '96. Bringing Together Educ., Sci. Technol.*, Apr 1996, pp. 265–268.

[9] W.-Y. Tsai, M. Spencer, C. Wu, C. Winn, and K. Kellogg, "SeaWinds on QuikSCAT: sensor description and mission overview," in *IEEE Int. Geosci. Remote Sens. Symp.*, vol. 3, 2000, pp. 1021–1023 vol.3.

[10] D. E. Fernandez, J. Carswell, S. Frasier, P. Chang, P. Black, and F. Marks, "Dual-polarized C- and Ku-band ocean backscatter response to hurricane-force winds," *J. Geophysical Research: Oceans (1978–2012)*, vol. 111, no. C8, 2006.

[11] M. W. Spencer, C. Wu, and D. G. Long, "Improved resolution backscatter measurements with the seawinds pencil-beam scatterometer," *IEEE Trans. Geosci. Remote Sens.*, vol. 38, no. 1, pp. 89–104, Jan 2000.

[12] Z. Jelenak and P. Chang, "Impact of the dual-frequency scatterometer on NOAA operations," in *IEEE Int. Geosci. Remote Sens. Symp.*, July 2010, pp. 1808–1811.

[13] J. Carswell, D. Perkovic, T. Chu, S. Frasier, P. Chang, and Z. Jelenak, "Preliminary investigation of splash effect on high wind C-band HH-pol model function," in *IEEE Int. Geosci. Remote Sens. Symp.*, July 2010, pp. 2539–2542.

[14] D. Fernandez, E. Kerr, A. Castells, J. Carswell, S. Frasier, P. Chang, P. Black, and F. Marks, "IWRAP: the imaging wind and rain airborne profiler for remote sensing of the ocean and the atmospheric boundary layer within tropical cyclones," *IEEE Trans. Geosci. Remote Sens.*, vol. 43, no. 8, pp. 1775–1787, Aug 2005.

[15] J. Sapp, S. Frasier, J. Dvorsky, P. Chang, and Z. Jelenak, "Airborne dual-polarization observations of the sea surface NRCS at C-band in high winds," *IEEE Geosci. Remote Sens. Lett.*, vol. 10, no. 4, pp. 726–730, July 2013.

[16] NOAA. (2013) Business operations manual. [Online]. Available: www.ppi.noaa.gov

[17] M. Danielsen and R. Jorgensen, "Frequency scanning microstrip antennas," *IEEE Trans. Antennas Propag.*, vol. 27, no. 2, pp. 146–150, Mar 1979.

[18] I. Bahl and K. Gupta, "Frequency scanning by leaky-wave antennas using artificial dielectrics," *IEEE Trans. Antennas Propag.*, vol. 23, no. 4, pp. 584–589, Jul 1975.

[19] A. Fackelmeier and E. Biebl, "Narrowband frequency scanning array antenna at 5.8 GHz for short range imaging," in *IEEE MTT-S Int. Microw. Symp. Dig.*, May 2010, pp. 1266–1269.

[20] A. Al-Zoubi, A. Kishk, and A. Glisson, "A linear rectangular dielectric resonator antenna array fed by dielectric image guide with low cross polarization," *IEEE Trans. Antennas Propag.*, vol. 58, no. 3, pp. 697–705, March 2010.

[21] ——, "Slot-aperture-coupled linear dielectric resonator array fed by dielectric image line backed by a reflector," in *IEEE Antennas Propag. Soc. Int. Symp.*, July 2008, pp. 1–4.

[22] H. Wang, P. Ge, D.-G. Fang, X. Ma, and W. Sheng, "A low loss frequency scanning planar array using hybrid coupling," in *Int. Conf. Microw. Millimeter Wave Technol.*, May 2010, pp. 1908–1911.

[23] C. Vazquez, C. Garcia, Y. Alvarez, S. Ver-Hoeye, and F. Las-Heras, "Near field characterization of an imaging system based on a frequency scanning antenna array," *IEEE Trans. Antennas Propag.*, vol. 61, no. 5, pp. 2874–2879, May 2013.

[24] P. Hallbjorner, I. Skarin, K. From, and A. Rydberg, "Circularly polarized traveling-wave array antenna with novel microstrip patch element," *IEEE Antennas Wireless Propag. Lett.*, vol. 6, pp. 572–574, 2007.

[25] J. Choi, J. Sun, and T. Itoh, "Frequency-scanning phased-array feed network based on composite right/left-handed transmission lines," *IEEE Trans. Microw. Theory Techn.*, vol. 61, no. 8, pp. 3148–3157, Aug 2013.

[26] J. H. Choi and T. Itoh, "Dual-band composite right/left-handed (CRLH) phased-array antenna," *IEEE Antennas Wireless Propag. Lett.*, vol. 11, pp. 732–735, 2012.

[27] R. Doviak, V. Bringi, A. Ryzhkov, A. Zahrai, and D. Zrnic, "Considerations for polarimetric upgrades to operational WSR-88D radars," *J. Atmospheric Ocean. Technol.*, vol. 17, no. 3, pp. 257–278, 2000.

[28] G. Zhang, R. Doviak, D. Zrnic, J. Crain, D. Staiman, and Y. Al-Rashid, "Phased array radar polarimetry for weather sensing: A theoretical formulation for bias corrections," *IEEE Trans. Geosci. Remote Sens.*, vol. 47, no. 11, pp. 3679–3689, Nov 2009.

[29] Q. Cao, M. B. Yeary, and G. Zhang, "Efficient ways to learn weather radar polarimetry," *IEEE Tran. Educ.*, vol. 55, no. 1, pp. 58–68, 2012.

[30] S. Karimkashi and G. Zhang, "An optimal design of a cylindrical polarimetric phased array radar for weather sensing," *Radio Sci.*, vol. 47, no. 2, 2012.

[31] G. Zhang, R. J. Doviak, D. S. Zrnic, R. Palmer, L. Lei, and Y. Al-Rashid, "Polarimetric phased-array radar for weather measurement: A planar or cylindrical configuration?" *J. Atmospheric Ocean. Technol.*, vol. 28, no. 1, pp. 63–73, 2011.

[32] S. Karimkashi, G. Zhang, R. Kelley, J. Meier, R. Palmer, A. Zahrai, R. Doviak, and D. Zrnic, "Cylindrical polarimetric phased array radar demonstrator: Design and analysis of a frequency scanning antenna array," in *IEEE. Int. Symp. Phased Array Systems Technol.*, Oct 2013, pp. 477–480.

[33] S. Karimkashi and G. Zhang, "A dual-polarized series-fed microstrip antenna array with very high polarization purity for weather measurements," *IEEE Trans. Antennas Propag.*, vol. 61, no. 10, pp. 5315–5319, Oct 2013.

[34] S. Karimkashi, G. Zhang, and A. Kishk, "A dually polarized frequency scanning microstrip array antenna for weather radar applications," in *7th Eur. Conf. Antennas Propag.*, April 2013, pp. 1795–1798.

[35] T. Chiba, Y. Suzuki, and N. Miyano, "Suppression of higher modes and cross polarized component for microstrip antennas," in *IEEE Antennas Propag. Soc. Int. Symp.*, vol. 20, May 1982, pp. 285–288.

[36] W.-H. Hsu and K.-L. Wong, "A dual capacitively fed broadband patch antenna with reduced cross-polarization radiation," *Microw. Opt. Technol. Lett.*, vol. 26, no. 3, pp. 169–171, 2000.

[37] C. Fulton and W. Chappell, "A dual-polarized patch antenna for weather radar applications," in *IEEE Int. Conf. Microw. Commun. Antennas Electron. Syst.*, Nov 2011, pp. 1–5.

[38] P. Patel, "A dual polarised microstrip antenna with low cross-polarisation, for SAR applications," in *IEEE Antennas Propag. Soc. Int. Symp.*, vol. 3, July 1996, pp. 1536–1539 vol.3.

[39] J. Granholm and K. Woelders, "Dual polarization stacked microstrip patch antenna array with very low cross-polarization," *IEEE Trans. Antennas Propag.*, vol. 49, no. 10, pp. 1393–1402, Oct 2001.

[40] K. Woelder and J. Granholm, "Cross-polarization and sidelobe suppression in dual linear polarization antenna arrays," *IEEE Trans. Antennas Propag.*, vol. 45, no. 12, pp. 1727–1740, Dec 1997.

[41] J. Hirokawa, "High-gain, high-efficiency and wide-band planar hollow-waveguide antennas by diffusion-bonding of laminated metal plates for sub-millimeter wave and THz bands," in *Int. Topical Meeting Microw. Photon.*, Sept 2012, pp. 64–67.

[42] J. Hirokawa, M. Zhang, Y. Miura, and M. Ando, "High-efficiency wide-band double-layer slotted hollow waveguide array antennas by diffusion bonding of laminated thin metal plates," in *Conf. Proc. ICECom*, Sept 2010, pp. 1–4.

[43] M. Zhang, J. Hirokawa, and M. Ando, "Fabrication of a slotted waveguide array at 94GHz by diffusion bonding of laminated thin plates," in *IEEE Antennas Propag. Soc. Int. Symp.*, June 2009, pp. 1–4.

[44] J. Hirokawa, M. Zhang, and M. Ando, "94GHz fabrication of a slotted waveguide array antenna by diffusion bonding of laminated thin plates," in *IEEE Sensors*, Oct 2009, pp. 907–911.

[45] D. Kim, M. Zhang, J. Hirokawa, and M. Ando, "Design of dual-polarization waveguide slot array antenna using diffusion bonding of laminated thin plates for the 60 GHz-band," in *IEEE Antennas Propag. Soc. Int. Symp.*, July 2012, pp. 1–2.

[46] ——, "Design and fabrication of a dual-polarization waveguide slot array antenna with high isolation and high antenna efficiency for the 60 GHz band," *IEEE Trans. Antennas Propag.*, vol. 62, no. 6, pp. 3019–3027, June 2014.

[47] Y. Li, Z. Zhang, C. Deng, Z. Feng, and M. Iskander, "2-D planar scalable dual-polarized series-fed slot antenna array using single substrate," *IEEE Trans. Antennas Propag.*, vol. 62, no. 4, pp. 2280–2283, April 2014.

[48] R. Pokuls, J. Uher, and D. Pozar, "Microstrip antennas for SAR applications," *IEEE Trans. Antennas Propag.*, vol. 46, no. 9, pp. 1289–1296, Sep 1998.

[49] J. Eade and J. Whitehurst, "Dual band phased array antenna design for radar applications," in *11th Int. Conf. Antennas Propag.*, vol. 1, 2001, pp. 77–81 vol.1.

[50] A. Sondas, M. Ucar, and Y. Erdemli, "Loop-loaded printed dipole array design for a dual-band radar application," in *Loughborough Antennas Propag. Conf.*, Nov 2009, pp. 529–532.

[51] K. Naishadham, R. Li, L. Yang, T. Wu, W. Hunsicker, and M. Tentzeris, "A shared-aperture dual-band planar array with self-similar printed folded dipoles," *IEEE Trans. Antennas Propag.*, vol. 61, no. 2, pp. 606–613, Feb 2013.

[52] R. Jordan, B. Huneycutt, and M. Werner, "The SIR-C/X-SAR synthetic aperture radar system," *IEEE Trans. Geosci. Remote Sens.*, vol. 33, no. 4, pp. 829–839, Jul 1995.

[53] D. M. Pozar and S. D. Targonski, "A shared-aperture dual-band dual-polarized microstrip array," *IEEE Trans. Antennas Propag.*, vol. 49, no. 2, pp. 150–157, Feb 2001.

[54] L. Shafai, W. Chamma, M. Barakat, P. Strickland, and G. Seguin, "Dual-band dual-polarized perforated microstrip antennas for SAR applications," *IEEE Trans. Antennas Propag.*, vol. 48, no. 1, pp. 58–66, Jan 2000.

[55] X. Qu, S. Zhong, and Y.-M. Zhang, "Dual-band dual-polarised microstrip antenna array for SAR applications," *Electronics Lett.*, vol. 42, no. 24, pp. 1376–1377, November 2006.

[56] X. Qu, S.-S. Zhong, Y. M. Zhang, and W. Wang, "Design of an S/X dual-band dual-polarised microstrip antenna array for SAR applications," *IET Microw. Antennas Propag.*, vol. 1, no. 2, pp. 513–517, April 2007.

[57] Z. Shi-Gang and C. Tan-Huat, "Dual-wideband, dual-polarized shared aperture antenna with high isolation and low cross-polarization," in *10th Int. Symp. Antennas Propag. EM Theory*, Oct 2012, pp. 30–33.

[58] D. Fernandez, P. Chang, J. Carswell, R. Contreras, and S. Frasier, "IWRAP: the imaging wind and rain airborne profiler for remote sensing of the ocean and the atmospheric boundary layer within tropical cyclones," in *IEEE Aerosp. Conf.*, Big Sky, MT, Mar 2006, pp. 1–7.

[59] M. I. Skolnik, *Introduction to radar systems*. McGraw-Hill, 2001.

[60] R. C. Hansen, *Phased array antennas.* John Wiley & Sons, 2009.

[61] C. A. Balanis, *Antenna theory: analysis and design.* John Wiley & Sons, 2005.

[62] J. D. Kraus and R. J. Marhefka, *Antennas for all applications.* McGraw-Hill, 2002.

[63] M. I. Skolnik, *Radar handbook.* McGraw-Hill, 2008.

[64] J. L. Volakis, *Antenna engineering handbook.* McGraw-Hill, 2007.

[65] Rogers Corporation. (2011) RT/duroid® 5870 /5880 high frequency laminates. [Online]. Available: www.rogerscorp.com

[66] ——. (2013) RT/duroid® 6202 high frequency laminates. [Online]. Available: www.rogerscorp.com

[67] ——. (2013) 2929 bondply data sheet. [Online]. Available: www.rogerscorp.com

[68] D. M. Pozar, "Microstrip antennas," *Proc. of IEEE*, vol. 80, no. 1, pp. 79–91, 1992.

[69] R. E. Collin, *Foundations for Microwave Engineering.* McGraw-Hill, 1992.

[70] D. M. Pozar, *Microwave Engineering.* John Wiley & Sons, 2009.

[71] A. Fathy and D. Kalokitis, "A simplified approach for the design of radial power combining structures," in *IEEE MTT-S Int. Microw. Symp. Dig.*, vol. 1, June 2004, pp. 73–76 Vol.1.

[72] J. Denoual, A. Peden, B. Della, and J.-P. Fraysse, "16-way radial divider/combiner for solid state power amplifiers in the K band," in *38th Eur. Microw. Conf.*, Oct 2008, pp. 345–348.

[73] K. Chang, M. Li, K. Hummer, and R. Speciale, "High power four-way power divider/combiner," in *IEEE MTT-S Int. Microw. Symp. Dig.*, May 1990, pp. 1329–1332 vol.3.

[74] E. J. Wilkinson, "An n-way hybrid power divider," *IRE Trans. Microw. Theory Techn.*, vol. 8, no. 1, pp. 116–118, January 1960.

[75] A. Saleh, "Planar electrically symmetric n-way hybrid power dividers/combiners," *IEEE Trans. Microw. Theory Techn.*, vol. 28, no. 6, pp. 555–563, Jun 1980.

[76] M. Abouzahra and K. Gupta, "Multiple-port power divider/combiner circuits using circular microstrip disk configurations," *IEEE Trans. Microw. Theory Techn.*, vol. 35, no. 12, pp. 1296–1302, Dec 1987.

[77] G. Bartolucci, F. Giannini, and C. Paoloni, "On the design of optimized microstrip radial line power dividers," in *20th Eur. Microw. Conf.*, vol. 2, Sept 1990, pp. 1047–1052.

[78] ANSYS, Inc. (2010) Antenna/RF training guide. [Online]. Available: www.ansys.com

[79] Y. Deguchi, K. Sakakibara, N. Kikuma, and H. Hirayama, "Millimeter-wave microstrip-to-waveguide transition operating over broad frequency bandwidth," in *IEEE MTT-S Int. Microw. Symp. Dig.*, Long Beach, CA, Jun. 2005, pp. 2107–2110.

[80] F. Schmuckle, W. Gross, K. Hirche, M. Rostewitz, and W. Heinrich, "A 30-GHz waveguide-to-microstrip-transition," in *Proc. IEEE MTT-S Int. Microw. Symp.*, Honolulu, Hawaii, Jun. 2007, pp. 1169–1172.

[81] J. Machac and W. Menzel, "On the design of waveguide-to-microstrip and waveguide-to-coplanar line transitions," in *Proc. 23rd Eur. Microw. Conf.*, Madrid, Spain, Sept 1993, pp. 615–616.

[82] W. Grabherr, B. Huder, and W. Menzel, "Microstrip to waveguide transition compatible with mm-wave integrated circuits," *IEEE Trans. Microw. Theory Techn.*, vol. 42, no. 9, pp. 1842–1843, 1994.

[83] R. Glogowski, J.-F. Zurcher, C. Peixeiro, and J. Mosig, "Ka-band rectangular waveguide to suspended stripline transition," *IEEE Microw. Compon. Lett.*, vol. 23, no. 11, pp. 575–577, 2013.

[84] M. A. Nikravan and D.-H. Kwon, "A vertical waveguide-to-suspended stripline transition," in *Proc. IEEE Antennas Propag. Society Int. Symp.*, July 2014, pp. 1696–1697.

[85] ——, "A broadband perpendicular E-plane waveguide-to-suspended stripline transition," *Microw. Opt. Techn. Lett.*, vol. 58, no. 8, pp. 1831–1834, August 2016.

[86] S. Amari, U. Rosenberg, and J. Bornemann, "Adaptive synthesis and design of resonator filters with source/load-multiresonator coupling," *IEEE Trans. Microw. Theory Techn.*, vol. 50, no. 8, pp. 1969–1978, 2002.

[87] I. Awai, A. Kundu, and T. Yamashita, "Equivalent-circuit representation and explanation of attenuation poles of a dual-mode dielectric-resonator bandpass filter," *IEEE Trans. Microw. Theory Techn.*, vol. 46, no. 12, pp. 2159–2163, 1998.

[88] S. Park, Y. Okajima, J. Hirokawa, and M. Ando, "A slotted post-wall waveguide array with interdigital structure for 45 deg; linear and dual polarization," *IEEE Trans. Antennas Propag.*, vol. 53, no. 9, pp. 2865–2871, Sept 2005.

[89] Omni Circuit Boards. (2015) Blind and buried vias. [Online]. Available: www.omnicircuitboards.com

[90] Royal Circuit Solutions. (2015) Designing with vias. [Online]. Available: www.royalcircuits.com

[91] EEVBlog. (2015) Buried vias and their effect on PCB cost. [Online]. Available: www.eevblog.com

[92] Agilent Technologies. (2006) In-fixture measurements using vector network analyzers. [Online]. Available: www.agilent.com

[93] ——. (2006) Advanced calibration techniques for vector network analyzers. [Online]. Available: www.agilent.com

[94] ——. (2000) Agilent network analysis applying the 8510 TRL calibration for non-coaxial measurements. [Online]. Available: www.agilent.com

[95] M. Balfour, "Active impedance of a phased-array antenna element simulated by a single element in waveguide," *IEEE Trans. Antennas Propag.*, vol. 15, no. 2, pp. 313–314, March 1967.

[96] P. Hannan and M. Balfour, "Simulation of a phased-array antenna in waveguide," *IEEE Trans. Antennas Propag.*, vol. 13, no. 3, pp. 342–353, May 1965.

[97] H. Wheeler, "A systematic approach to the design of a radiator element for a phased-array antenna," *Proc. IEEE*, vol. 56, no. 11, pp. 1940–1951, Nov 1968.

[98] D. M. Pozar, "Analysis of an infinite phased array of aperture coupled microstrip patches," *IEEE Trans. Antennas Propag.*, vol. 37, no. 4, pp. 418–425, Apr 1989.

[99] J. Lee and R.-S. Chu, "Aperture matching of a dielectric loaded circular waveguide element array," *IEEE Trans. Antennas Propag.*, vol. 37, no. 3, pp. 395–399, March 1989.

[100] R. J. Mailloux, *Phased array antenna handbook*. Artech House, 2005.

[101] J. Stockmann and R. Hodges, "The use of waveguide simulators to measure the resonant frequency of Ku-band microstrip arrays," in *IEEE Antennas Propag. Soc. Int. Symp.*, vol. 1A, July 2005, pp. 417–420 Vol. 1A.

[102] L. Page and N. Adams Jr, "Electromagnetic waves in conducting tubes," *Physical Rev.*, vol. 52, no. 6, p. 647, 1937.